ABSTRACT

Generally, this study comprises of 3 stages. Firstly, pure maghemite nanoparticles were synthesized within 10nm size range. Secondly, the nanoparticles were encapsulated into the silica xerogel matrix to minimize agglomeration and aggregation by producing nanocomposites. Finally, the surface area of the nanocomposites was increased by modifying the matrix into silica particulate form. The nanoparticles and nanocomposites were characterized using XRD, TGA, TEM, BET, DLS and AGM.

In stage I, the effects of varying the $FeCl_2$ concentration on the properties of magnetic nanoparticles produced by Massart's procedure were investigated. The lattice parameters of the samples obtained from XRD analysis revealed that the nanoparticles formed were maghemites (γ-Fe_2O_3). The magnetization curves showed no hysteresis, indicating that the particles were superparamagnetic. The crystallite, magnetic and physical sizes were similar, indicating that the particles were monocrystals. When the $FeCl_2$ concentration increased from 0.1 to 1.0M, the size of as-synthesized maghemite nanoparticles decreased. However, when the $FeCl_2$ concentration was increased further, the size of as-synthesized maghemite nanoparticles increased. This indicates that a very low or a very high $FeCl_2$ concentration leads to the formation of larger particles. In addition, agglomeration and aggregation occurred for most samples. Superparamagnetic maghemite nanoparticles with the smallest size were chosen to proceed to stage II and stage III.

Maghemite-silica xerogel nanocomposites were produced by dispersing the as-synthesized maghemite nanoparticles into silica xerogel by sol-gel technique. The phase

analysis performed using XRD confirmed that the encapsulated nanoparticles were maghemites. TEM micrographs showed that the maghemite nanoparticles were spherical and homogeneously incorporated into the silica xerogel matrix. The surface area of the nanocomposites was less than $40m^2/g$. This was probably due to the fact that majority of the pores in the silica gel were filled by as-synthesized maghemite nanoparticles. Reduction in average crystallite size of dispersed maghemite particles was observed after the encapsulation process compared to as-synthesized maghemite nanoparticles. However, increasing the weight ratio of Fe_2O_3/SiO_2 in nanocomposites caused an increase in average crystallite size of embedded maghemite nanoparticles.

Maghemite-silica particulate nanocomposites were prepared by a modified sol-gel process. The purpose of changing the matrix from xerogel to particulate form was to increase the surface area and retain its properties. It is a promising alternative technique for fabricating nanocomposites because it is simple, manufacturable, inexpensive, fast, can be prepared at room temperature and its ability to control the composition, crystalline distribution and properties of maghemite nanoparticles and nanocomposites. Moreover, no surfactant or other unnecessary precursor was involved. The HRTEM micrograph revealed that the embedded particle (core) was with the presence of atomic interspaces indicating that the particles were crystalline and covered with a non-crystalline material. The EELS result showed the presence of Fe-L_3 signals, which proves that the embedded particles were iron-based compounds. In stage III, a very high surface area was attained for the produced nanocomposites (360 – 390 m^2/g), compared with those of stage II. This enhances the sensitivity and the reactivity of the nanocomposites.

ABSTRAK

Secara keseluruhan, kajian ini meliputi tiga tahap. Yang pertama sekali, adalah sintesis nano-zarah maghemit dalam lingkungan saiz 10nm. Selanjutnya, adalah proses pengkapsulan nano-zarah ke dalam matriks xerogel silika untuk meminimumkan pengelompokan dan agregasi semasa menghasilkan nano-komposit. Akhirnya, adalah untuk menambahkan luas permukaan nano-komposit yang dihasilkan dengan mengubahsuai matriks ke bentuk zarahan silika.

Pada tahap I, kesan-kesan dipengaruhi oleh kepekatan $FeCl_2$ yang berlainan pada sifat-sifat nano-zarah magnetik yang dihasilkan oleh prosedur Massart diselidik. Kisi parameter yang diperolehi daripada analisis XRD menunjukkan bahawa nano-zarah yang dihasilkan adalah maghemit (γ-Fe_2O_3). Lengkungan pemagnetan tidak menunjukkan hysteresis, menandakan bahawa zarah adalah superparamagnetik. Nilai saiz kristalit, magnetik dan fizikal yang berdekatan menunjukkan bahawa zarah adalah monokristal. Boleh disimpulkan bahawa apabila kepekatan $FeCl_2$ bertambah dari 0.1M ke 1.0M, saiz nano-zarah maghemit yang disintesis berkurang. Namun, apabila kepekatan $FeCl_2$ bertambah dengan selanjutnya, saiz nano-zarah maghemit yang disintesis akan menambah. Ini menunjukkan bahawa kepekatan $FeCl_2$ yang sangat tinggi atau sangat rendah akan mengakibatkan pembentukan saiz zarah yang lebih besar. Tambahan, dapat diperhatikan bahawa pengelompokan dan agregasi berlaku pada kebanyakan sampel. Nano-zarah maghemit memerlukan rawatan yang selanjutnya untuk meminimumkan pengelompokan dan agregasi. Oleh itu, tahap II dan II adalah diperlukan untuk menyelesaikan masalah ini. Nano-zarah superparamagnetik maghemit dengan saiz yang terkecil dipilih untuk melanjutkan ke tahap II dan III.

Nano-komposit maghemit-silika xerogel dihasilkan dengan teknik sol-gel. Nisbah jisim Fe_2O_3/SiO_2 yang berlainan diselidik. Analisis fasa yang dijalankan dengan menggunakan XRD mengesahkan bahawa nano-zarah yang disintesis dan yang dikapsul adalah maghemit. Imej TEM menunjukkan bahawa nano-zarah maghemit adalah dalam bentuk sfera dan bergabung homogen dengan matriks silika. Luas permukaan nano-komposit kurang daripada $40m^2/g$. Ini mungkin disebabkan oleh kenyataan bahawa majoriti liang-liang silika gel telah diisi oleh nanopartikal maghemit yang disintesis. Lebar liang yang dianggar bertambah apabila kandungan maghemit meningkat. Ini menunjukkan bahawa kuantiti liang-liang mini dan mikro telah diisi oleh nano-zarah maghemit. Pengurangan purata saiz kristalit nanopartikal maghemit yang diserak diperhatikan selepas proses pengkapsulan dibandingkan dengan nano-zarah maghemit yang disintesis. Ini menunjukkan bahawa pembubaran nano-zarah maghemit berlaku dengan kadar yang rendah. Namun, nisbah jisim nano-komposit Fe_2O_3/SiO_2 yang meningkat mengakibatkan purata saiz kristalit nanopartikal maghemit yang terbenam meningkat.

Nano-komposit maghemit-silica zarah dihasilkan dengan teknik pengubahsuaian sol-gel. Tujuan menukarkan matriks dari xerogel kepada bentuk zarahan adalah untuk meningkatkan luas permukaan dan mengekalkan sifat-sifatnya. Ini adalah teknik alternatif untuk menghasilkan nano-komposit kerana teknik ini adalah mudah, boleh dikilangkan, murah, cepat, boleh dihasilkan pada suhu bilik dan mampu mengawal komposisi, penyedaran kristal dan sifat-sifat nano-zarah maghemit dan nano-komposit maghemit. Selain itu, teknik ini tidak melibatkan surfaktan atau apa-apa pelopor. Dari mikrograf HRTEM, kehadiran celah atom kelihatan jelas pada zarah terbernam (inti), mengimplikasikan struktur kristalit. Manakala matriks adalah bahan bukan kristalit kerana tidak ada kisi hasil daripada pemerhatian. Keputusan EELS diperolehi daripada

inti menunjukkan kehadiran signal Fe-L_3, yang membuktikan bahawa zarah terbenam adalah sebatian berasas daripada besi. Pada tahap III, luas permukaan yang sangat tinggi diperolehi untuk nano-komposit yang dihasilkan (360-390m^2/g), berbanding dengan nano-komposit pada tahap II. Ini dapat mempertingkatkan kepekaan dan kereaktifan nano-komposit.

UNIVERSITY OF MALAYA

ORIGINAL LITERARY WORK DECLARATION

Name of Candidate: Ang Bee Chin (I.C/Passport No: 790417-07-5032)

Registration/Matric No. KHA 070012

Name of Degree: Doctor of Philosophy (PhD.)

Title of Project Paper/ Research Report/ Dissertation/ Thesis ("this work"):

Synthesis and Characterization of Maghemite Nanoparticles Dispersed in Silica Matrix

Field of Study: Advanced Materials (Nanotechnology)

I do solemnly and sincerely declare that:

1. I am the sole author/writer of this Work;
2. This Work is original;
3. Any use of any work in which copyright exists was done by way of fair dealing and for permitted purposes and any except or extract from, or reference to or reproduction of any copyright work has been disclosed expressly and sufficiently and the title of the Work and its authorship have been acknowledged in this Work;
4. I do not have any actual knowledge nor do I ought reasonably to know that the making of this work constitutes an infringement of any copyright work;
5. I hereby assign all and every rights in the copyright to this Work to the University of Malaya ("UM"), who henceforth shall be owner of the copyright in this Work and that any reproducing or use in any form or by any means whatsoever is prohibited without the written consent of UM having been first had and obtained;
6. I am fully aware that if in the course of making this Work I have infringed any copyright whether intentionally or otherwise, I may be subjected to legal action or any other action as may be determined by UM.

Candidate's Signature Date:

Subscribed and solemnly declared before,

Witness's Signature Date:

Name:

Designation:

ACKNOWLEDGEMENTS

I would like to take this opportunity to express my appreciation to those who have helped and supported me over the past four years. Without them, I would not finish my PhD programme and this thesis in a smooth manner.

My heartfelt thanks to my supervisor, Prof. Dr Iskandar Idris Yaacob for his patience, continuous guidance and motivation channeled throughout this research. He is very knowledgeable and dedicated in guiding me as he spent time with me whenever I faced challenges.

I would like to extend my utmost gratitude to my colleagues, Dr. Roslina Ismail, Dr. Abdul Hadi, Dr. Koay Mei Hyie, Ms. Yusrini Marita and Ms. Siti Hajar for their precious sharing of knowledge, ideas, assistance and fruitful discussions provided to accomplish this research successfully.

I would also like to express my sincere appreciation to the Faculty of Engineering, University of Malaya for providing me with all the facilities in the laboratories. Gracious thanks to the dedicated laboratory assistants Mr. Mohd Said Sakat, Mr. Nazarul Zaman and Mr. K. Kandasamy for giving their full co-operation while using the equipments. Special thanks to all the staff of Faculty of Engineering, and the Electron Microscope Unit, University of Malaya.

I am grateful for the financial support provided by University of Malaya's SLAI scheme and PPP Grant No. PS042/2007A and PS073/2008C.

Last but not the least, million thanks to my lovely family members who gave me full support in making this research work a success. Their support and encouragement during times of adversity have made me stronger.

I am also thankful for the effort and contribution shared by individuals whose names are not mentioned above.

Thank you so much.

TABLE OF CONTENTS

LIST OF FIGURES

LIST OF TABLES

CHAPTER 1: INTRODUCTION

1.1 GENERAL

Nanoscience is one of the hottest topics in the 20th century. Producing nanoparticles is an ongoing project in modern science. The use of nanoparticle materials offers many advantages due to their unique size and physical properties.

There has been a dramatic increase in interest for nanocrystalline maghemites due to their magnetic properties which are strongly dependent on the particles' and crystallites' sizes. This is especially so when the particle size reaches the nanometer scale (Morales et al., 1994). If the particle size is sufficiently small, the magnetic properties of nanoparticles transform from ferromagnetic to superparamagnetic. Moreover, maghemite nanoparticles have very high surface area compared with bulk materials. This means that the nanoparticles are attracted to the magnetic field and retain no residual magnetism after the field is removed. Additionally, maghemite nanoparticles have higher reactivity (Aslam et al., 2005). The properties of magnetic nanoparticles are a function of particle size, shape and surface chemistry (Kroll et al., 1996, Vollath et al., 1995). Among these, maghemite nanoparticles with a size range of 2-10nm are of particular importance.

The reason for maghemite nanoparticles being a material of interest is due to their potential applications in many areas such as high-density recording media (Martin et al. 2003; Bate, 1999), catalysis (Ida et al., 1997), bio-medical separation process (Gupta and Gupta, 2005), matrices for magneto-optical devices (Ennas et al., 1999), magnetic refrigeration (Mcmichael et al., 1829) and as controlled drug delivery systems (Bhatnagar et al., 1995). As mentioned previously, the size and distribution of the

particles are the major factors which influence the novel properties and applications of maghemite nanoparticles.

The most critical problem associated with maghemite nanoparticles is their tendency to agglomerate. Most of their unique properties will no longer be retained when the particles aggregate to micron size. This problem needs to be solved in order to maximize the useful nature of the individual particles. Therefore, there are efforts toward finding solutions to prevent the agglomeration and aggregation problem.

Much effort has been devoted toward the synthesis of maghemite nanoparticles due to their superior magnetic properties. The methods include precipitation, impregnation (Satterfield, 1991), a special precipitation technique known as Massart process (Bee et al., 1995), mechanical crushing of powder (Gomez et al., 1987), sol-gel preparation (Cannas et al., 2001), polymer matrix mediated synthesis (Hoh et al., 2003), usage of lauric acid as a non-aqueous medium (Jing and Wu, 2004) and using water in oil microemulsion (Yang et al., 2004, Ang and Yaacob, 2007). However, the agglomeration and aggregation problem still occurs after sometime. In addition, these methods require tedious washing procedure in order to remove residual surfactants.

Several attempts have been made to disperse the maghemite phase in a variety of matrix materials such as silica (Ennas et al., 1998; Monte et. al., 1997), porous glass (Borrelli et al., 1983) and polymer (Ziolo et al., 1992; Nguyen and Diaz, 1994). This technique is used to block the long-range magnetic dipole-dipole interactions among the nanoparticles even in the absence of an applied magnetic field (Vekas et al., 2006) using a physical barrier, which in turn, minimizes the agglomeration.

Maghemite nanocomposites consisting of maghemite nanoparticles dispersed in different matrices have been a subject of extensive investigation in recent years. SiO_2 is

one of the well-known matrices which possess unique properties such as high surface area, small pores and good electrical, acoustic and thermal insulations as well as bio-compatibility (Casas et al., 2001). It is believed that this type of nanocomposites will become increasingly important due to their stability. However, the instability in kinetics energy of the system poses a major disadvantage in this method, whereby sizes and shapes of the nanoparticles are difficult to control. All of the techniques used are one-step processes and therefore, these techniques are presently in the laboratory stage.

In this research, maghemite nanoparticles were produced by Massart's procedure and the effects of varying the $FeCl_2$ concentration on the properties of nanoparticles were investigated. This enables good monitoring and control of the size and homogeneity of the as-synthesized maghemite nanoparticles. In addition, the method retains the particles' particular identities without serious kinetic exchange involved. Following this, the size of the maghemite nanoparticles was further controlled by encapsulating them into a matrix by sol-gel technique. In this process, two different matrices conditions were used to produce iron-oxide nanocomposites, which are the network form of silica matrix (silica xerogel) and the particulate form of silica matrix. This is a novel approach for synthesizing these materials. This method is a two-step procedure to obtain homogeneous and well-coated particles.

Chapter 2 discusses the properties and magnetic behaviour of maghemite nanoparticles. In this chapter, previous researche on maghemite nanoparticles and maghemite nanocomposite are reviewed and the advantages of the fabrication techniques are briefly discussed. The potential applications of maghemites and maghemite nanocomposites are also included. The mechanisms of magnetite and

maghemite transformation are discussed and the basic properties of the matrix are presented at the end of this chapter.

Chapter 3 describes the experimental procedures for the synthesis of maghemite nanoparticles and the fabrication of the nanocomposites.

The results and interpretation of the data are presented in Chapter 4, and conclusions of the findings are given in Chapter 5.

Chapter 6 offers recommendations for further studies on the behaviour and applications of maghemite nanoparticles and maghemite nanocomposites.

1.2 OBJECTIVES

The objectives of this research are as follows:

1. To synthesize maghemite nanoparticles using Massart's procedure and to analyze the effects of varying the concentration of $FeCl_2$ on the properties and magnetic behaviour of as-synthesized maghemite nanoparticles.

2. To produce maghemite-silica xerogel nanocomposites by hydrothermal synthesis procedure (sol-gel method) and to determine the effects of varying the weight ratio of Fe_2O_3/SiO_2 on the size and properties such as morphology, product texture and magnetic behaviour of the maghemite-silica xerogel nanocomposites.

3. To produce maghemite-silica particulate nanocomposites by modified hydrothermal synthesis procedure (new modified sol-gel method) and to measure the effects of varying the weight ratio of Fe_2O_3/SiO_2 on the size and properties such as morphology, product texture and magnetic behaviour of the maghemite-silica particulate nanocomposites.

CHAPTER 2: LITERATURE REVIEW

2.1 IRON OXIDES

Iron oxides are defined as various oxides of iron, such as ferric oxide or ferrous oxide. Iron oxides are one of the most common compounds found in nature. There are 6 types of iron oxides, which are Fe_3O_4, FeO and four of them are polymorphs of Fe_2O_3 (α, β, γ, ε).

β-Fe_2O_3 (Braun and Gallagher, 1972) and ε-Fe_2O_3 are rare compounds which have been synthesized only in the laboratory. The former is obtained by dehydroxylation of β-FeOOH under high vacuum at 170^{o}C. ε-Fe_2O_3 was first reported in 1934 and named in 1963 (Trans et al., 1998). It exists both as a disordered, pure form and an ordered form which appears to be associated with hematite or maghemite. Its structure is intermediate between those of hematite and maghemite. It can be prepared in various ways and transforms to hematite at temperatures between 500^{o}C and 750^{o}C according to the method of preparation (Cornell and Schwertmann, 1996).

Table 2.1
Iron Oxides and their Descriptions

Types of Iron Oxides	Description
Maghemite  Figure 2.1: Image of Maghemite	**Chemical Formula:** γ –$Fe^{3+}_2O_3$ **Molecular Weight**: 159.69g (iron 69.94%, oxygen 30.06%) **Density**: 4.6g/cc **Colour**: Dark Brown **Characteristics**: Ferrimagnetic. Isostructural with magnetite but with cation deficient sites. Product of heating other Fe oxides in presence of organic matter.
Magnetite  Figure 2.2: Image of Magnetite	**Chemical Formula:** $Fe^{2+}Fe^{3+}_2O_4$ **Molecular Weight**: 231.54g (iron 72.36%, oxygen 27.64%) **Density**: 5.21g/cc **Colour**: Greyish black, Iron black **Characteristics**: Ferrimagnetic. Inverse spinel structure.
Hematite  Figure 2.3: Image of Hematite	**Chemical Formula:** α-Fe_2O_3 **Molecular Weight**: 159.69 (iron 69.94%, oxygen 30.06%) **Density**: 5.3 g/cc **Colour**: Reddish grey (fine), Black (coarse), Blackish red **Characteristics**: Corundum structure. Extremely stable, the end member of transformation of other oxides.
Wustite, FeO  Figure 2.4: Image of Wustite	**Chemical Formula:** $Fe^{2+}O$ **Molecular Weight**: 71.85g Density: 5.88g/cc **Colour**: Grey **Characteristics**: Cubic Structure with thermal expansion 33.9

From Table 2.1, magnetites are isostructural with maghemites but with cation deficient sites and both of them are ferrimagnetic. Due to its structural similarity with maghemite, magnetite is frequently used as a precursor compound of maghemite in laboratory synthesis. Both oxides have cubic inverse spinel structure, differing in the number of vacancies and in the occupancy of tetrahedral and octahedral cation sites (Cannas et al., 2001).

Iron oxides are found to be useful in many aspects. They are used as pigments, tape coatings and reinforcement fillers for polymer. The iron oxides are produced most widely for pigment production, followed by titanium (Cornell and Schwertmann, 1996).

In addition, the magnetic properties of magnetites and maghemits are also useful. The magnetic behaviour for both iron oxides is utilized as magnetic pigments in electronic recording media, ferrofluids, starting materials for the production of ferrites are used as permanent magnets, high storage recording media and semiconductor. (R.M. Cornell and Schwertmann, 1996). Ferrofluids are colloidal mixtures composed of nanoscale ferromagnetic or ferrimagnetic particles suspended in a carrier fluid, usually an organic solvent or water. A ferrofluid is superparamagnetic and can create liquid seals held in position by magnetic fields. One application of ferrofluids is to keep dust off the drive shafts of magnetic disc drives.

2.2 MAGNETISM

In this research, the magnetic properties of maghemite nanoparticles and maghemite nanocomposites are studied using hysteresis loops. The magnetic moment, saturation magnetization, coercivity and initial permeability are important parameters to consider in the investigation. Hence, a brief introduction regarding hysteresis loops is discussed.

2.2.1 Hysteresis loops

A great deal of information can be learned about the magnetic properties of a material by studying its hysteresis loop. A hysteresis loop shows the relationship between the changes of magnetic moment (**M**) over the strength of an applied magnetic field **(H).** It is often referred to as the B-H loop or M-H loop. An example of hysteresis loop is shown in Fig. 2.5.

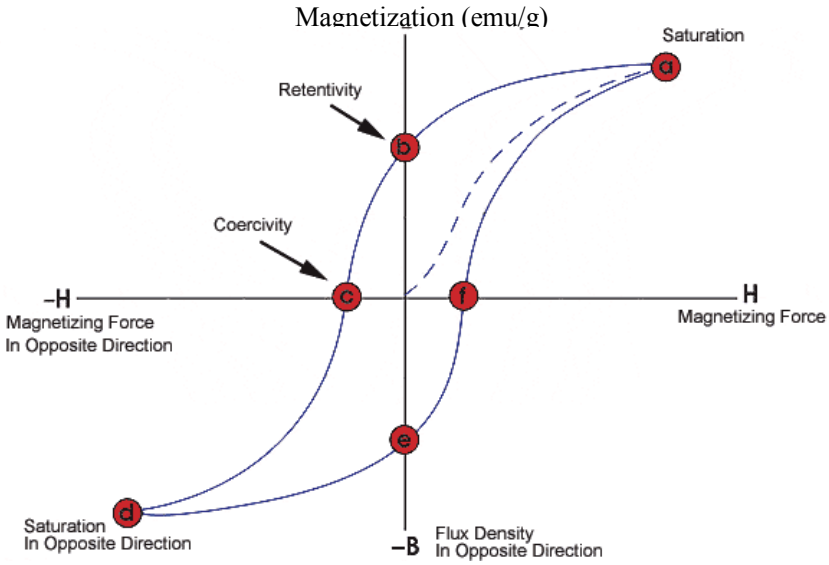

Figure 2.5:
Magnetization Curve

The loop is generated by measuring the magnetic flux of a ferromagnetic material while the magnetizing force is applied. A ferromagnetic material that has never been previously magnetized or has been thoroughly demagnetized will follow the dashed line as **H** is increased. As the line demonstrates, the greater the amount of current applied **(H+)**, the stronger the magnetic field in the component **(M+)**. At point "a" almost all of the magnetic domains are aligned and an additional increase in the magnetizing force will produce very little increase in magnetic flux. The material has reached the point of magnetic saturation ($\mathbf{M_s}$). When **H** is reduced to zero, the curve will move from point "a" to point "b". At this point, it can be seen that some magnetic flux remains in the material even though the magnetizing force is zero. This is referred to as the point of retentivity on the graph and indicates the remanent or level of residual magnetism in the material (remanent magnetic moment, $\mathbf{M_r}$). Some of the magnetic domains remain aligned while some have lost their alignment. As the magnetizing force is reversed, the curve moves to point "c", where the flux has been reduced to zero. This is called the point of coercivity on the curve ($\mathbf{H_c}$). The reversed magnetizing force has flipped enough of the domains so that the net flux within the material is zero. The force required to remove the residual magnetism from the material is called the coercive force or coercivity of the material.

As the magnetizing force is increased in the negative direction, the material will again become magnetically saturated but in the opposite direction (point "d"). Reducing **H** to zero brings the curve to point "e". It will have a level of residual magnetism equal to that achieved in the other direction. Increasing **H** back in the positive direction will return **M** to zero. It shall be noted that the curve did not return to the origin of the graph because some force is required to remove the residual magnetism. The curve will take a different path from point "f" back to the saturation point where it will complete the loop.

From the hysteresis loop, a number of primary magnetic properties of a material can be determined.

1. **Retentivity** (remanent magnetic moment) - A measure of the residual flux density corresponding to the saturation induction of a magnetic material. In other words, it is a material's ability to retain a certain amount of residual magnetic field when the magnetizing force is removed after achieving saturation.

2. **Coercive Force** - The amount of reverse magnetic field which must be applied to a magnetic material to make the magnetic flux return to zero.

3. **Permeability, μ -** A property of a material which describes the ease with which a magnetic flux is established in the component. It is the ratio of the flux density to the magnetizing force and is represented by the following equation:

$$\mu = M/H \qquad (2.1)$$

M Magnetization (emu/g)

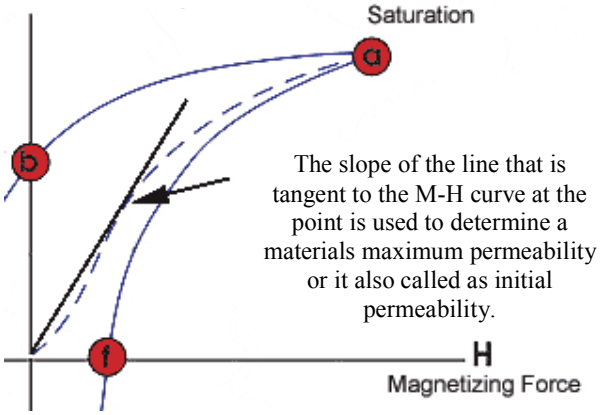

Figure 2.6:
Initial Permeability of Magnetization Curve

2.2.2 Classes of Magnetic Materials

The origin of magnetism lies in the orbital and spin motions of electrons and how the electrons interact with one another. The best method to introduce the different types of magnetism is to describe the manner by which materials respond to magnetic fields. Some materials are much more magnetic compared to others. The primary difference is that there is no collective interaction of atomic magnetic moments in some materials, whereas there is a very strong interaction between the atomic moments in other materials.

The magnetic behaviour of materials can be classified into the following five major groups (Moskowitz, 1991):

1. Diamagnetism
2. Paramagnetism
3. Ferromagnetism
4. Antiferromagnetism
5. Ferrimagnetism

Materials in the first two groups are those which do not exhibit collective magnetic interactions and are not magnetically ordered. Materials in the last three groups exhibit long-range magnetic order below a certain critical temperature.

2.2.3 Superparamagnetism (SPM)

Superparamagnetism occurs when the material is composed of very small crystallites (1-10 nm). In this case, when the temperature is below the Curie or Neel temperature (and hence the thermal energy is insufficient to overcome the coupling forces between neighbouring atoms), the thermal energy is sufficient to change the direction of magnetization of the entire crystallite. The resulting fluctuations in the direction of magnetization cause the magnetic field to average to zero. Thus, the material behaves in a manner similar to paramagnetism, except that instead of each individual atom being independently influenced by an external magnetic field, the magnetic moment of the entire crystallite tends to align with the magnetic field.

The energy required to change the direction of magnetization of a crystallite is called the crystalline anisotropy energy and depends both on the material properties and the crystallite size. As the crystallite size decreases, so does the crystalline anisotropy energy, resulting in a decrease in the temperature at which the material becomes superparamagnetic.

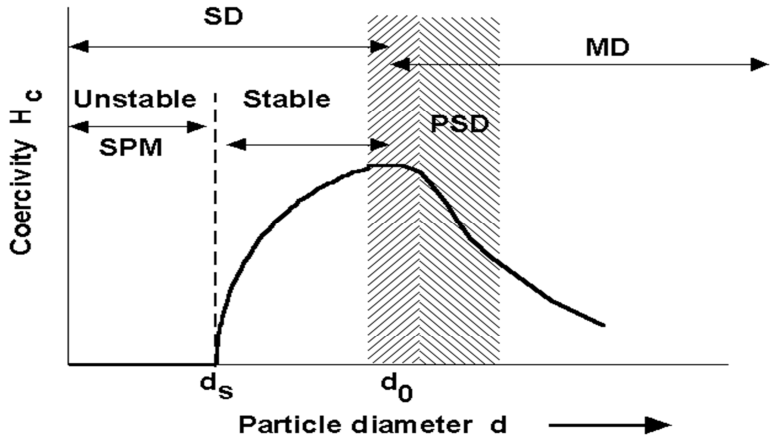

Figure 2.7:
Coercivity as a Function of Particle Size
(Cullity, 1972)

As the grain size decreases, a critical size will be obtained. This is a condition where the grain can no longer accommodate a wall. Below this critical size, the grain contains a single domain (SD). A SD grain is uniformly magnetized to its saturation magnetization. SD grains are very important. To change the magnetization of a MD grain. The domain wall needs to be translated in order to change the magnetization of a MD grain. This is a very energetically easy process, which can be accomplished in relatively low fields. Thus, MD grains are magnetically soft with low values of coercivities and remanence. However, the only way to change the magnetization of a SD grain is to rotate the magnetization. This is however, an energetically difficult process. Thus, SD grains are magnetically hard and have high coercivities and remanence.

The critical size for SD behaviour depends on several factors, which include saturation magnetization and the shape of the grain. Estimations of the SD-MD transition size are based on theoretical calculations. As particle size continues to decrease within the SD range, another critical threshold is reached, at which remanence and coercivity go to zero. When this happens, the grain becomes superparamagnetic. For superparamagnetic particles, the net magnetic moment is in zero field and at a temperature close to zero. It also show a net statistical alignment of magnetic moments when magnetic field is applied.

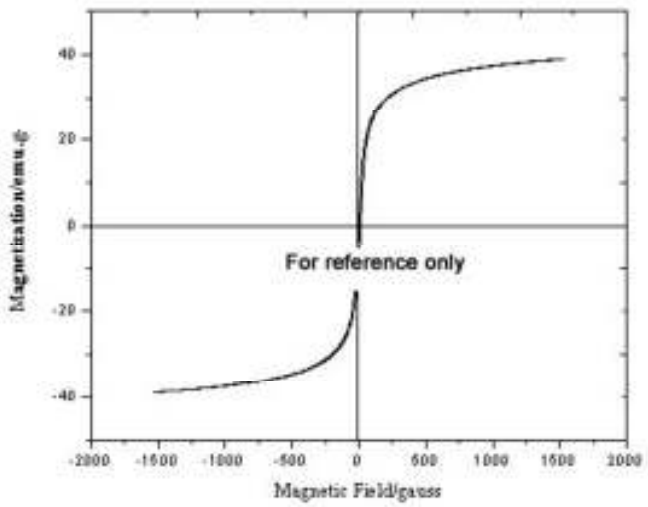

Figure 2.8:
Schematic Illustration of the Hysteresis Loop of a Superparamagnetic Nanoparticles (Sun, 2006)

SPM particles exhibit no remanence or coercivity, as shown in Fig. 2.13. The shape of the hysteresis loop is thus extremely thin or without loops at all. SPM grains show a very steep initial rise in magnetization with field, followed by a gradual increase to saturation. Typical values for hysteresis parameters are (Bruce, 1991):

$$M_r/M_s << 0.01 \qquad (2.2)$$

All relevant magnetic properties of nanoparticles such as coercivity, blocking temperature, saturation magnetization and remanent field are a function of particle size (Wang et. al, 2001).

The energy barrier (E_A) for rotation of magnetization orientation in a single domain particle has been described by the Stoner-Wohlfarth theory and is given by

$$E_A = KV \sin^2\theta \qquad (2.3)$$

where K is the anisotropy of the material, V is the volume of the nanoparticle and θ is the angle between an applied magnetic field and the easy axis of a nanoparticle. The

blocking temperature of a material is defined as the temperature for a given measurement time at which the moments are no longer blocked and are able to overcome the energy barrier. The coercivity can be considered as a measure of the magnetic field strength that is required to achieve changes of magnetization direction in a material. Lowering the anisotropy of a material will lower the activation energy barrier following the Stoner Wohlfarth theory and results in a lower blocking temperature and a lower applied field required for spin reversal and hence to a lower coercivity (Vestal and Zhang, 2003).

2.3 MAGNETIC NANOPARTICLES

Magnetism is a phenomenon by which materials assert an attractive or repulsive force on other materials. Some well known materials which exhibit magnetic properties are iron, some types of steels and the natural mineral, lodestone. For magnetic properties, the saturation magnetization, hysteresis loop and coercivity are important points to be discussed. They are highly dependent on the producing parameter, for example temperature, pH, particle size and surface area.

Recent advances in lithography and self-assembly have made it possible to produce magnetic wires and dots, magnetic nanowires, which may be used in a number of sensor applications. In the area where density and geometry can be controlled, it offers a paradigm shift for information storage. This could overcome the super-paramagnetic limit in current technologies (Panina, 2002, Allwood et. al., 2002).

Understanding the magnetic properties of nanometre scale particles is a central issue in the study of magnetic materials. This stimulates the interest of researchers to

further investigate the novel properties in nanosize compared with micro size. Structures in nanoscale have better advantages over structures in microscale.

Firstly, the ratio of surface to volume atoms is strongly enhanced. In other words, the surface properties will dominate the properties of the nanostructure. Since surfaces and interfaces are of chief importance, their quality must be controlled as well as their interior structures.

Secondly, the density of nanomaterials increases tremendously compared with density of micron size. This finding creates new concepts for data storage and very precise ideas are developed for new storage concepts of non-volatile memory devices, such as the magnetic random access memory MRAM, which is based on magnetic structures in nanometre size. (Daughton JM, 1992; Nordquist et.al., 1997). Eventually, the storage capacity is increased. Combination of a scanning tunneling microscope and chemical vapour deposition has been used for serial patterning of films with nanometre resolution to provide accuracy in positioning nanomagnets (Gider et. al,. 1996).

Thirdly, sufficient small nanostructures may behave superparamagnetically. This may destroy the desirable alignment of the magnetization and hence, the stored information. For example, the magnetic properties of iron oxide transform to superparamagnetic when the size decreases to the nanometre scale due to the low coercivity and magnetic saturation (Yee, 2003). Thus, the coercivity of a material is strongly connected to its size. According to Kodama (1999), when the particles size decrease to below a critical diameter, the particles become a single domain and the coercivity also decreases. The main reason is due to thermal effects. Thermal effects are strong enough to demagnetize previously saturated assembly of particles and create zero coercivity. This phenomenon is known as superparamagnetism.

Fourthly, they will lower the firing temperature and time as well as reduce energy consumption. Additionally, some nanocrystalline spinel ferrites exhibit different cation distribution compared with particles in the micro scale. Consequently, the magnetic properties are diverse compared with the corresponding bulk counterparts (Fatemi, 1999 and Rath, et. al., 2002)). Due to their novel properties, magnetic nanoparticle materials are normally used as the active component of ferrofluids, high-density biomedical applications, recording media and pigments.

2.3.1 Maghemite Nanoparticles

Maghemite is ferromagnetic at room temperature. The measurement of Curie temperature is difficult because maghemite is a metastable phase which will transform to hematite at temperatures about 350-450 ^{o}C. The Curie temperature has been estimated to be around 550-700 ^{o}C (Murad, 1988).

The magnetic structure consists of two sublattices corresponding to Fe located on tetrahedral (A) sites and octahedral (B) sites. The atomic moments within each sublattice are parallel, but those of the two sublattices are anti-parallel. Particles greater than 10nm in size are completely magnetically ordered at room temperature, whereas smaller particles (< 10nm) are superparamagnetic. Surface/interfacial effects influence the magnetic properties of ultrafine maghemite particles. Incomplete coordination of the atoms at the surface leads to a non-collinear spin configuration which reduces the magnetization of small particles. The specific saturation magnetization decreases linearly with increasing specific surface area (Mollard et al., 1977) and is also influenced by particle morphology (Boudeulle et al., 1983).

However, problems occur for most maghemite nanoparticles such as (a) they tend to form large aggregates, (b) their original structure may be altered if they are not stable enough, resulting in the alteration of magnetic properties and (c) they can undergo rapid biodegradation when they are directly exposed to biological systems. Therefore, a suitable coating is necessary to prevent such limitations. To make a stable suspension of particles for practical applications, their dimensions should be sufficiently small so that precipitation due to gravitational forces can be avoided. To achieve this particles should be made very uniform and ultra small (<5nm in diameter). This creates thermal stability for maghemite nanoparticles. The basic requirement is, to synthesize ultra small, coated and uniform particles having strong magnetic properties for their practical applications (Santra et al., 2000).

2.3.1.1 Applications of Maghemite Nanoparticles

Maghemite (γ-Fe_2O_3) is a technologically important compound widely used for the production of magnetic materials and catalysts. Maghemite nanoparticles exhibit superparamagnetic behaviour due to the small coercivity arising from a negligible energy barrier in the hysteresis of the magnetization loop. They have recently attracted considerable interest as optical-magnetic media in magneto-optical devices. Optical-magnetic media can be made by deposition of magnetic and optically transparent particles inside supporting transparent materials, and maghemite nanoparticles satisfy these requirements since they can be easily incorporated into ultrathin polymer films (Ennas, 1998).

In bio-applications, especially for in vivo applications, the main challenges currently consist of (i) reducing the nanoparticle size for passing through the majority of

biological membranes, (ii) ensuring their stability in pH conditions of biological fluids and (iii) tailoring their surface in order to functionalize and/or develop strong interactions with specific biological components (dye, drug or effector grafting) (Mornet et al., 2002). Therefore, maghemite nanoparticles is one of the useful magnetic nanoparticles which fulfil most of the requirement.

2.4 SILICA MATRIX

Silica gel has a wide range of applications, such as insulation (Pajonk, 2003), catalysis (Tillotson and Reynolds, 2003), controlled drug release (Kortesuo et al., 2001) and bioencapsulation (Luckarift et al., 2004), which depend directly on their physical properties and on the variety of nanostructures attainable. These materials consist in a 3-dimension SiO_2 network or colloidal particle structure obtained by the sol-gel process. The structure of the wet gel is firstly established by inorganic polymerization of a colloidal solution, prepared by hydrolysis and condensation of a precursor, namely, silicon alkoxide ($Si_x(OR)_{5-x}$). For tetra-functinonal alkoxides (x=1) such as tetraethoxysilane (TEOS), the overall hydrolytic polycondensation reaction can be written as (Toldas et al., 2000):

$$n\mathrm{Si}(\mathrm{OC_2H_5})_4 + m\mathrm{H_2O} \longrightarrow \mathrm{Si}_n\mathrm{O}_{(2n-(z+y)/2)}(\mathrm{OH})_z(\mathrm{OC_2H_5})_y + (4n-y)\mathrm{C_2H_5OH} \quad (2.4)$$

where $y = z - 2(2n-m)$. The initial formed dimmers and trimmers rapidly condense into cyclic siloxane (Si-O-Si) units, containing mostly four or six silicon atoms. The three dimensional network is built upon aggregation of the nanomeric particles formed by condensation of those cyclosiloxanes (Fidalgo and Ilharco 2004). The phase of the gel form is controlled by the hydrolysis and condensation rate.

2.4.1.1 Advantages of Silica Matrix

In all these applications the coating of particles is a very important issue. Coating assists in making the particles biocompatible, preventing aggregation and the degradation of maghemite nanoparticles. Moreover, the outer coating surface of the particles can be functionalized to allow the binding of drugs or bio-molecules to the system. Inorganic amorphous silica is bio-compatible, non-toxic and possesses hydroxyl surface groups which provide intrinsic hydrophilicity and allow surface attachment by covalent linkages of specific drugs or bio-molecules. Amorphous silica is also a heat resisting material with a low specific gravity, high surface area and good mechanical strength. The small pore size of silica gel can give rise to a very selective interaction with the adsorbed molecules, depending on their size, shape and chemical characteristics (Pacheco et al., 2006; Shao et al., 2008).

In addition, the thermal stability of silica gel is high and the porous texture of gels, i.e., pore size and pore structure, can be tailored. It is chemically stable and does not react with maghemite nanoparticles during the encapsulation process. Lastly, it is a non-magnetic material.

2.5 PROCESSING METHOD

The preparation of pure nanophase γ-Fe_2O_3 presents some difficulties partially arising from the different metal oxidation states, which can lead to the contemporary presence of various oxides (FeO, Fe_2O_3 and Fe_3O_4). Furthermore, Fe_2O_3 also exhibits crystallite phase of α- Fe_2O_3 (hematite), which is thermodynamically stable (Cannas et al., 1998) compared to maghemite.

Attempts have been made to stabilize γ-Fe_2O_3 nanoparticles using preparation techniques and coatings.

2.5.1 Synthesis of Maghemite Nanoparticles

2.5.1.1 Introduction

In general, there are two approaches to nanoparticle production which are commonly referred to as "top-down" and "bottom up". "Top-down" nanoparticles are generated from the size reduction of bulk materials and they generally rely on physical, the combination of physical and chemical, electrical or thermal processes for their production. In this study, the "bottom up" approach is used. The "bottom up" approach generates nanoparticles from the atomic or molecular level, and are thus, predominantly chemical processes. Commonly used techniques are crystallication/precipitation, sol-gel method, water in oil microemulsion, chemical vapour deposition and self assembly routes. Some processes may use a combination of these techniques (Hannink and Hill, 2006).

The synthesis of nanosize noble particles has attracted great interest due to the widespread use of these particles in applications. Nanosize particles have unique properties in comparison with their bulk counterparts such as thermal stability (Gleiter, 1989), unique magnetic properties (Ennas et al., 1998) and surface properties (Galina et al., 2009). Due to its unique properties, magnetic nanoparticles especially maghemite nanoparticles are increasingly required for potential applications. Maghemite nanoparticles are used as matrices for magneto-optical devices (Ennas et al., 1998) and high-density recording media (Martin et al., 2003), magnetic refrigeration (Mcmichael

et al., 1982), as magnetic fluids in controlled drug delivery systems (Bhatnagar & Rosensweig, 1995) and for bio-medical separation processes (Gupta and Gupta, 2005) as well as catalysis.

A number of strategies are now available to synthesize iron oxide nanoparticles. They are sol-gel processing (Cannas et al., 2001, Solinas et al., 2001), Massart's procedure (Bee et al., 1995), usage of hydrazine as a reducing agent of iron salts (Reddy et al., 2000), ball milling of lepidocrocite, γ-FeOOH (Gomez-Villacieros et al., 1987), hydrolysis and pyrolysis of akaganeite (β-FeOOH) and lepidocrocite (Herrero et.al., 1997), polymer matrix mediated synthesis (Hoh et al., 2004), usage of lauric acid as a non-aqueous medium (Jing and Wu, 2004), wet chemical processing (Okuda and Harada, 1985) and the use of microemulsion (Liu et al., 1999).

Researchers are facing difficulties to produce a monodisperse and uniform maghemite nanoparticles. A number of solutions have been devised by researchers, such as controlling the parameter of the synthesis process, temperature, pH, etc. Feltin and Pileni (1998) changed the temperature and the concentration of precursor during the precipitation of ferrous dodecyl sulfate micellar solution with methylamine. Wang et al. (2001) used a wire explosion (WEE) method to produce maghemite in a single step and produced uniform particles of 4nm in size successfully. Yaacob et al. (1994) and Ang and Yaacob (2007) used a special aqueous colloidal processing technique of using unilamellar vesicles and microemulsion as reactors, respectively. They reported the formation of particles with a mean diameter of less than 10nm. They managed to produce maghemite nanoparticles, however, the stability after a period of time remains a challenge for researchers.

Several authors reported that the preparation method used greatly affects the properties of synthesized nanoparticles (He et al., 2003; Landau et al., 1999: Kim and Hahn, 2001; Fang et al., 1998).

A classic method used to produce maghemite and magnetite nanoparticles is Massart's procedure. The use of Massart's procedure is another promising preparation technique for forming of magnetic nanoparticles. Particles with a defined shape and size can be prepared with this method (Tao et al., 2008; Liu et al., 2004). However, most of the studies were focused on the formation of pure magnetite and additional precursor materials were needed. The production of a single phase of maghemite nanoparticles and its stability is the main concern of this study. In addition, several authors also reported the evolution from γ to the α-Fe_2O_3 phase as a size-dependent transition as a decrease in particle size seems to provide better stability for γ-Fe_2O_3 (Ayyub et al., 1988; Grimm et al., 1997). Hence, the size of maghemite nanoparticles need to be further reduced to create a more stable condition for maghemite nanoparticles.

2.5.1.2 Massart's Procedure

Massart's procedure is a well established process created by Massart et al. (Bee et al., 1995). This process was used as it is an economic and versatile technique to synthesis large amounts of materials with different compositions and particle sizes.

Maghemite nanoparticles were synthesized by chemical coprecipitation (Massart's procedure) of ferric and ferrous ions in alkaline solution. In Massart's procedure, aqueous solutions of $FeCl_2.4H_2O$ (stabilized by adding a few drops of HCl) and $FeCl_3.6H_2O$ are mixed at a molar ratio of Fe^{3+}: Fe^{2+} of 2:1. Excessive amount of

ammonium hydroxide (NH_4OH) are added to the solution to ensure that the precipitation process is complete. The addition of NH_4OH causes instantaneous formation of black precipitates. After the precipitates have settled to the bottom of a beaker, the clear supernatant liquid is decanted. The precipitates are washed with deionized water. This process is repeated several times. The precipitates are then stirred in a solution of nitric acid solution (HNO_3). Nitric acid is used as an oxidation agent to oxidize the remaining iron oxides into maghemites. The particles are then recovered by centrifugation at 6000 rpm for 15 min. They are then completely oxidized to maghemites at 90°C in ferric nitrate solution, $Fe(NO_3)_3.9H_2O$. The particles are isolated again and dispersed in deionized water at pH≈2.5 in order to maintain the stability of maghemite nanoparticles. Powder specimens are obtained by drying the suspension in an oven at a slightly elevated temperature.

In precipitation techniques, the usage of various salts and controlling processing parameters such as the mixing and stirring rates, pH, solution concentrations, molar ratios and temperature enable the control of the particle size of powders. It is also possible to obtain ceramic powders with mixed cations and solid solutions.

Although coprecipitation reactions in aqueous medium for preparing iron oxide nanoparticles have been researched for more than 20 years, the difficulties in synthesizing iron oxide nanoparticles by coprecipitation are still present, controlling of the particle size, size distribution and in particular, the resultant phase.

2.5.2 Preparation of Maghemite Nanocomposites

2.5.2.1 Introduction

Maghemite nanoparticles tend to aggregate and agglomerate to reduce the energy associated with their high surface area to volume ratio. Most of the unique properties are only present in properly dispersed particles and are no longer retained when they form agglomeration.

Several techniques have been employed to control the agglomeration problem, such as coating the nanoparticles with surfactant and co-surfactant (Ang and Yaacob, 2007). The production of maghemite nanocomposites is a latest technique used to control the agglomeration problem. The generation of maghemite nanocomposites can be classified into two types, namely, the 1-step and 2-step procedure. In the 1-step procedure, maghemite nanocomposites are produced in a single step, whereby maghemite nanoparticles and silica gel are produced simultaneously. For this procedure, various methods have been used such as microemulsion (Santra et al., 2001; Yang et al., 2004; Maria et al., 2001), sol-gel (Cannas et al., 2001), arc-discharge (Pachecco et al., 2006), reactor (Barrada et al., 2005) and low-pressure flames (Janzen et al., 2003).

In the 2-step procedure, maghemite nanoparticles or silica gels are produced first and the encapsulation process is performed later. The 2-step procedure have been used by Mornet et al. (Mornet et al., 2002), Sartoratto et al. (Sartoratto et al., 2007) and Zhang et al. (Zhang et al., 1997) for producing iron oxide nanocomposites.

Although the 1-step procedure is more common compared to the 2-step procedure, the former method suffers from a major disadvantage, which is the size and shape of the nanoparticles are difficult to control. In addition, 1-step procedure usually

uses surfactants, reactors or stabilizers to help the dispersion process. It is known that such chemicals could not be completely removed (Santra et al., 2001) and the products are therefore unsuitable for bio-applications. Achieving particle size control in nanocomposites is certainly more difficult. Therefore, most of the works are devoted to a careful investigation of the relationship between particle size and magnetic properties rather that searching for the appropriate preparation conditions which favour particle size control.

In this study, the 2-step synthesis method is employed. Firstly, maghemite nanoparticles are synthesized using Massart's procedure. This process produces nanoparticles in the desired size range, which is less than 10nm. Secondly, the synthesized maghemite nanoparticles are encapsulated into silica gel matrix using sol-gel method. The nanoparticles are incorporated within the silica matrix. The matrices provide a physical barrier to reduce the interaction between the nanoparticles and hence, prevent their aggregation or agglomeration. This method enables the achievement of homogeneous and well dispersed particles within silica matrix.

Table 2.2 summarizes some of the selected properties for nanocomposites based on different techniques reported in literature.

Table 2.2:
Summary of Current Research on Magnetic Nanocomposites

Authors	**Technique used**	**Results**	**Disadvantages**
Santra et al. (2001)	• 1-step technique • Synthesis of γ-Fe_2O_3 by W/O microemulsion of iron salts ($FeCl_2$ and $FeCl_3$) and 2 different bases (NaOH and NH_4OH). • TEOS is added to both microemulsion solution • Purged nitrogen gas during mixing in ultra sonicator	• Surfactant is **not** completely removed • Particle size (1-2nm) • Silica coating layer (1-2nm) • Silica aerogel matrix	• Images are poor, indicated the presence of surfactant. • Surfactant affects the stability and shape of maghemite. • Low magnetization even at 20kOe of applied field. • Purging is needed throughout the experiment
Cannas et al. (2001)	• 1-step technique • TEOS is added to a solution containing iron nitrate dissolve in ethanol-ethylene glycol. • 17-20days of gelation • Drying 140^oC for 24h • Heat treatment until 900^oC	• Presence of maghemite is observed only after heat treatment of 900^oC. • Presence of hematite for sample with higher wt % of Fe (28wt%) • Particle size (3-4nm) for 16.9wt % Fe and 5-6nm for 28wt% of Fe • M_s = 34-43emu/g • Silica aerogel matrix	• Hardly produce pure maghemites • The magnetism behaviour is ferromagnetic, with loop not superparamagnetic • Need heat treatment up to 900^oC. • Long gelation period.
Mornet et al. (2002)	• 2-step technique • First Massart's synthesis followed by W/O microemulsion and hollow sphere synthesis. • Surfactants used:	• Maghemite = 5-10nm, BET = 130m^2/g. • Particulate gel appears at pH2.5 with embedded maghemite nanoparticles,	• Use of surfactants • Magnetism is ferromagnetic

	Brij®30/AOT. • 20h stirring	BET= 440m^2/g • Maghemite nanocomposite is stable for pH higher than 5 and remain unaltered until 1273K (1000^oC).	
Pacheco et al. (2006)	• 1-step procedure • Experiment involving 3000^oC	• M_s = 160emu/g • Ferromagnetic • Magnetite nanocomposite • Particle size = 10-30nm • BET = 30.6m^2/g	• Complicated arc-discharge method which involves 3000^oC • Silica source is purchased from Sigma-Aldrich and ball-milled for 16 h to obtain microscale oxidized silicon powder. • Costly
Yang et al. (2004)	• 1-step technique • Synthesis γ-Fe_2O_3 by W/O microemulsion of iron salts ($FeSO_4$ and $FeCl_3$) and NH_4OH. • TMOS is added to both microemulsion solution • Purged nitrogen gas during mixing in ultra sonicator	• Particle size = 5-7nm • Mixed product of magnetite and maghemite.	• Use of surfactant • Produce a mixed product • Purging is needed throughout the experiment
Maria et al. (2001)	• Same method as Cannas but different wt% of Fe for xerogel, • Supercritical drying process is carried out	• Maghemite nanocomposites (xerogel and aerogel) are obtained after heat treatment of 900^oC. • High surface area, in the range of 500-800m^2/g	• Heat treatment needed • Long gelation time

Barrado et al. (2005)	Method 1: • 1-step procedure using reactor • pH 10 • Bubbling through the solution for 1h • Heat at 100^{o}C for 48h Method 2: • 2-step method using reactor • pH10 • Stirring for 24 h and heating for 48h	Method 1 • less magnetic properties • only magnetite obtained Method 2 • Obtained hematite and is unstable. Hematite will changes according to temperature.	• Irregular morphology of nanocomposites • Non-stable iron oxides formed • Involvs reactor, which is costly.
Sartoratto et al. (2007)	• 2-step procedure • Molar ratio = 0.013and 0.020 Fe/Si • Sol-gel system is TEOS/Ethanol/water/H^{+} • 30 gelation days • Heating in the range of 120-1400^{o}C for 1h	• As-synthesized maghemite nanoparticles doped with a small amount of Fe(II) ions. • Stability of maghemite nanoparticles is up to 300^{o}C • Stability of 0.02 Fe/Si nanocomposites is up to 900^{o}C	• Stability of maghemite nanocomposties only up to 300^{o}C for Fe/Si molar ratio more than 0.02 • Long gelation time
Solinas et al. (2001)	• 1-step procedure by sol-gel • Study the effects of varying surface/volume (S/V) ratio • Study the effects of the heat treatment on the formation of γ-Fe_2O_3	• Stability of maghemite nanoparticles is up to 400^{o}C • Gelation time depends on the gelation temperature and S/V ratio • Particle size is around 10nm to 25nm	• Particle size is big (10-25nm) • Long gelation time • Stability of γ-Fe_2O_3 only up to 400^{o}C.

Zhang et al. (1997)	• 2-step procedure • Iron oxides are prepared by coprecipitation technique and coated within silica by sol-gel.	• Particle size is 4-5nm. • Superparamagnetic	• Some elongated particles are found
Janzen et al. (2003)	• 1-step procedure • Use low-pressure premixed flames of hydrogen and oxygen	• Particle size was 3-7nm. • Maghemites exhibit superparamagnetic behaviour	• Complicated process • High cost

2.5.2.2 Sol-Gel

The main challenge in the synthesis of nanopartricle is the attainment of well defined particle size and morphology. The use of an inorganic matrix as a host for nanocrystalline particles can provide an effective way for tailoring uniform particle size and controlling the homogeneous dispersion of ultrafine metal oxide clusters. The sol-gel derived oxide matrices act as excellent supports for the dispersion of metal or metal oxide magnetic particles. In this case, the process is frequently based on the hydrolysis of the precursors, such as tetraethoxysilane (TEOS) and subsequent condensation of hydrolysed TEOS in a medium containing hydroalcholic solution of the metal salt.

The sol-gel process, also known as chemical solution deposition, is a wet-chemical technique widely used in the fields of materials science and ceramic engineering. Such methods are used primarily for the fabrication of materials (typically a metal oxide) starting from a chemical solution (or *sol*) that acts as the precursor for an integrated network (or *gel*) of either discrete particles or network polymers. Typical precursors are metal alkoxides and metal chlorides, which undergo various forms of hydrolysis and polycondensation reactions (*Internet Reference*, 29/9/2010a).

The sol-gel process allows the fabrication of materials with a large variety of properties: ultra fine powders, monolithic composites, thin film coatings and aerogel. Sol-gel chemistry is a remarkably versatile approach for fabricating materials. Scientists have used it to produce the world's lightest materials and some of its toughest ceramics.

In typical sol-gel syntheses, metal or main-group element compounds undergo hydrolysis and condensation reactions, giving gel materials with extended three-dimensional structures or in particulate form if the hydrolysis and condensation rates are accelerated. As shown in the following equation for silicon, the addition of an acid or base catalyst to a solution of an alkoxysilane reagent, such as tetramethoxysilane (TMOS), water, and methanol leads to the hydrolysis of Si-OMe bonds to form Si-OH functional groups:

$$\underset{\text{TMOS}}{Si(OMe)_4} + H_2O \xrightarrow{MeOH} Si(OH)_4 + 4MeOH \xrightarrow{-2H_2O} SiO_2 \text{ gel} \quad (2.4)$$

Subsequent elimination of water from two such Si-OH groups gives eventually an extended silica gel matrix (known as xerogel when dry). Since hydrolysis and condensation reactions occur concurrently, monomeric silanols proceed to xerogel through oligomeric and polymeric intermediates. As these reactions progress, the viscosity of sol-gel solutions increases and can reach a "spinable" stage at which point thin films or fibers can be produced. Otherwise, xerogel products are obtained as porous powders or monoliths which assume the shape of their containers. If desired, residual Si-OH groups remaining in the xerogel product can be removed at an elevated temperature to give a fully densified SiO_2.

Sol-gel methods are commonly used to prepare nanocomposite materials because these conversions occur readily with a wide variety of precursors and can be

conducted at or near room temperature. In addition, the gel products frequently have properties ideal for desired applications. Porous ceramic xerogel of high surface area can serve as supports for chemical catalysts (Cauqui and Rodriguez-Izquierdo, 1992; Elaloui et al., 1997) and thin film deposition is useful for materials possessing desired optical or magnetic properties (Nalwa, 2002).

CHAPTER 3: EXPERIMENTAL PROCEDURE

3.1 MATERIALS AND METHODS

This chapter describes the materials used and the experimental setup of this study.

3.1.1 Raw Materials and Experimental Procedure

The study consisted of three main stages of experiments. All stages included characterization of the prepared samples. A flowchart of the research procedure is shown in Fig. 3.1.

The first stage involved the synthesis of maghemite nanoparticles using Massart's procedure. The raw chemicals used for preparation of maghemite nanoparticles were ferrous chloride hexahydrate (Sigma), ammonium hydroxide (Fisher Chemicals), ferric chloride (Fisher Chemicals), ferric nitrate (AJAX Chemicals), hydrochloric acid (AJAX Chemicals) and nitric acid (Merck).

The second stage of this study involved the preparation of maghemite nanocomposites in silica xerogel matrix. The nanocomposites containing as-synthesized maghemite nanoparticles and SiO_2 xerogel were prepared using sol-gel procedure. The raw materials used for silica xerogel were tetrapropyl ammonium hydroxide solution, TPA (Aldrich) and tetraethyl orthosilicate, TEOS (Aldrich) and deionized water.

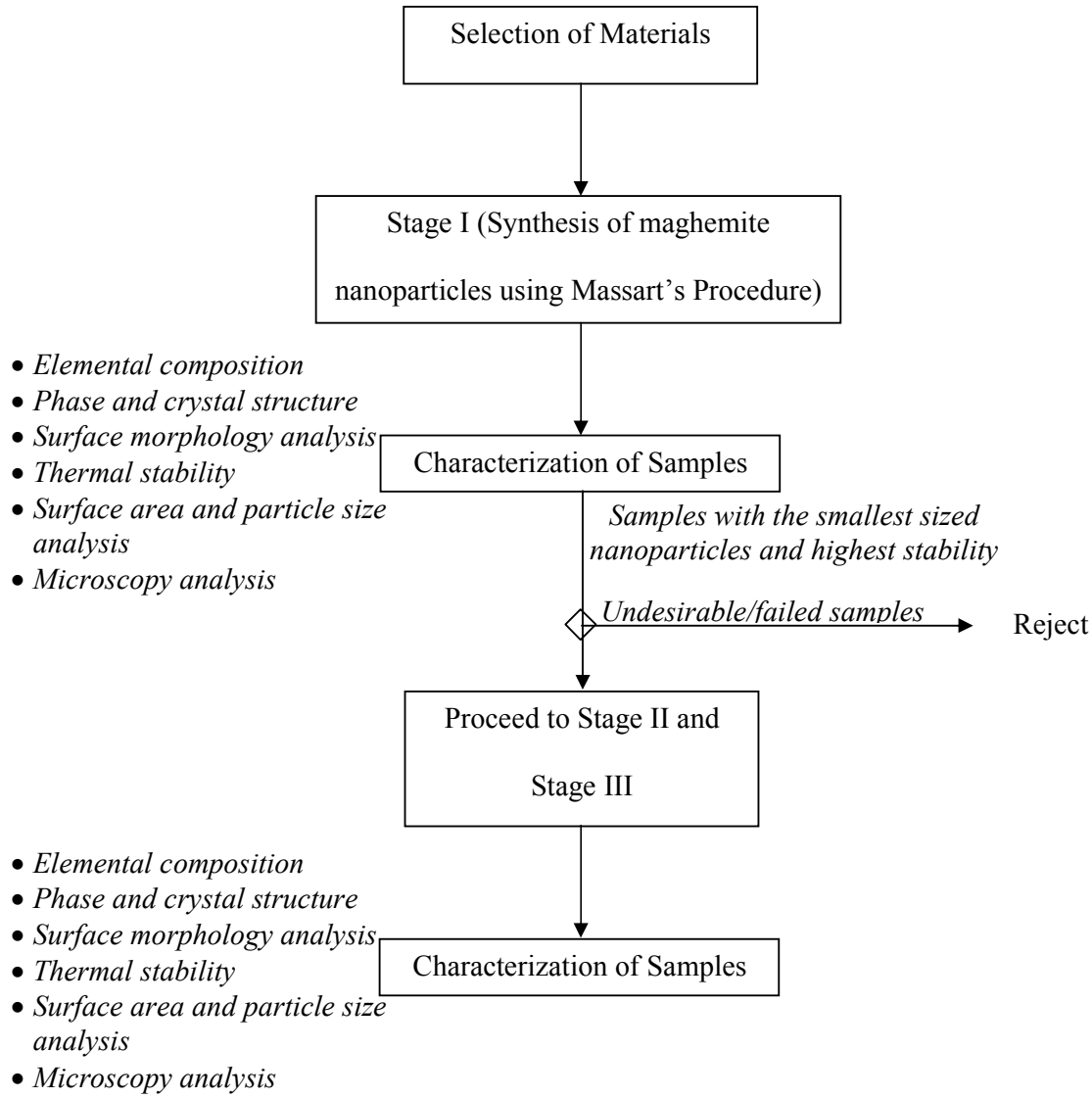

Figure 3.1:
Flowchart of the Research Methodology

The third stage of this study involved the preparation of maghemite nanocomposites in particulate form of silica matrix. The modified sol-gel method was used for the preparation of the nanocomposites. The raw materials used were tetraethyl orthosilicate, TEOS (Aldrich), ethanol (Ajax Chemical), ammonium hydroxide (Fisher Chemicals) and deionized water.

Deionized water with a resistivity of approximately 16-18 MΩ/cm was obtained using ELGA ultra analytic deionizer, and was used for the preparation of the solutions. All chemicals were of analytical grade and were used without any further purification.

3.1.1.1 Synthesis of Maghemite Nanoparticles using Massart's Procedure

Maghemite nanoparticles were synthesized by chemical coprecipitation (Massart's procedure) of ferric and ferrous ions in alkaline solution. Aqueous solutions of $FeCl_2.4H_2O$ (stabilized by the addition of a few drops of HCl) and $FeCl_3.6H_2O$ were mixed at a Fe^{3+}: Fe^{2+} molar ratio of 2:1. Excessive amount of ammonium hydroxide (NH_4OH) was then added to the solution to ensure that the precipitation process was complete. The addition of NH_4OH caused instantaneous formation of black precipitates. After the precipitates settled at the bottom of the beaker, the clear supernatant was decanted. The precipitates were then washed with deionized water and the process was repeated several times. The precipitates were stirred in nitric acid solution (HNO_3). Nitric acid was used as an oxidation agent to oxidize the remaining iron oxide into maghemite. The particles were then recovered by centrifugation at 6000 rpm for 15 min. The particles were completely oxidized to maghemites at 90°C in ferric nitrate solution. The particles were isolated again and then peptized in deionized water (Ang and

Yaacob, 2006). Powder specimens were obtained by drying the suspension in an oven at a slightly elevated temperature. The flowchart of the process is shown in Fig. 3.2.

Five samples were produced using different $FeCl_2$ concentrations: 0.1M, 0.8M, 1.0M, 1.2M and 1.5M. The samples were labelled as M01, M08, M10, M12 and M15 for0.1M, 0.8M, 1.0M, 1.2M and 1.5M, respectively. The concentrations of the $FeCl_3$ was varied accordingly in order to maintain a Fe^{3+}: Fe^{2+} molar ratio of 2:1.

The maghemite nanoparticles were characterized using XRD, TGA, TEM, DLS, BET and AGM.

Figure 3.2:
Flowchart of Massart's Procedure for Stage I

3.1.1.2 Preparation of Maghemite-Silica Xerogel Nanocomposite

The maghemite nanocomposites containing as-synthesized maghemite nanoparticles and SiO_2 xerogel were prepared using sol-gel procedure. A typical sol-gel precursor mixture consisting of TEOS, tetrapropylammonium hydroxide solution and deionized water was used. The weight ratio of the precursors was 5:7:3, respectively. The sol-gel mixture was stirred overnight. The maghemite nanoparticles were then dispersed in the aged sol-gel mixture by stirring for an additional 3 hours. The system was then heated for a period of 3 days at 140^{o}C. The product was washed with deionized water by centrifugation at 6000 rpm for 5 min to remove the un-encapsulated maghemite nanoparticles. The flowchart of the process is shown in Fig. 3.3.

Various weight ratios of Fe_2O_3/SiO_2 were prepared and investigated. The samples were labelled as MN010, MN025, MN050, MN100 and MN150, corresponding to 0.14, 0.35, 0.7, 1.4 and 2.08 weight ratios of Fe_2O_3/SiO_2, respectively. A control sample of SiO_2 was prepared (without addition of maghemite nanoparticles) and labelled as S1. The nanocomposites were characterized using XRD, TGA, TEM, FESEM, BET and AGM.

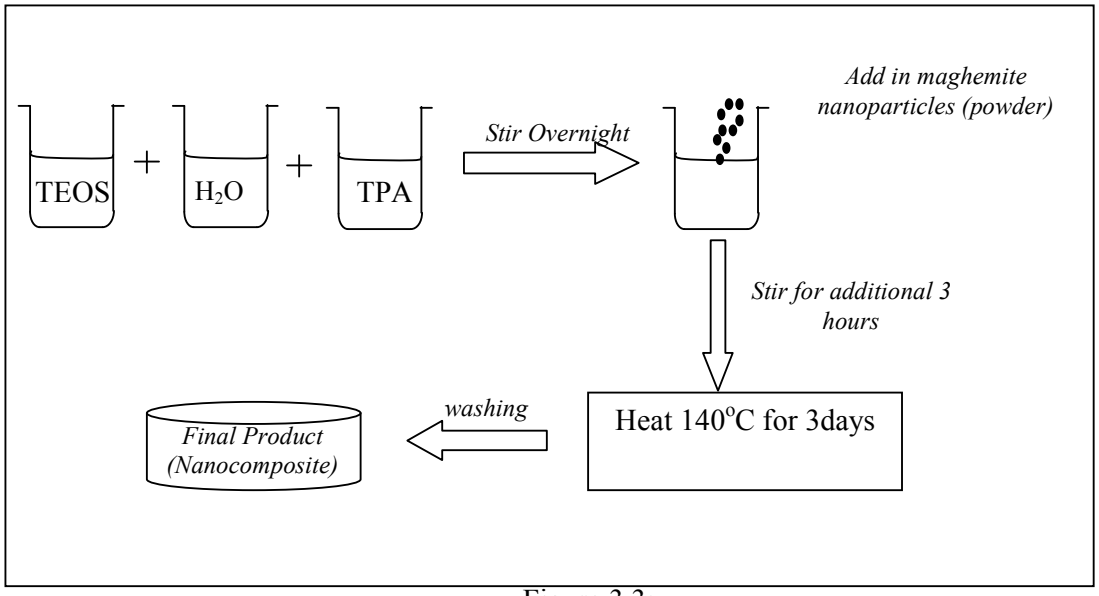

Figure 3.3:
Flowchart of Sol-Gel Process for Stage II

3.1.1.3 Preparation of Maghemite-Silica Particulate Form Nanocomposites

In addition, the process for preparing silica xerogel matrix was modified to form silica matrix in particulate form. The purpose of changing the matrix from xerogel to particulate form was to increase the surface area and hence increase the sensitivity while maintaining its properties.

The maghemite nanocomposites consisting of as-synthesized maghemite nanoparticles and particulate form of SiO_2 matrix were prepared using modified sol-gel procedure. A typical sol-gel precursor mixture consisting of TEOS and deionized water was used. The weight ratio of the precursor was 5:3, respectively. The sol-gel mixture was stirred for 15 min in ultrasonic bath. The maghemite nanoparticle powders were then dispersed in ethanol (6 ml) followed by dispersion in the aged sol-gel mixture for an additional 1 hour in ultrasonic bath. The pH of the solution was retained at 10 to achieve the particulate form of silica matrix. In this analysis, ammonium hydroxide solution was used to control the pH level. Following this, the system was heated for a

period of 3 days at 140°C. The product was washed with deionized water by centrifugation at 6000 rpm for 5 min to remove un-encapsulated maghemite nanoparticles. The flowchart of the process is shown in Fig. 3.4.

A number of selected weight ratios of Fe_2O_3/SiO_2 were prepared and investigated. The weight ratios of Fe_2O_3/SiO_2 investigated were 0.35, 0.7 and 1.4 and labelled as MNP025, MNP050 and MNP100, respectively.

This method is a promising alternative technique for fabrication of nanocomposites as it is simple, manufacturable, inexpensive and fast. Additionally, it is prepared at room temperature and the composition, crystalline distribution and properties of maghemite nanoparticles and maghemite nanocomposite can be controlled. Moreover, no surfactants or other unnecessary precursors are involved.

The nanocomposites were characterized using XRD, TGA, FESEM, TEM, HRTEM, BET and AGM.

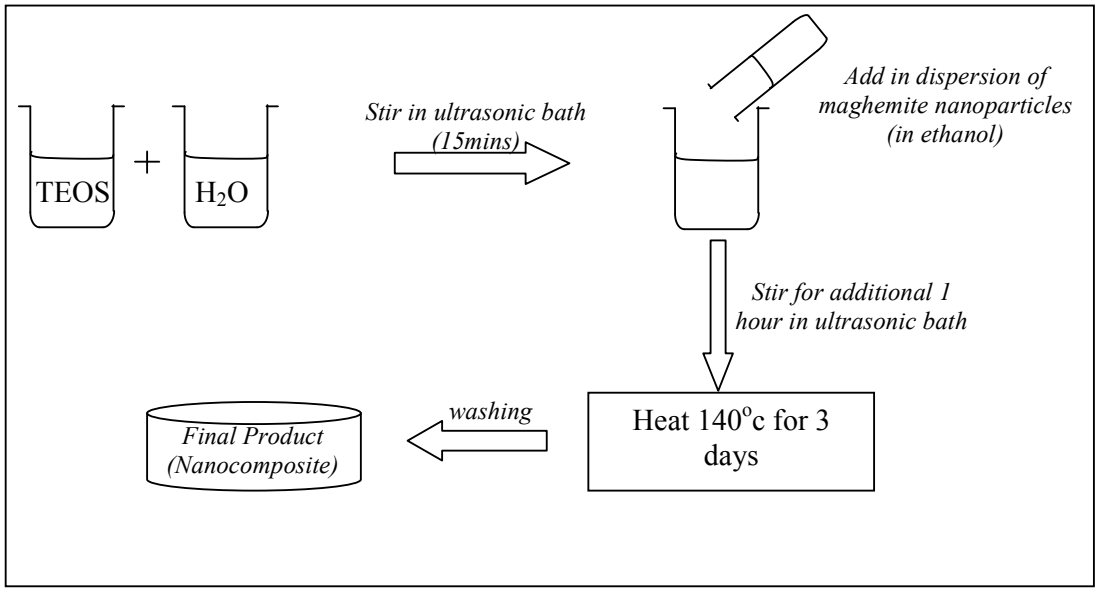

Figure 3.4:
Flowchart of Sol-Gel Process for Stage II

CHAPTER 4: RESULTS AND DISCUSSION

4.1 SYNTHESIS OF γ-Fe_2O_3 NANOPARTICLES BY MASSART'S PROCEDURE (STAGE I)

In this research, maghemite nanoparticles were produced by Massart's procedure and the effects of varying the $FeCl_2$ concentration on the physical and magnetic properties of nanoparticles were investigated.

4.1.1 Formation of Maghemite (γ-Fe_2O_3) Nanoparticles

Five samples were prepared for this study. The steps for the formation of maghemite nanoparticles are summarized as follows:

a) NH_4OH solution was added into a mixture of ferrous chloride ($FeCl_2$) and ferric chloride ($FeCl_3$) solution. Dark brown precipitates were observed. Excess NH_4OH solution changed the colour of the precipitates to black, which indicates that magnetite precipitates (Fe_3O_4,) were obtained.

$$FeCl_2 + 2FeCl_3 + NH_4OH \longrightarrow Fe_3O_4 + 4HCl + 4\ NH_4Cl \quad (4.1)$$

b) After washing by centrifugation, the particles were peptized in 2M HNO_3 solution under vigorous stirring in order to create positive surface charges.

c) The resultant Fe_3O_4 precipitates were oxidized with $FeNO_3$ solution until the Fe^{2+}/Fe^{3+} ratio in the particles was lower than 0.05, which indicates that magnetites were converted to maghemites.

$$2Fe_3O_4 + ½\ O_2 \longrightarrow 3(\gamma\text{-}Fe_2O_3) \quad (4.2)$$

d) The precipitates were isolated by a magnet. It was then washed in deionized water and dispersed in deionized water at pH≈2.5 in order to maintain the stability of maghemite nanoparticles.

In this study, five samples were prepared with different $FeCl_2$ concentrations. The details of the samples are listed in Table 4.1.

Table 4.1:
$FeCl_2$ and $FeCl_3$ Concentrations of Samples

Sample	$FeCl_2$ Concentration, (M)	$FeCl_3$ Concentration, (M)
M01	0.1	0.2
M08	0.8	1.6
M10	1.0	2.0
M12	1.2	2.4
M15	1.5	3.0

4.1.2 Thermal Properties

Fig. 4.1 shows the TGA curves of samples M01, M08, M10, M12 and M15. The curves exhibit similar behaviour. A weight loss of about 18-33 % is observed upon heating over the range of room temperature to 700 ^{o}C, as shown in Table 4.2. Most of the weight loss occurs below 230 ^{o}C, which is mainly due to the removal of solvent and dehydration process. No obvious weight loss is observed within the range of 230 – 700 ^{o}C, which indicates that the maghemite nanoparticles are thermally stable. On the contrary, a minor weight loss occurs around 255 ^{o}C due to transformation of dehydroxylation of the lepidocrocite structures leading to the formation of maghemite (Dinesen et al., 2001) as well as the aggregation of unstable maghemite nanoparticles which transform into hematite and magnetite at around 380^{o}C (Sartoratto et al., 2006, Grimm et al., 1997).

Nanocrystalline maghemites, in which the oxygen atoms are arranged in a face-centered cubic (FCC) structure, is of a spinel-type phase. When the temperature increases to a certain value, the metastable nanocrystalline maghemites is reconstructed into stable magnetites, whereby the oxygen atoms are from hexagonal close-packed (HCP) structure. The thermal studies show that the maghemites are stable up to 700 ^{o}C. This is due to the extremely small size (less than 10 nm size range) of the as-synthesized maghemite nanoparticles. It is well known that the maghemite to magnetite transition occurs at higher temperatures with decreasing grain size. The reduction in grain size of maghemite nanoparticles enhanced their thermal stability. (Ye et al., 1998; Ayyub et al., 1988; Schimanke and Martin, 2000).

Table 4.2:
Percentage Weight Loss of Samples

Sample	Weight loss (%)
M01	32.52
M08	28.58
M10	18.78
M12	21.05
M15	19.55

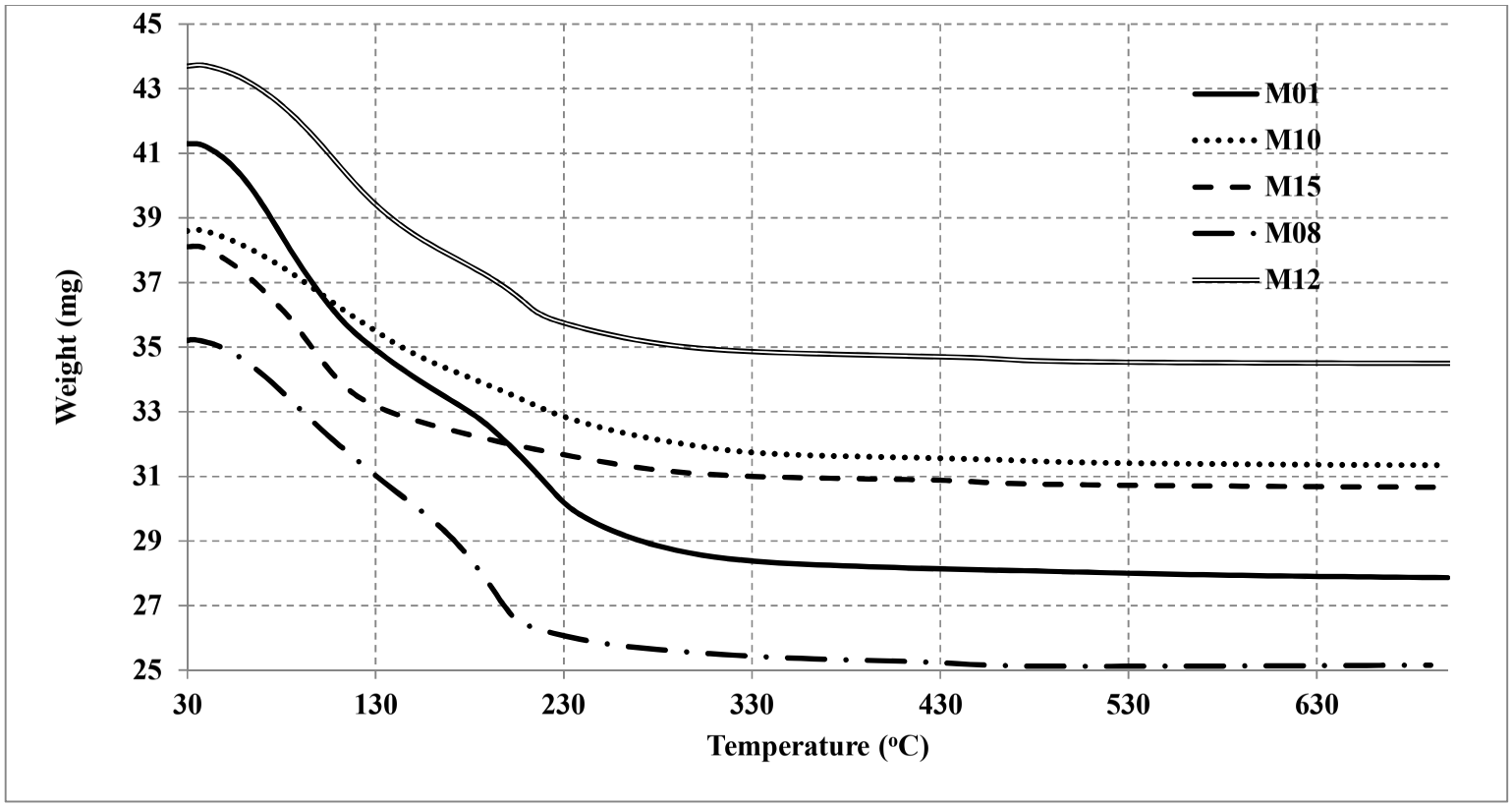

Figure 4.1:
TGA Curves for Samples

4.1.3 Phase and Crystal Structure

The XRD patterns of the as-synthesized γ-Fe_2O_3 nanoparticles are shown in Fig. 4.2. The characteristic peaks corresponding to (220), (311), (400), (511), and (440) planes are clearly observed and located at about 2θ = 30.09 °, 35.60 °, 43.28 °, 56.74 °, and 62.86 °, respectively. The peaks are very close to the ones which belong to the ICDD PDF Card Number 39-1346, as shown in Table 4.3. Analysis of the XRD patterns reveals that the particles are maghemite (ICDD PDF Card No. 39-1346).

Table 4.3:
Comparison between the XRD Characteristic Peaks of Samples and Standard

As-prepared γ-Fe_2O_3		**ICDD PDF No. 39-1346**	
Angle (2θ)	**Miller indices (hkl)**	**Angle (2θ)**	**Miller indices (hkl)**
30.085	220	30.266	220
35.595	311	35.661	311
43.275	400	43.321	400
56.835	511	57.323	511
62.855	440	62.983	440

The results were confirmed further by calculating the lattice parameter of the samples (Gunzler and Williams, 2001). The actual lattice parameter of the samples was also determined using the data extracted from the XRD patterns, as shown in Tables 4.4 - 4.8 and Fig. 4.3. The lattice parameters calculated are within the range of 8.33 - 8.35 Å. It is noted that the cited lattice parameter is 8.33 and 8.396 Å for bulk maghemite and magnetite, respectively. Therefore, the values obtained indicate that the particles are more likely to be maghemite rather than magnetite. It is emphasized that the lattice parameter for sample M10 is equal to the value for bulk maghemite.

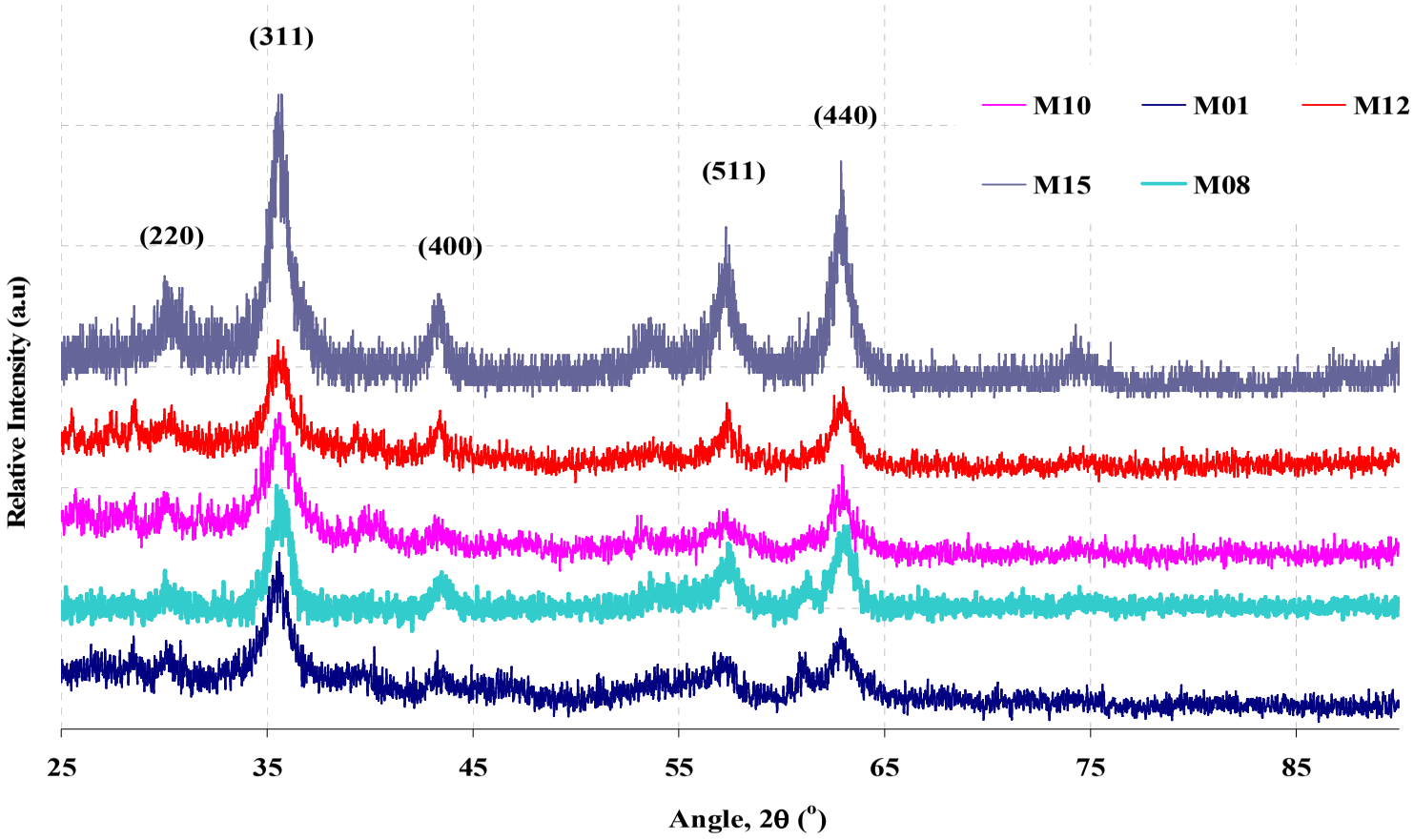

Figure 4.2:
XRD Curves for Samples

Table 4.4:
Lattice Parameter for Sample M01

2θ (°)	d-spacing (Å)	Miller indices (hkl)	Lattice Constant (Å)
30.375	2.939	220	8.31
35.484	2.527	311	8.38
43.275	2.088	400	8.35
57.425	1.603	511	8.33
62.875	1.476	440	8.35
		$a_{average}$	**8.34**

Table 4.5:
Lattice Parameter for Sample M08

2θ (°)	d-spacing (Å)	Miller indices (hkl)	Lattice Constant (Å)
30.055	2.969	220	8.40
35.564	2.521	311	8.36
43.485	2.078	400	8.31
57.485	1.601	511	8.32
62.805	1.478	440	8.36
		$a_{average}$	**8.35**

Table 4.6:
Lattice Parameter for Sample M10

2θ (°)	d-spacing (Å)	Miller indices (hkl)	Lattice Constant (Å)
30.505	2.927	220	8.28
35.579	2.520	311	8.36
43.325	2.086	400	8.34
57.365	1.604	511	8.34
62.851	1.477	440	8.35
		$a_{average}$	**8.33**

Table 4.7:
Lattice Parameter for Sample M12

2θ (°)	d-spacing (Å)	Miller indices (hkl)	Lattice Constant (Å)
30.306	2.945	220	8.33
35.586	2.520	311	8.36
43.405	2.082	400	8.33
57.475	1.601	511	8.32
62.8445	1.477	440	8.35
		$\mathbf{a_{average}}$	**8.34**

Table 4.8:
Lattice Parameter for Sample M15

2θ (°)	d-spacing (Å)	Miller indices (hkl)	Lattice Constant (Å)
30.205	2.955	220	8.36
35.569	2.521	311	8.36
43.365	2.084	400	8.34
57.285	1.606	511	8.35
62.933	1.475	440	8.34
		$\mathbf{a_{average}}$	**8.35**

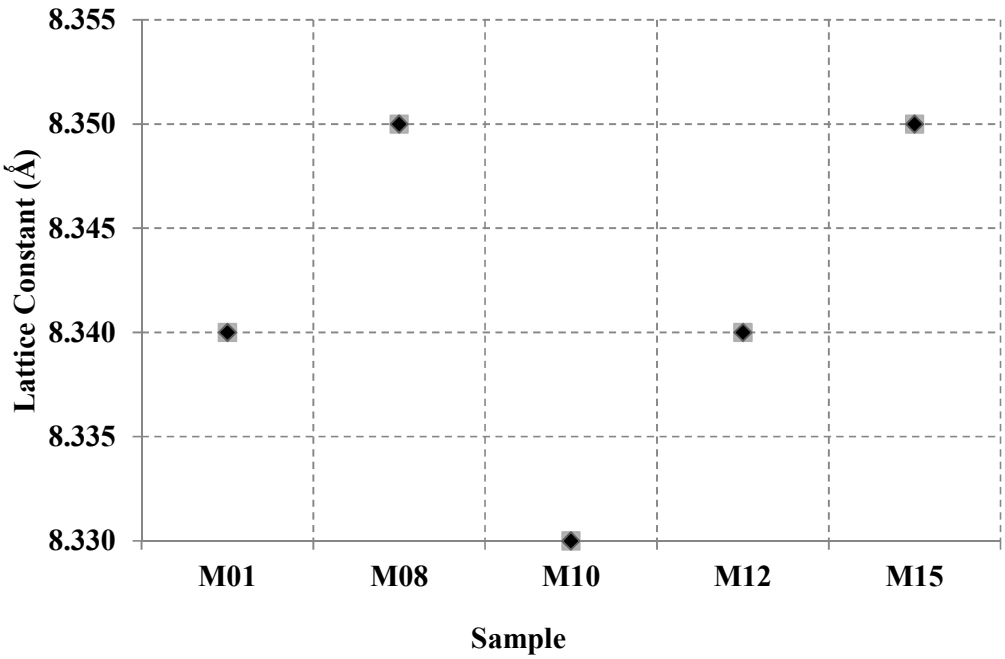

Figure 4.3:
Lattice Parameter for Samples

The broadening and lowering of intensity of the peaks in the XRD patterns in Fig. 4.2 indicate that the crystallite sizes of the samples are within nanometre scale for all samples. Assuming that the size distribution was the dominant cause for broadening, the average crystallite sizes of the samples were calculated (as shown in Table 4.9 and Fig. 4.4) from two major peaks, (311) and (440) using Scherrer's equation:

$$d_{XRD} = \frac{0.9\lambda(57.3)}{\beta \cos\theta} \qquad (4.3)$$

where, d_{XRD} = calculated crystallite size,

λ = wavelength, 1.54056 Å

β = full width at half maximum (FWHM) of the peaks

θ = diffraction angle

The factor 0.9 is an approximation of the angle 2θ at the maximum intensity, I_{max}. The value 57.3 is a constant used for the conversion between degree and radian.

A Profile Fitting software, *Profit*, was used to determine the value of FWHM and β. This program decomposes a powder diffraction pattern into its constituent Bragg reflections and yields defining parameters of each reflection. Lanthanum hexaboride (LaB_6) was used as the standard calibration material for instrumental broadening measurements.

The calculated crystallite sizes are 6.79 nm, 6.56 nm, 6.14 nm, 6.72 nm and 7.24 nm for samples M01, M08, M10, M12 and M15, respectively. From Figs. 4.3 and 5.4, the graphs exhibit a similar trend except for sample M08 (Fig. 4.3). The graphs indicate smaller crystallite size will have lattice parameter that is closer to maghemite's lattice parameter. This also shows that small crystallite size creates the stability for the maghemite nanoparticles. The results agree well with those reported in the literature (Ayyub et al., 1988; Schimanke and Martin, 2000).

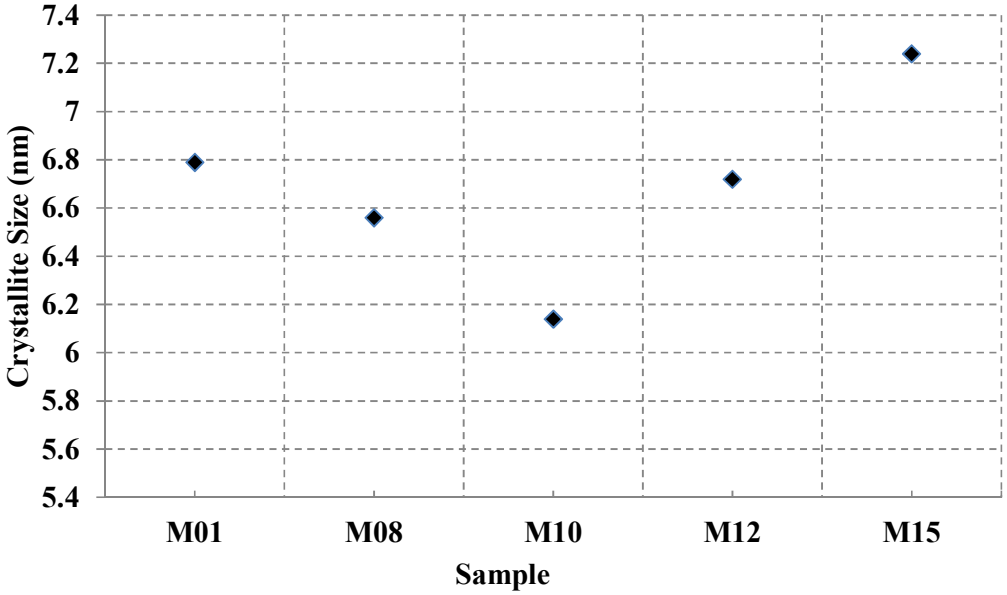

Figure 4.4:
Comparison of Crystallite Size for Samples

Table 4.9:
Crystallite Size for Samples

Sample	2θ (°)	θ (rad)	cos θ	$W_{b(sample)}$	$W_{s(standard)}$	Crystallite Size (nm)
M01	35.484	0.3097	0.95243	1.3181	0.0531	5.75
	62.8745	0.54875	0.85317	0.8817	0.1618	7.83
					Average	**6.79**
M08	35.5639	0.31039	0.95221	1.1458	0.0531	6.62
	62.8047	0.54815	0.85349	1.0559	0.1618	6.50
					Average	**6.56**
M10	35.5792	0.31053	0.95217	1.245	0.0531	6.09
	62.8507	0.54855	0.85328	1.1066	0.1618	6.20
					Average	**6.14**
M12	35.5862	0.31059	0.95215	1.1032	0.0531	6.87
	62.8445	0.54849	0.85331	1.0451	0.1618	6.57
					Average	**6.72**
M15	35.5687	0.31044	0.9522	1.1838	0.0531	6.40
	62.9332	0.54927	0.85291	0.8557	0.1618	8.07
					Average	**7.24**

4.1.4 Morphology and Physical Size

In this study, TEM analysis was performed, which provides information on the physical size and shape of primary particles and their state of agglomeration. The average size of the particles was calculated from about 100 particles.

TEM micrographs of the as-synthesized maghemite nanoparticles are shown in Figs. 4.5 - 4.9. The particles are nearly spherical and are within the nanometre size range. Moderate aggregation and agglomeration of particles are observed in the micrographs, which may be due to long-range magnetic dipole-dipole interactions and Van der Wall interaction between the particles. Moderate aggregation and agglomeration may also be caused by the drying process during TEM sample preparation. The occurrence of aggregation and agglomeration is a solid reason to proceed to Stage II and Stage III. The aggregation and agglomeration problem will be minimized by the encapsulation process in Stage II and III. This stabilizes the maghemite nanoparticles from any transformations.

The ESI analysis was carried out on sample M10, which proves that the particles as iron-based compounds, as shown in Fig. 4.10.

The size distribution histograms are shown in Figs. 4.11 - 4.15. Most of the particles are between 2 and 10nm. The calculated mean diameters are 5.97 nm, 6.02 nm, 4.98 nm, 5.35 nm and 5.98 nm for samples M01, M08, M10, M12 and M15, respectively. From measurement, M10 exhibits the smallest size compared with other samples. The trends of result agree well with the crystalline size calculated from XRD result shown previously.

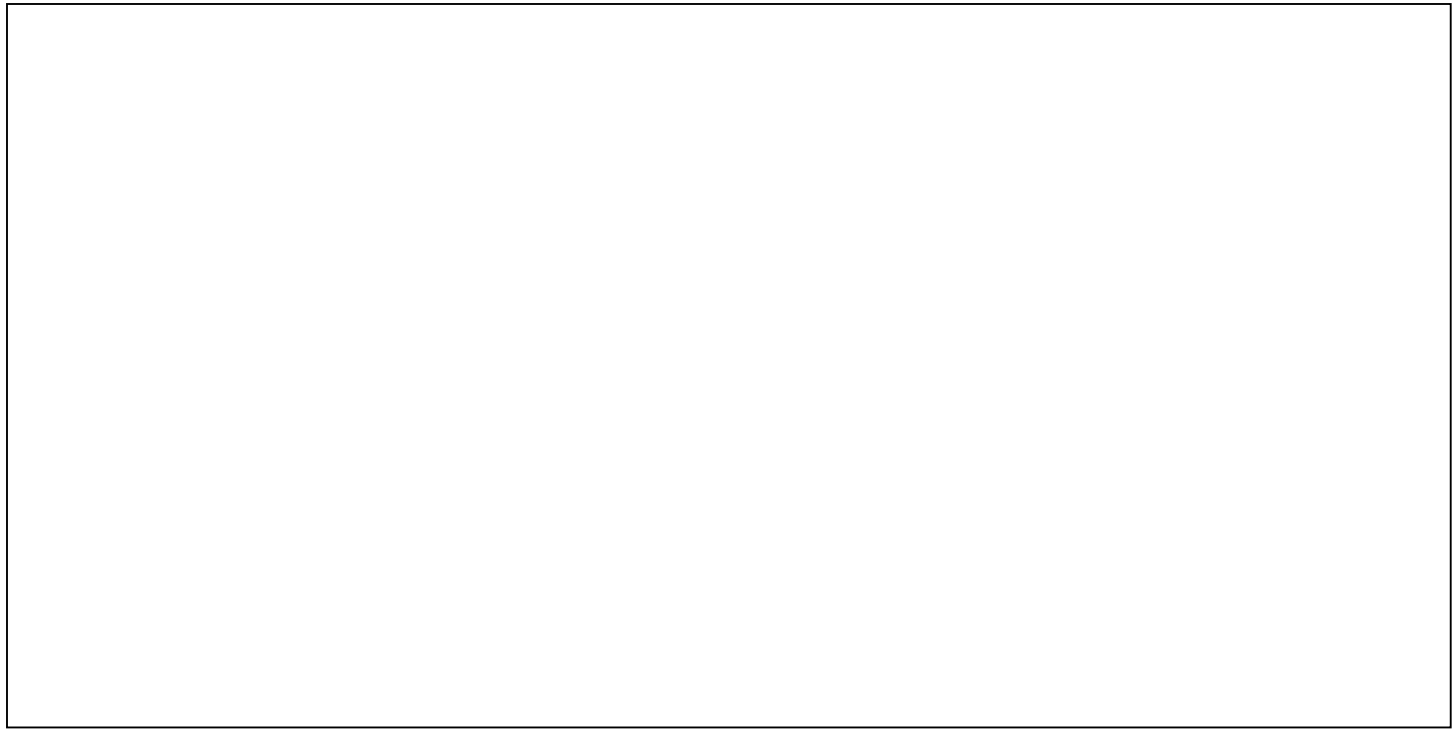

Figure 4.5:
TEM Images of Sample M01

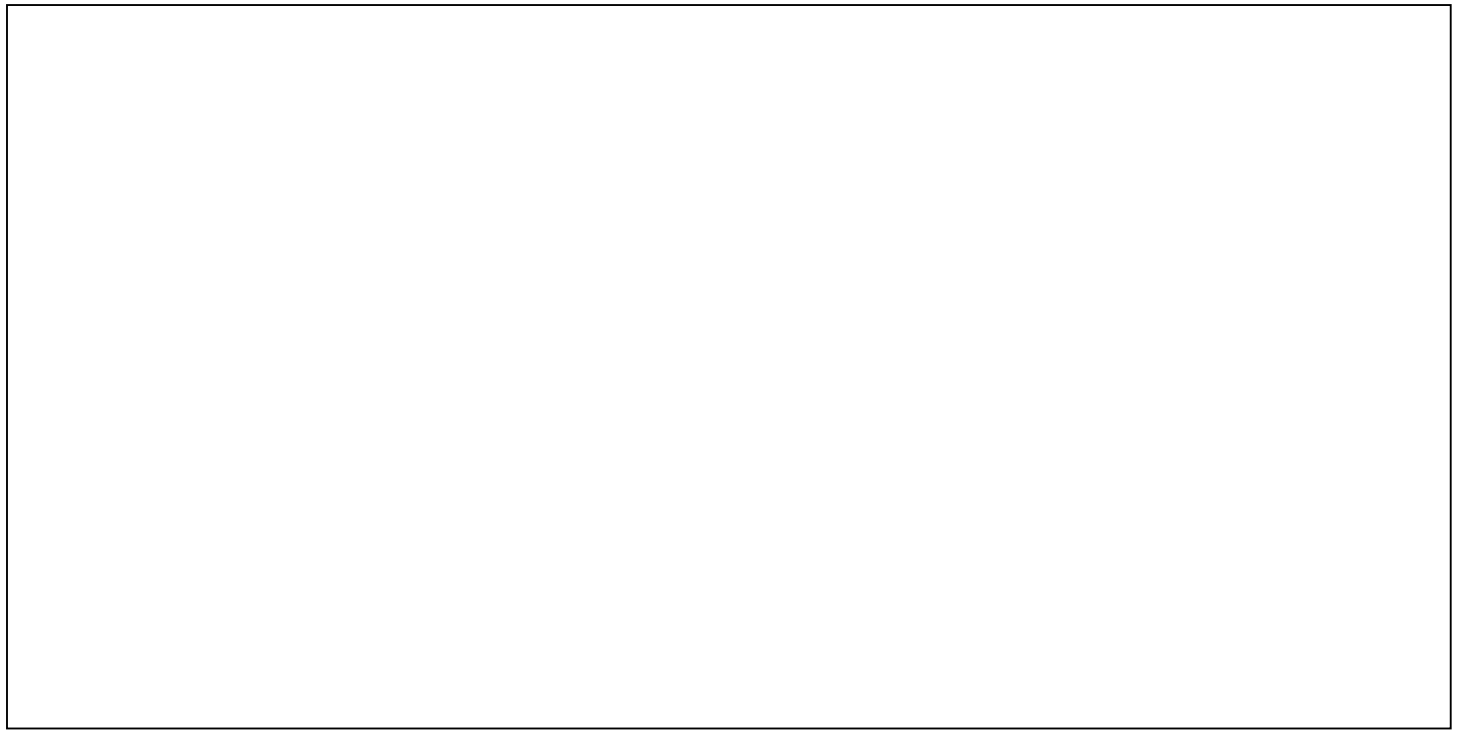

Figure 4.6:
TEM Images of Sample M08

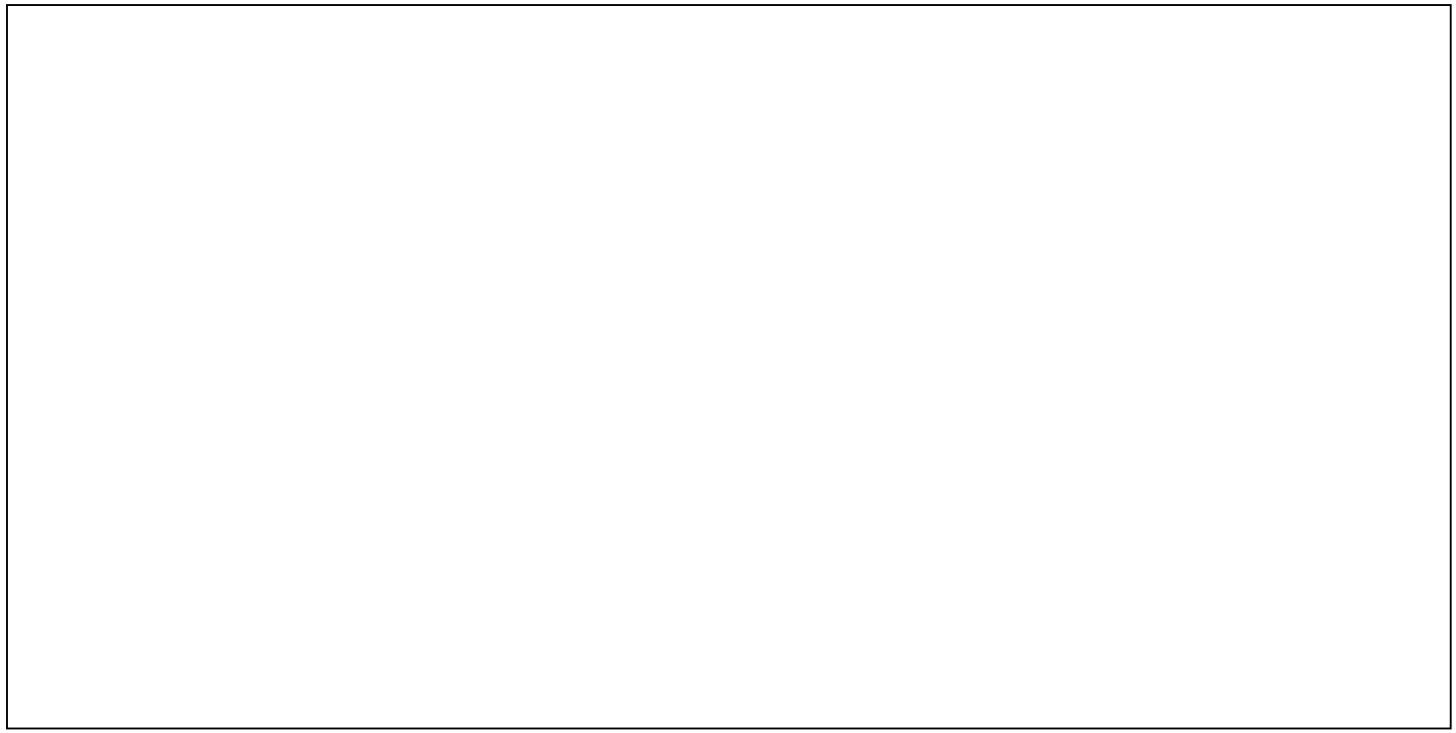

Figure 4.7:
TEM Images of Sample M10

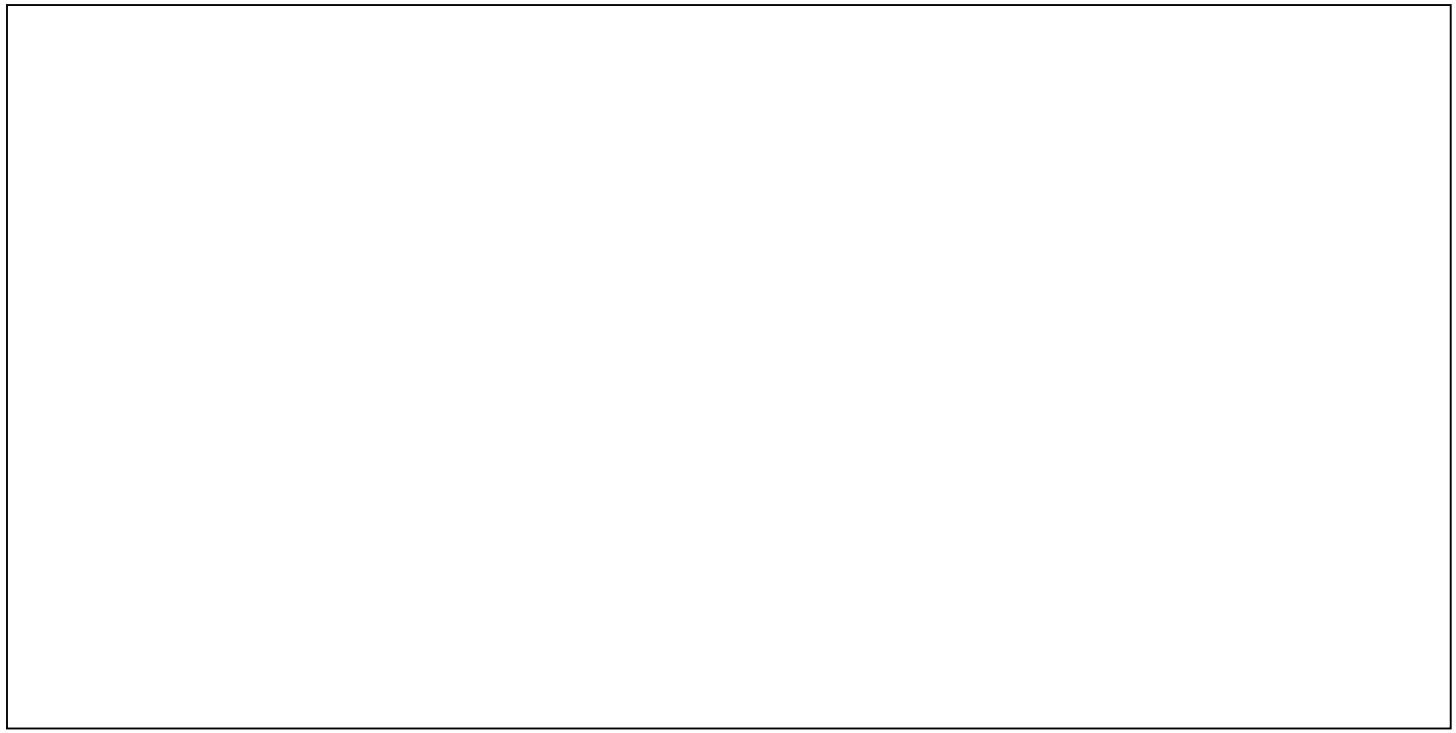

Figure 4.8:
TEM Images of Sample M12

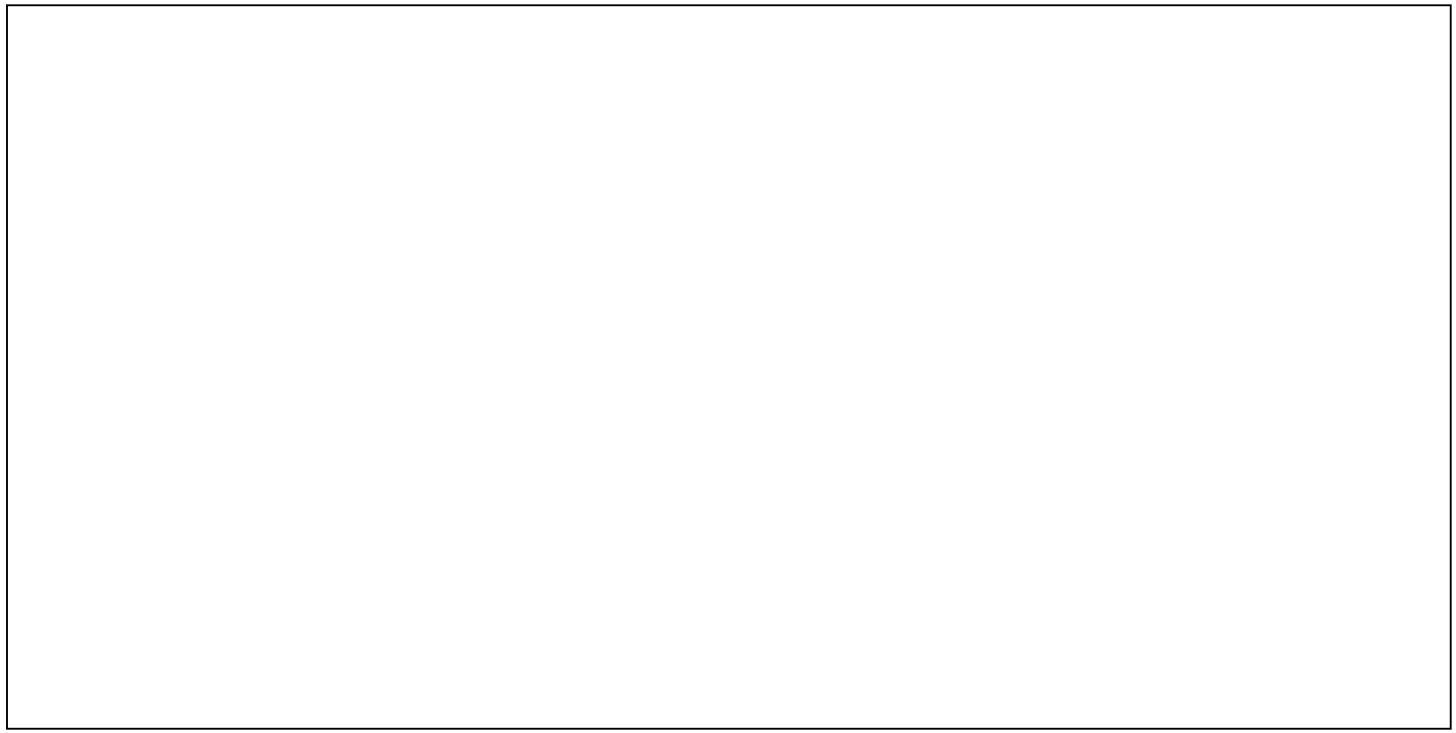

Figure 4.9:
TEM Images of Sample M15

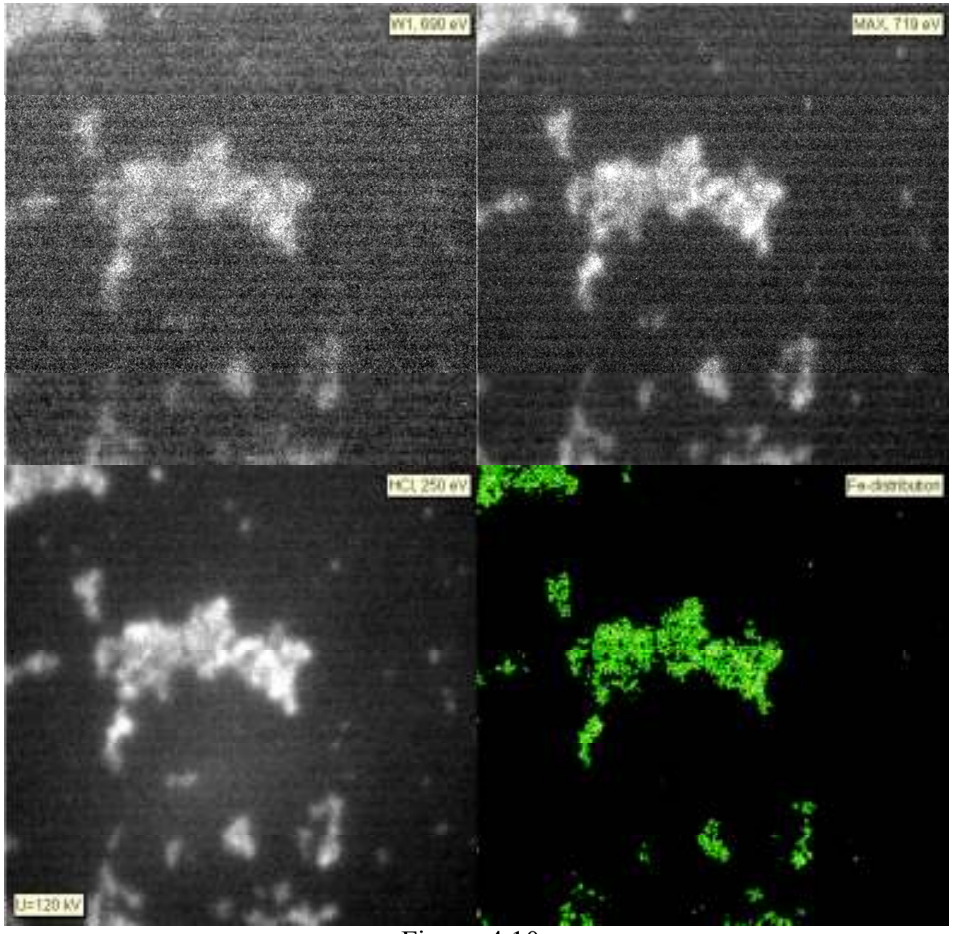

Figure 4.10:
ESI Images for Sample M10

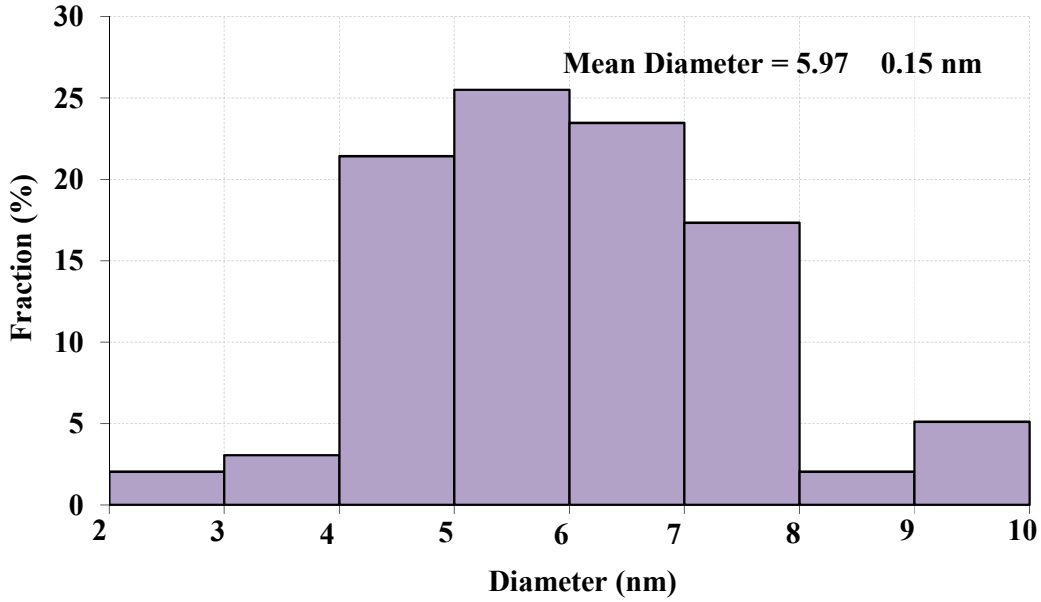

Figure 4.11:
TEM Physical Size Distribution Histogram for Sample M01

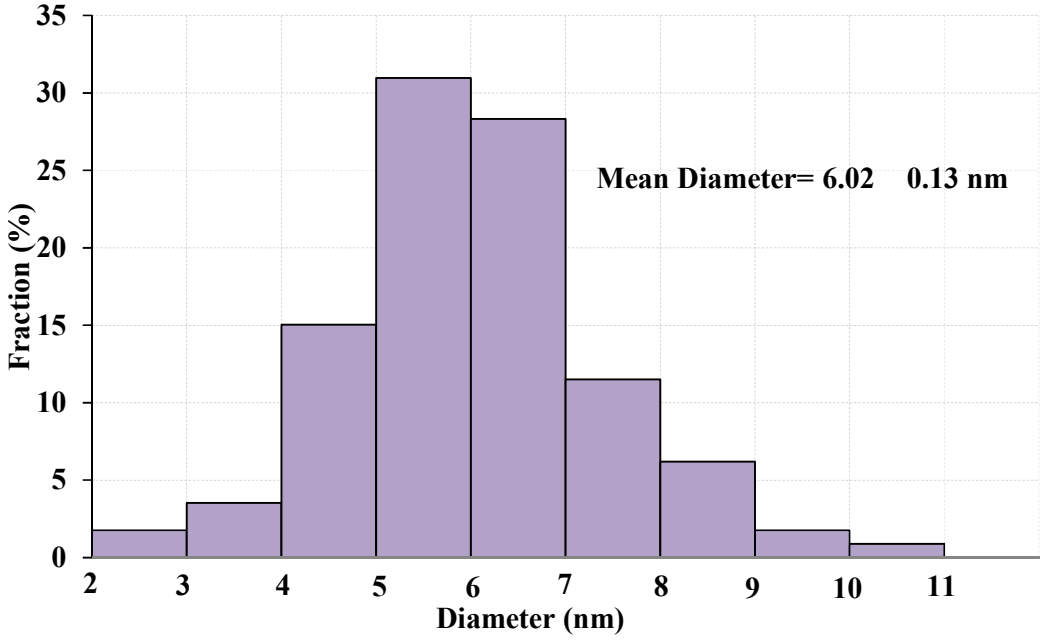

Figure 4.12:
TEM Physical Size Distribution Histogram for Sample M08

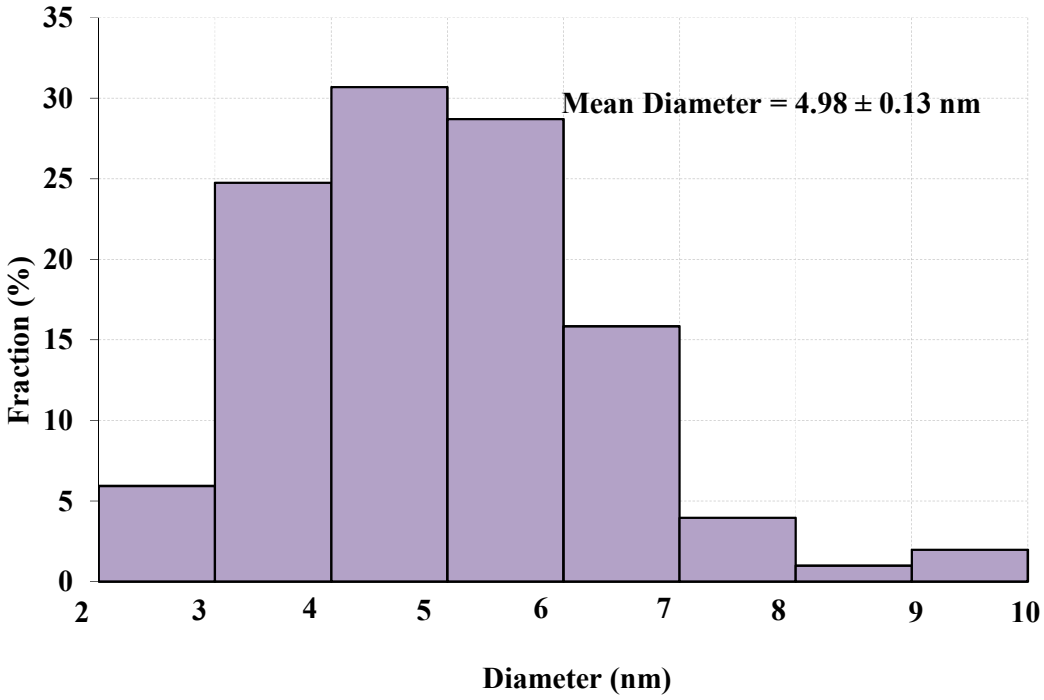

Figure 4.13:
TEM Physical Size Distribution Histogram for Sample M10

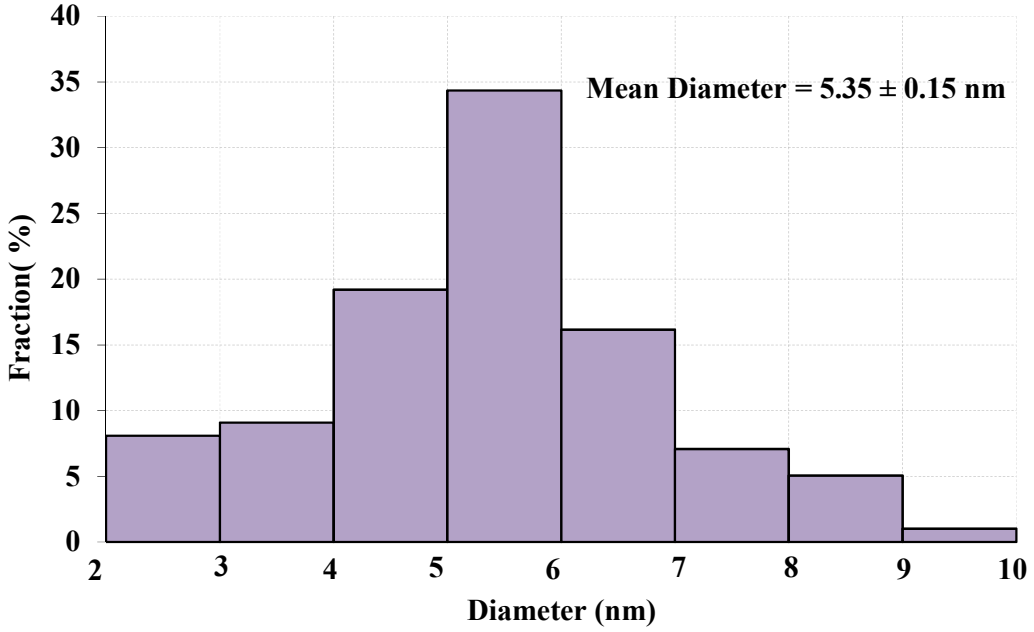

Figure 4.14:
TEM Physical Size Distribution Histogram for Sample M12

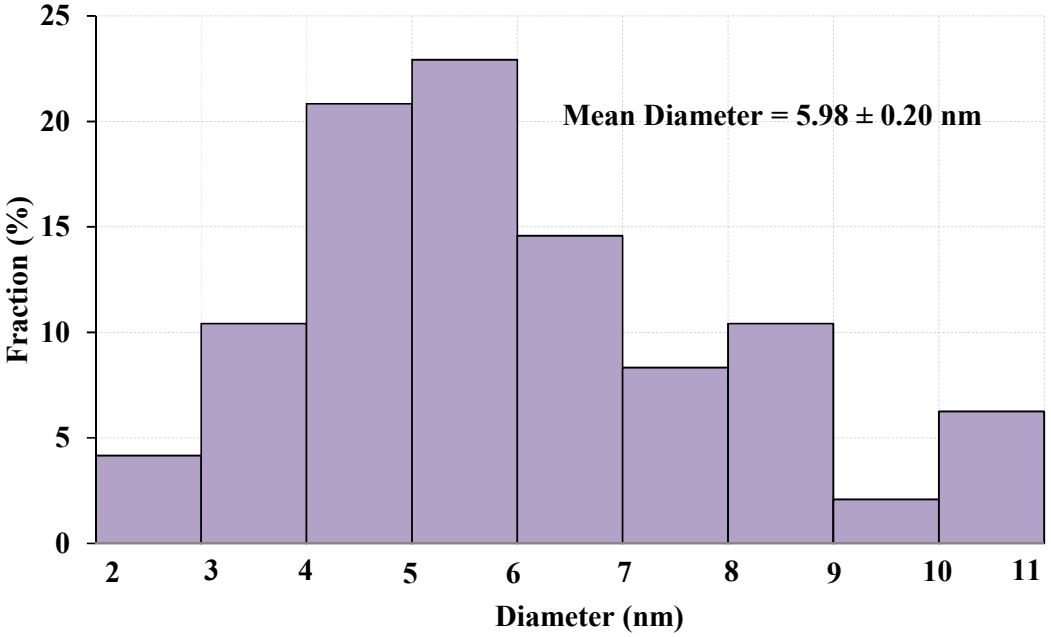

Figure 4.15:
TEM Physical Size Distribution Histogram for Sample M15

4.1.5 Surface Area Analysis

Due to the presence of agglomerates, it was sometimes difficult to determine the exact size of a single particle in the samples. Therefore, the size of the particles measured from the TEM images may be slightly inaccurate. In order to solve this problem, another measurement technique, i.e., gas adsorption desorption analysis was employed. In principle, this method is used to measure the specific surface area of materials. However, the size of particles can be determined using the relationship between surface area and particle size, assuming that the particles are spherical and non-porous.

$$d_{BET} = \frac{6}{\rho s} \qquad (4.4)$$

where ρ is the density of bulk maghemite and S is the specific surface area calculated by BET. Moreover, the mean pore size and the pore size distribution of the materials can

also be analyzed using this method. The results from the calculation are summarized in Table 4.10.

The typical gas adsorption-desorption isotherms of maghemite nanoparticles are shown in Fig. 4.16(a) - (e). The gas adsorption desorption isotherms exhibit these features: (i) the adsorption at relative pressure, $p/p_o \rightarrow 0$ is nearly zero, indicating the absence of micropores in the samples; (ii) a significant increase in volume adsorbed within a p/p_o range of 0.1 - 0.3, (iii) further increase in volume adsorbed and opening of hysteresis loops occurs at p/p_o of 0.3 – 0.99; (iv) a sharp increase in adsorbed amount at $p/p_o \rightarrow 1$. According to IUPAC classification, this type of isotherm is classified as type IV isotherm, i.e. a mesoporous material, with hysteresis loop within the range of p/p_o from 0.3 to 0.99. The existence of hysteresis loops in the isotherms is due to capillary condensation of N_2 gas occurring in the mesopores. Therefore, the isotherms are considered as a characteristic features of mesoporous materials.

Higher surface area means smaller particle size. The specific surface area increases when the concentration of $FeCl_2$ is increased from 0.1 to 1.0 M and decreases when the concentration is increased further to 1.5M. The calculated size is shown in Table 4.10. The results are in agreement with the XRD and TEM results.

Table 4.10:
Specific Surface Area (BET) and Calculated Particle Size of Samples

Sample	Specific Surface Area (m^2/g)	Calculated Particle Size (nm)
M01	87.1196	14.97
M08	96.9338	13.46
M10	154.3747	8.34
M12	73.3839	17.77
M15	71.3751	18.28

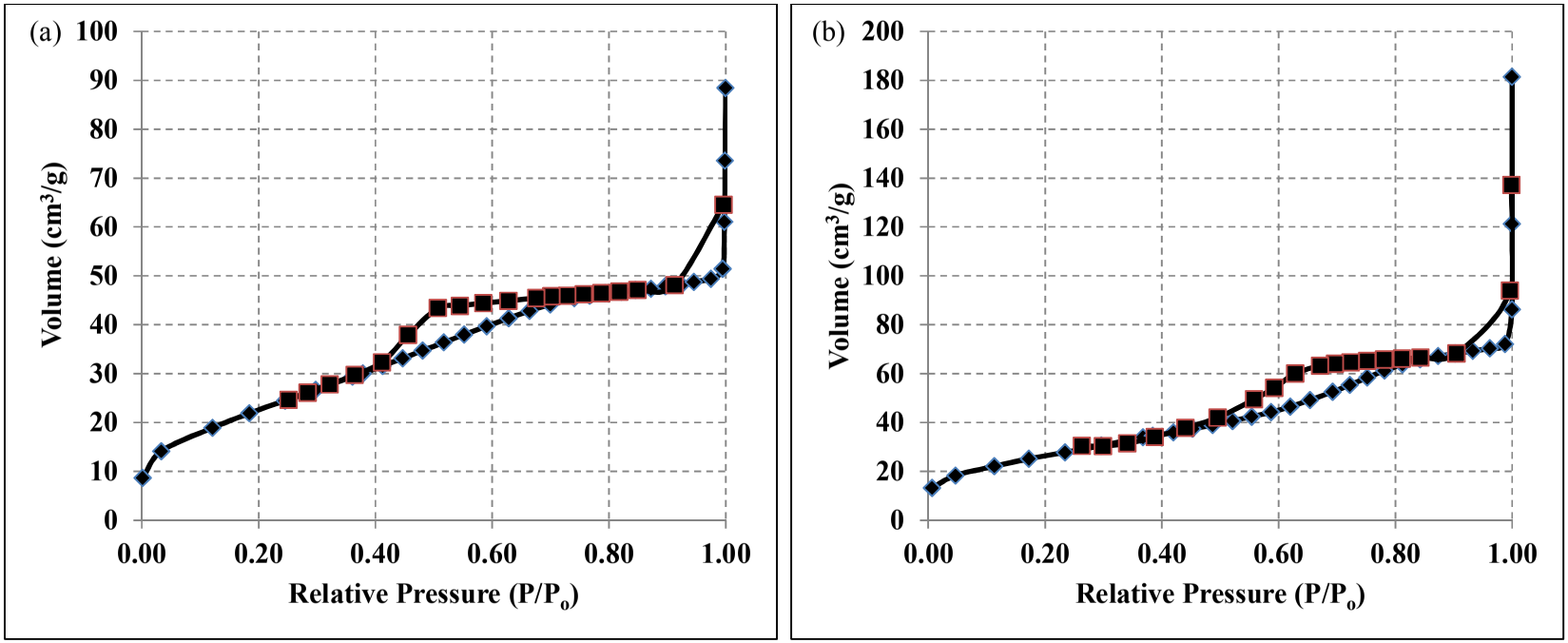

Figure 4.16:
N_2-gas Adsorption Desorption Isotherm for Sample (a) M01, (b) M08

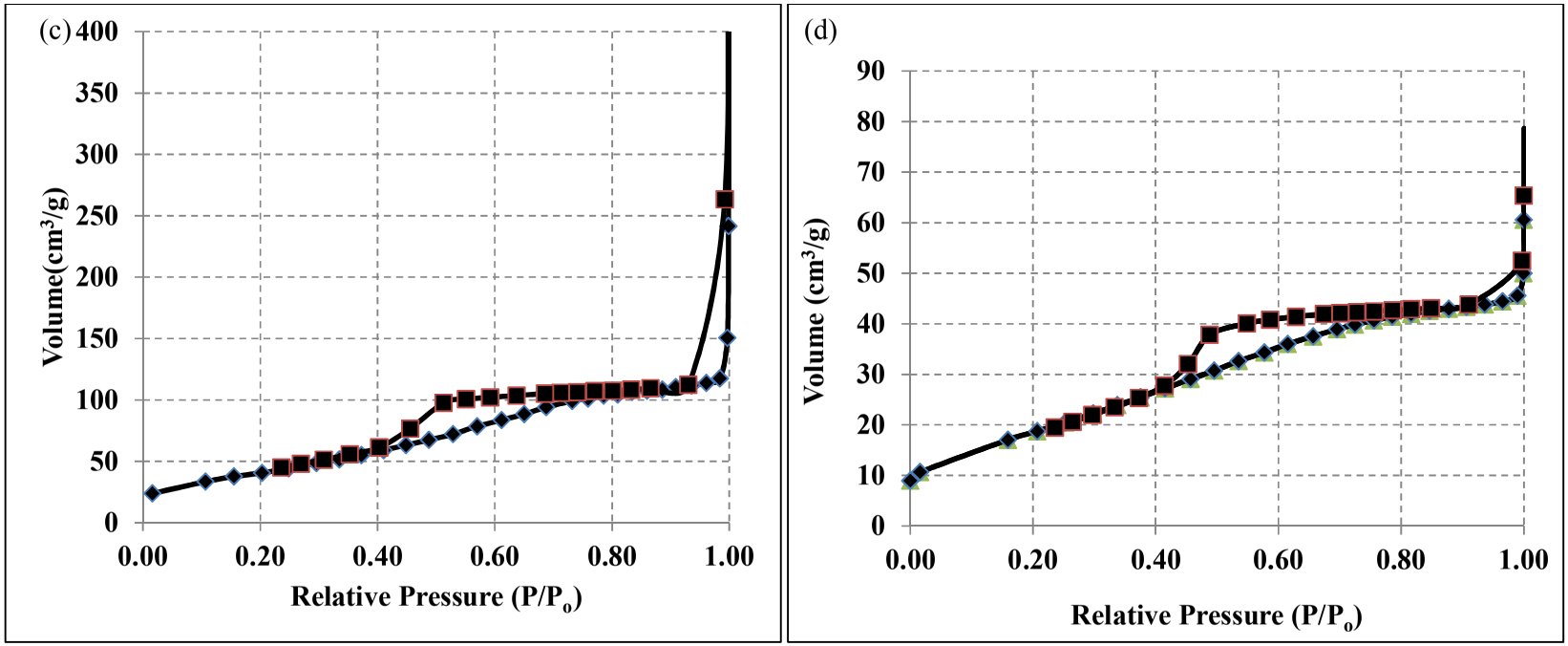

Figure 4.16 (continue):
(c) M10, (d) M12 and

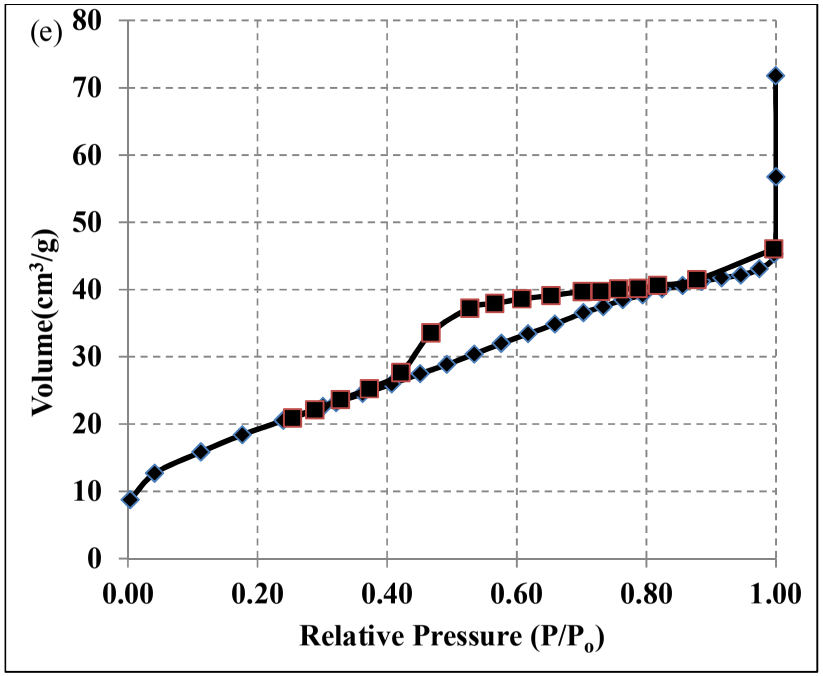

Figure 4.16 (continue):
(e) M15

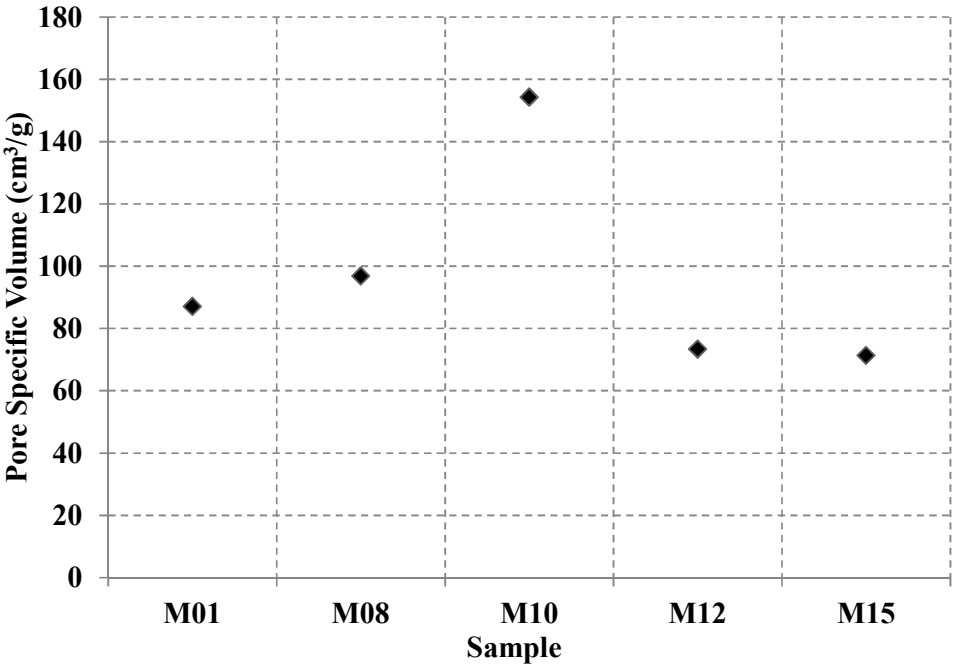

Figure 4.17:
Specific Surface Area (BET)

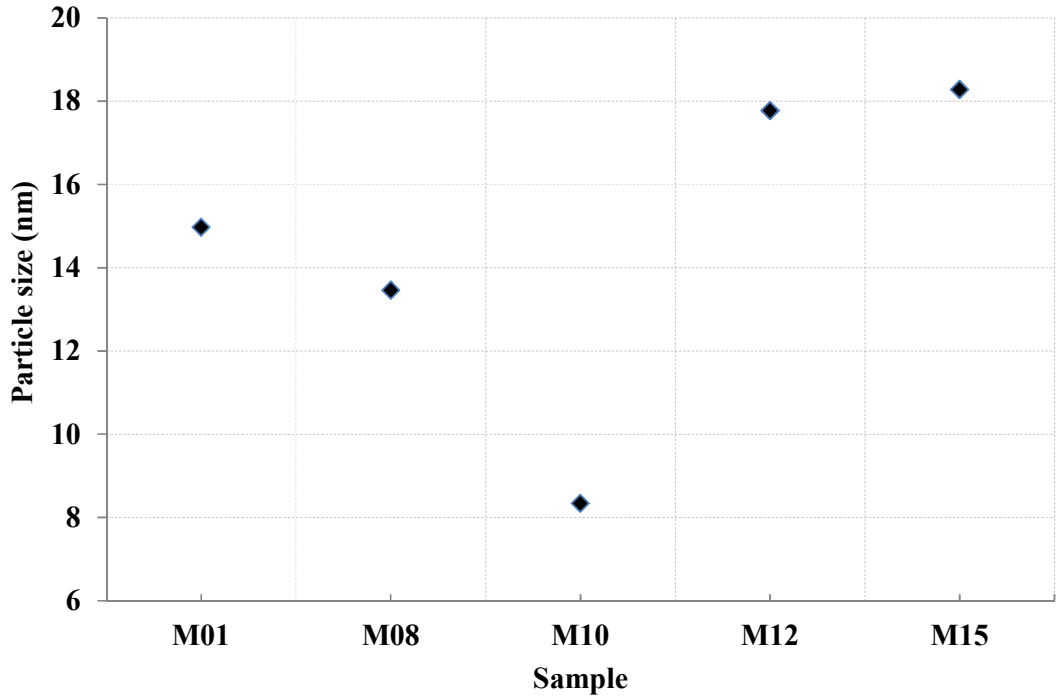

Figure 4.18:
BET Physical Size for Samples

4.1.6 Dynamic Light Scattering Analysis

The size distributions of maghemite nanoparticles were measured using dynamic light scattering (DLS) method in order to investigate the dependence of size on the concentration of $FeCl_2$.

The DLS histograms are shown in Fig. 4.19. The particle size increases gradually with increasing $FeCl_2$ concentration. The relationship between the particle size and $FeCl_2$ concentration in Massart's procedure is plotted in Fig. 4.20, and the observed trend is similar to the TEM, XRD and BET results.

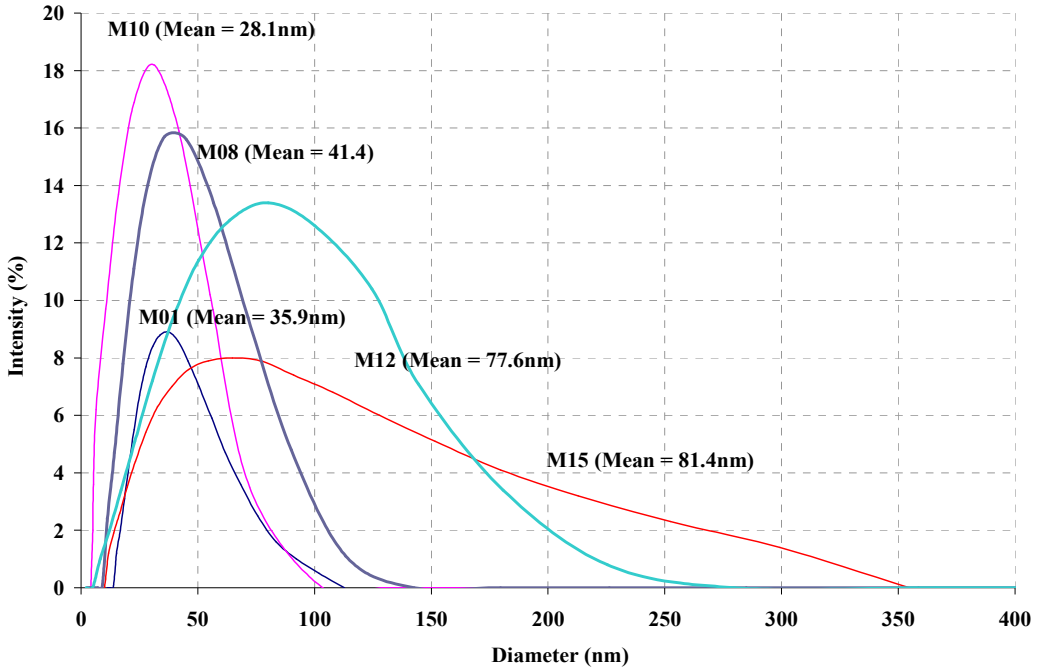

Figure 4.19:
DLS Size Distribution of Samples

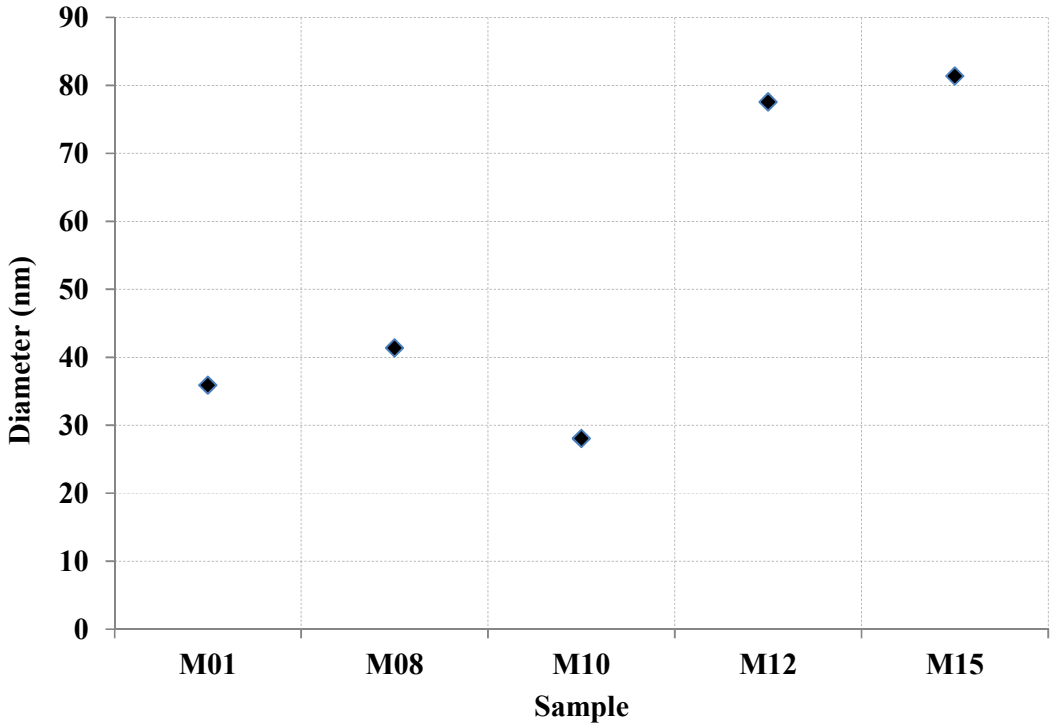

Figure 4.20:
DLS Mean Size of Samples

4.1.7 Magnetization Analysis

Fig. 4.21 shows a typical hysteresis curve of the samples at room temperature. The magnetic behaviour of the samples is under the influence of an applied magnetic field which alternates from a maximum of 10 kOe to a minimum of -10 kOe. The magnetic properties of all samples were extracted from the measurements and are summarized in Table 4.11.

The magnetization curves of the samples do not exhibit hysteresis loops as they pass through the origin at room temperature, which indicate that the remanence and coercivity are zero. This shows that the samples are superparamagnetic. Superparamagnetic phenomenon occurs only when the particle size is below a certain

critical dimension. In contrast, bulk magnetites or maghemites are ferrimagnetic. Typical values for hysteresis parameters of superparamagnetic materials are (Moskowitz, 1991):

$$M_r/M_s << 0.01 \qquad (4.5)$$

Magnetic properties such as coercivity, blocking temperature, saturation magnetization and remanent field are a function of the particle size, shape, and surface chemistry (Asti et al., 1994; Fang et al., 2000). When the particle is sufficiently small, ferrimagnetic materials lose their magnetization below the Neel temperature and become superparamagnetic. Hence, the material no longer exhibits any hysteresis. This is due to the fact that magnetic particles below a certain critical size cannot support more than one domain. The magnetization vector becomes unstable in this size range and begins to wander in a thermally activated manner analogous to the Brownian movement (Crangle, 1977).

The maximum magnetization for all samples at 10 kOe (M_{s10kOe}) are within 9 – 24 emu/g, which is lower than the reported value for bulk maghemite (74 emu/g). This phenomenon is usually observed in nanoparticle interacting systems. Such a reduction of M_{max} can be ascribed to surface effects arising from broken symmetry and reduced coordination of atoms lying at the surface of maghemite nanoparticles and also to a high degree of interparticle interactions (Kluchova et al., 2009). The particle size decreases and the surface/volume ratio increases such that surface effects dominate the magnetic properties (Gilbert et al., 2003), which may be due to the existence of noncollinear spins at the surface. The surface curvature of the nanoparticles is much larger for smaller particle size, which promotes disordered crystal orientations on the surface, which results in a significantly decreased M_s for smaller nanoparticles (Binh et al., 1998; Varanda et al, 2002; Coey, 1971; Santra et al., 2001).

When the particles are characterized by a non-uniform size distribution, the major contribution to the slope near a zero applied field (H = 0) comes from the largest particles. Thus, the calculated magnetic size is defined as "least upper bound magnetic size" (Yaacob et al., 1994). Assuming that the sample is maghemite, whereby the M_s value and density value for bulk material is 73 emu/g and 4.6 x 10^6 g/m^3 respectively, the least upper bound magnetic size of these particles is given by the following formula (Yee, 2003). The details regarding the magnetic properties and the calculated magnetic size are summarized in Table 4.11.

$$d_{mag} = \left(\frac{18kT\left(\frac{dM}{dH}\right)_{H=0}}{\pi\rho M_s^{\,2}} \right)^{1/3} \qquad (4.6)$$

where:

k = Boltzmann constant (1.38 x 10^{-16} erg/K)

T = Room temperature (298K),

$\frac{dM}{dH}_{H=0}$ = Slope of the magnetization curve near zero field, and

ρ = Density of maghemite (4.6 x 10^6g/m^3)

M_s = Saturation magnetization (73emu/g)

In view of the simplifying assumption of non-interacting, monodispersed, uniaxial magnetic particles, this result is comparable to the size of the particles as determined from XRD and TEM.

Table 4.11:
Magnetization Saturation and Calculated Magnetic Size

Sample	M_r/M_s	Saturation Magnetization (emu/g)	$dM/dH_{(H=0)}$	Magnetic Size (nm)
M01	0.0024	17.89	0.04445	7.53
M08	0.0018	13.29	0.02595	6.29
M10	0.0013	9.53	0.02205	5.92
M12	0.0008	12.65	0.0274	6.41
M15	0.0025	23.49	0.0541	8.04

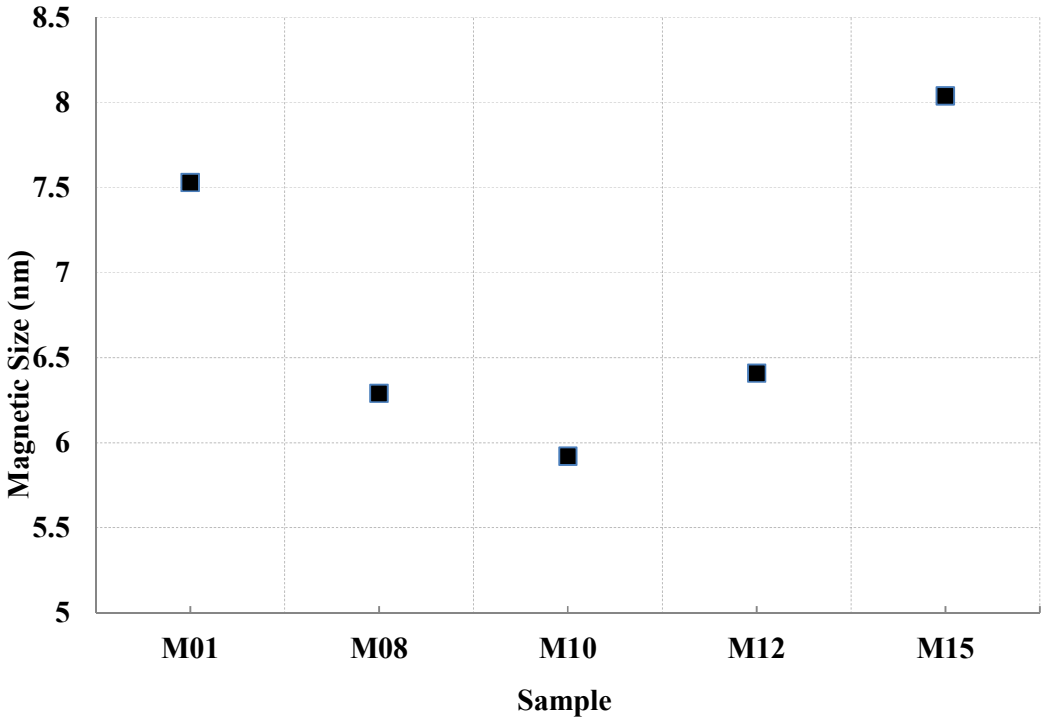

Figure 4.21:
Magnetic Size for Samples

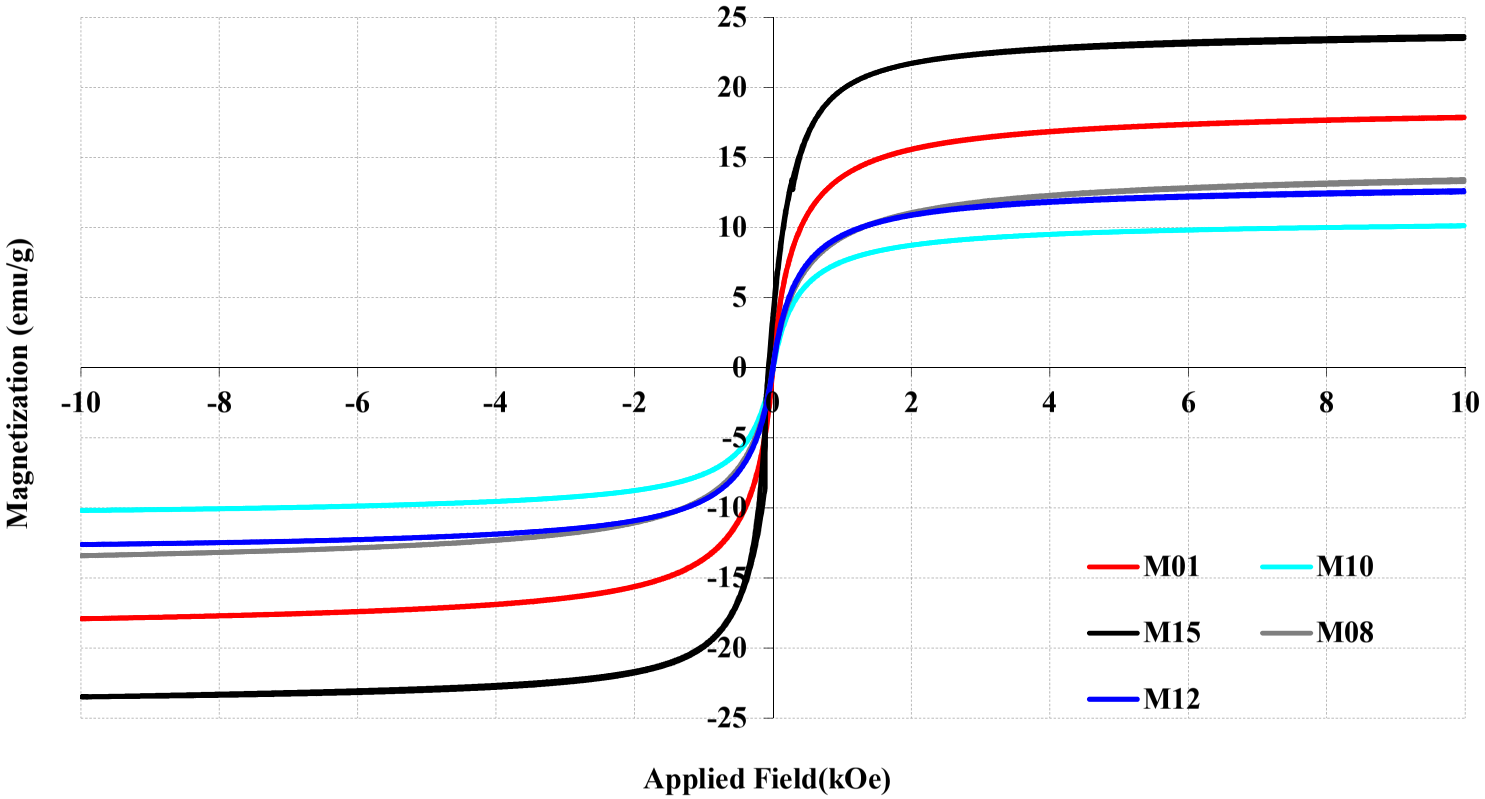

Figure 4.22:
Magnetization Curves for Samples

4.1.8 Summary for Stage I

Table 4.12:
Crystallite, Physical, and Magnetic Size of Samples

Sample	Crystallite Size (nm)	Physical Size (nm)	Hydrodynamic Size (nm)	Magnetic Size (nm)	Physical $Size_{(BET)}$ (nm)
M01	6.79	5.97	35.9	7.53	14.97
M08	6.56	6.02	41.4	6.29	13.46
M10	6.14	4.98	28.1	5.92	8.34
M12	6.72	5.98	77.6	6.41	17.77
M15	7.24	5.35	81.4	8.04	18.28

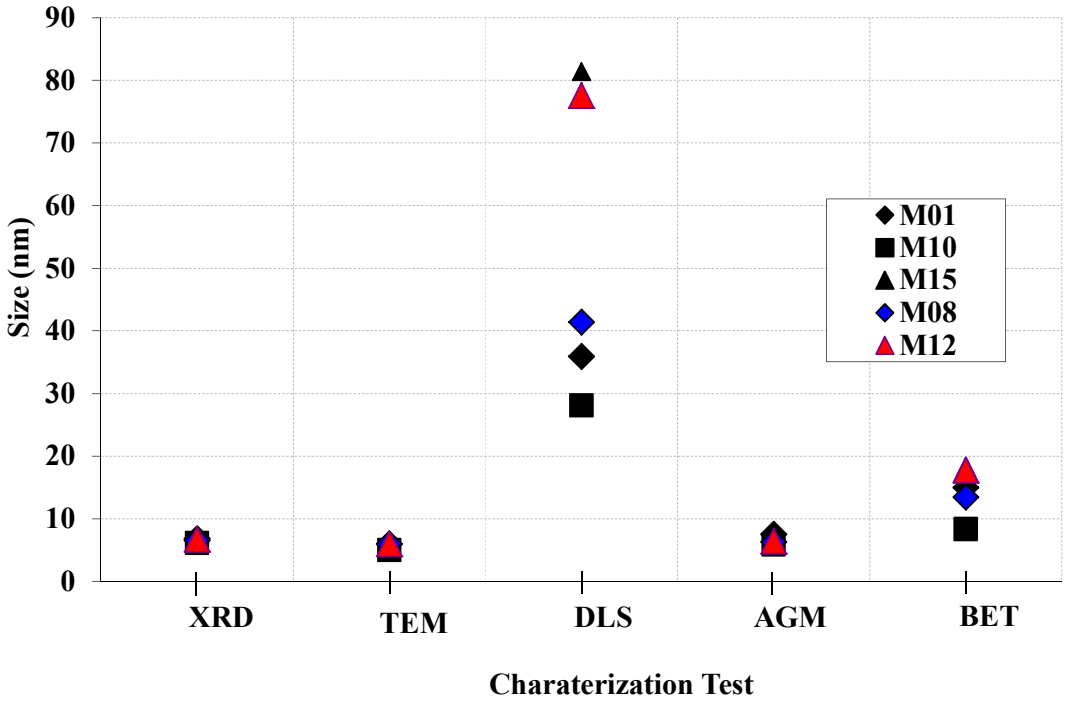

Figure 4.23:
Size Comparison Graph for Samples

From Fig. 4.23 and Table 4.12, it can be concluded that when the $FeCl_2$ concentration increases from 0.1 to 1.0M, the size of as-synthesized maghemite nanoparticles decreases. However, when the $FeCl_2$ concentration is increased further, the

size of as-synthesized maghemite nanoparticles increases. This indicates that a very low or a very high $FeCl_2$ concentration leads to the formation of larger particles. According to classical nucleation and growth theory, concentration is one of the predominant factors which determine the growth rate in diffusion controlled classical coprecipitation reactions due to the growth of the nucleus via a long-distance mass transfer. This means the size of the product would be larger with higher concentrations. The results are in agreement with the latter results of this study (from 1.0M – 1.5M). However, the size of the as-synthesized maghemite nanoparticles decreases when the $FeCl_2$ concentration increased from 0.1M to 1.0M, which may be due to the concentration of the precursor was too low to form stable nuclei for sample M01 and M08. The nuclei formed was too small, therefore surface area involved is too large and leads to high free energy. The nucleis tend to attract neighbour particles to form more stable particles. This is another new finding for this study, which has never been reported elsewhere.

XRD and TEM particle sizes are close, but very different from the BET and DLS sizes. This is due to XRD and TEM are mainly calculate the single crystallite size while DLS and measuring the hydrodynamic size. Where for BET, it was a dry powder and it measured the agglomerate and agglomeration particles.

The smallest size is chosen due to its large surface area to volume percentage, higher transition temperature and enhanced thermal stability compared with that of the corresponding normal polycrystal. It has also been reported that particles < 10nm continue to remain in γ-phase up to 1000^{o}C (Solinas et al., 2001). Smaller size maghemite nanoparticles will be more efficient in technological and industrial applications. However, maghemite nanoparticles require further treatment to minimize agglomeration and aggregation. The nanoparticles have hydrophobic surfaces with a

large surface area to volume ratio. Due to this interaction, the particles form aggregates and grow to minimize the overall surface free energy (Held et al., 2001). This increases the size of the particles and forms a stronger magnetic dipole-dipole attraction between the particles, which will result in ferromagnetism.

Therefore, pure magnetic particles themselves may not be very useful in practical applications due to the following limitations: (i) they tend to form large aggregates, (ii) their original structures may vary if they are sufficiently unstable resulting in the alteration of magnetic properties and (iii) they can undergo rapid biodegradation when they are exposed directly to biological systems. Therefore, a suitable coating is necessary to prevent such constraints. In the following study, the size of the maghemite nanoparticles is controlled by encapsulating the particles within silica xerogel matrix (stage II) and silica particulate matrix (stage III) by sol-gel technique.

4.2 PREPARATION OF MAGHEMITE-SILICA XEROGEL NANOCOMPOSITES

In this research, maghemite-silica xerogel nanocomposites were produced by sol-gel process and the effects of varying the amount of as-synthesized maghemite nanoparticles on the physical and magnetic properties of the nanocomposites were investigated. The primary aim of this stage was to create a physical barrier around the maghemite nanoparticles and hence, reduce the agglomeration problem. This stage was also aimed of observing the influence of variation of Fe_2O_3/SiO_2 ratios on the average size of maghemite particles and/or their distribution.

4.2.1 Formation of Silica Xerogel

A control sample of pure silica xerogel was produced by sol-gel process and labelled as S1. The steps for the formation of silica xerogel can be described briefly as follows:

a) TEOS solution was added to a mixture of tetrapropylammomium hydroxide solution and deionized water in a weight ratio of 5:7:3, respectively.

b) Polymerization occurred in three stages throughout the stirring time (Iler, 1979):

   1) Polymerization of monomers to form particles.
   2) Growth of particles.
   3) Linking of particles into chains, followed by networks which extend throughout the liquid medium, thickening into a gel.

c) Occurence of hydrolysis and condensation to create 3 - dimensional networks, as shown below (Brinker and Scherer, 1990):

   - Hydrolysis

$$\equiv\text{S-OR} + \text{H}_2\text{O} \rightleftharpoons \equiv\text{Si-OH} + \text{ROH} \qquad (4.8)$$

   - Water condensation

$$\equiv\text{Si-OH} + \text{Si-OH}\equiv \rightleftharpoons \equiv\text{Si-O-Si}\equiv + \text{H}_2\text{O} \quad (4.9)$$

   - Alcohol condensation

$$\equiv\text{Si-OR} + \text{HO-Si}\equiv \rightleftharpoons \equiv\text{Si-O-Si}\equiv + \text{ROH} \quad (4.10)$$

where R is an alkyl group $(C_2H_5)_4$.

d) The whole solution was aged overnight with vigorous stirring. The viscosity of the sol-gel solutions increased as the reaction proceeded.

e) The system was then heated for 3 days at 140^{o}C. Subsequent elimination of water from two Si-OH groups eventually formed an extended silica gel matrix (known as xerogel when dry). Fig. 4.24 shows the physical appearance of silica xerogel.

Figure 4.24:
Silica Xerogel When Dry

4.2.1.1 Thermal Properties

Figure 4.25 shows the TGA curve of sample S1. A weight loss of about 28.5% is observed upon heating over the range from room temperature to 700^{o}C. Two significant weight losses are observed for sample S1. The first weight loss occurs at around 100^{o}C, which is mainly due to dehydration or evaporation process. The second weight loss occurs at around 230^{o}C, which is caused by dehydration and evaporation of sol-gel solvent trapped within the silica xerogel networks or pores.

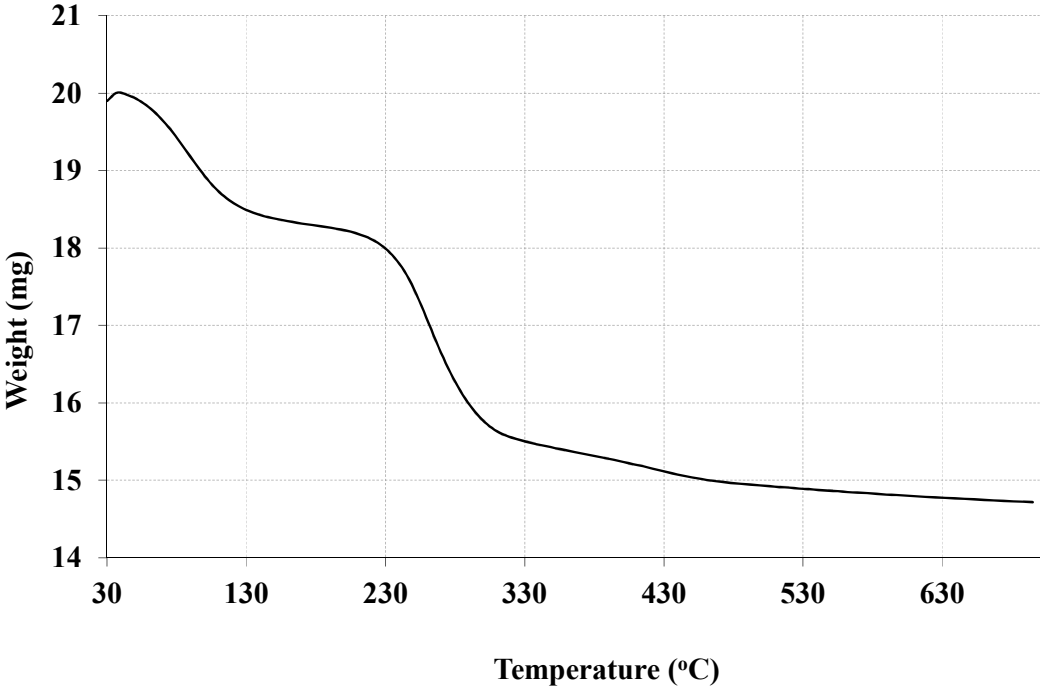

Figure 4.25:
TGA Curve for S1

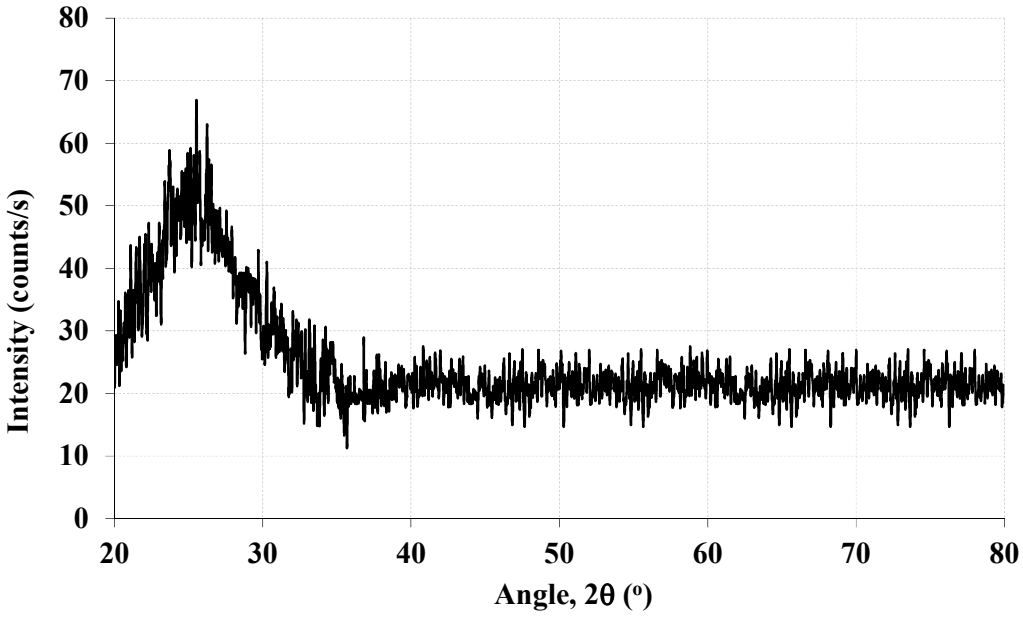

Figure 4.26:
XRD Pattern for S1

4.2.1.2 Phase and Crystal Structure

Figure 4.26 shows the XRD diffraction pattern of sample S1. Only one broad diffraction shoulder is observed at 2θ angles between 20^o and 35^o, which corresponds to the pattern for amorphous silica gel (Rainho et al., 2001; Barrado et al., 2005).

4.2.1.3 Surface Area Analysis

The surface area of S1 was studied by the N_2 absorption desorption method. Fig. 4.27(a) shows a typical mesoporous graph for sample S1. The unique features are (i) the adsorption at $P/P_o \rightarrow 0$ shows a small increase, which indicates a small amount of micropores; (ii) a relatively moderate increase in the adsorbed amount of N_2 within the P/P_o range of 0.1-0.9; (iii) a sharp increase in adsorbed N_2 within the P/P_o range of 0.9-1.0; (iv) the hysteresis loop is rather big and horizontally oriented; (v) the isotherms do not exhibit plateau at $P/P_o \rightarrow 1.0$, but they asymptotically approach the *y*-axis. These features correspond relatively well to Type IV isotherm.

The specific surface area calculated by the BET method is 155.09 m^2/g. The Barrett Joyner Halenda pore size distribution calculated from N_2 absorption analysis gives an average size of 15 nm. This value is in good agreement with the mean pore diameter determined by TEM and FESEM, which will be shown later.

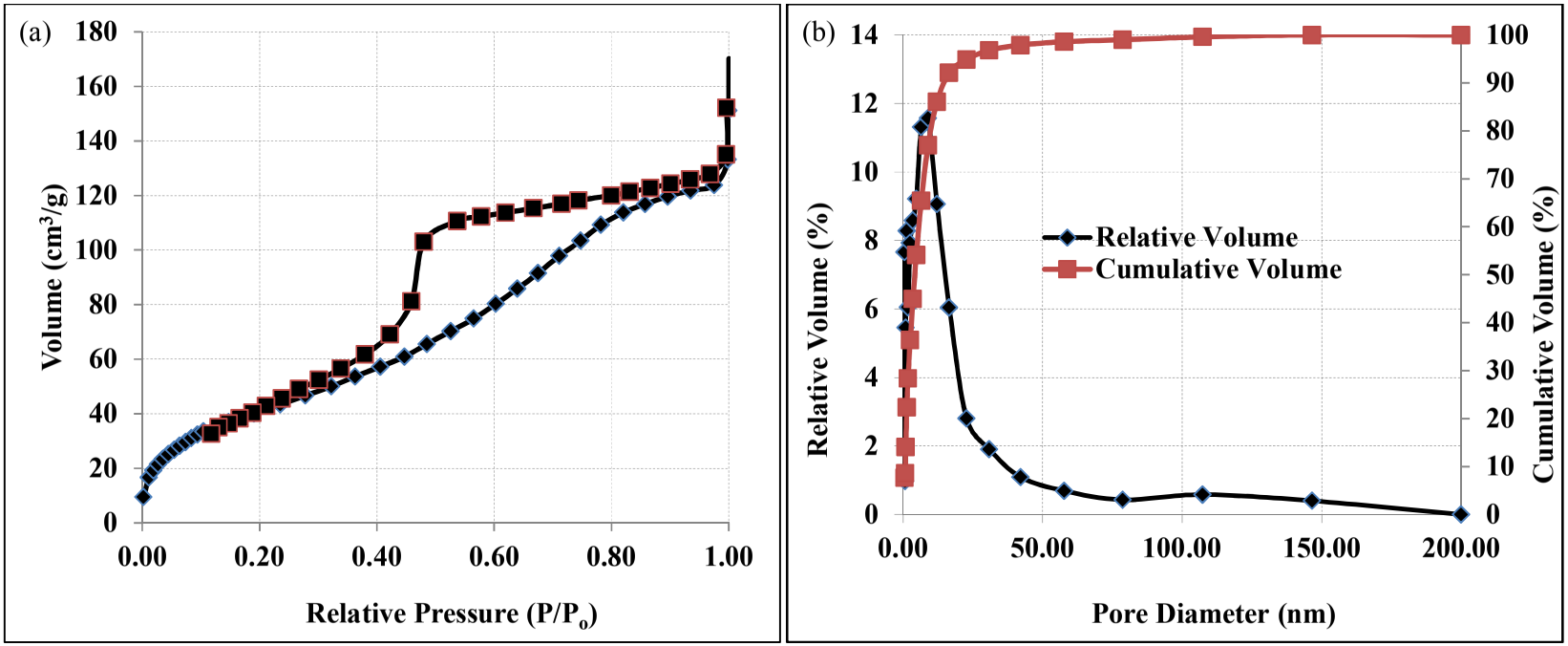

Figure 4.27:
(a) N_2-gas Adsorption Desorption Isotherm and (b) Pore Size Distribution of S1

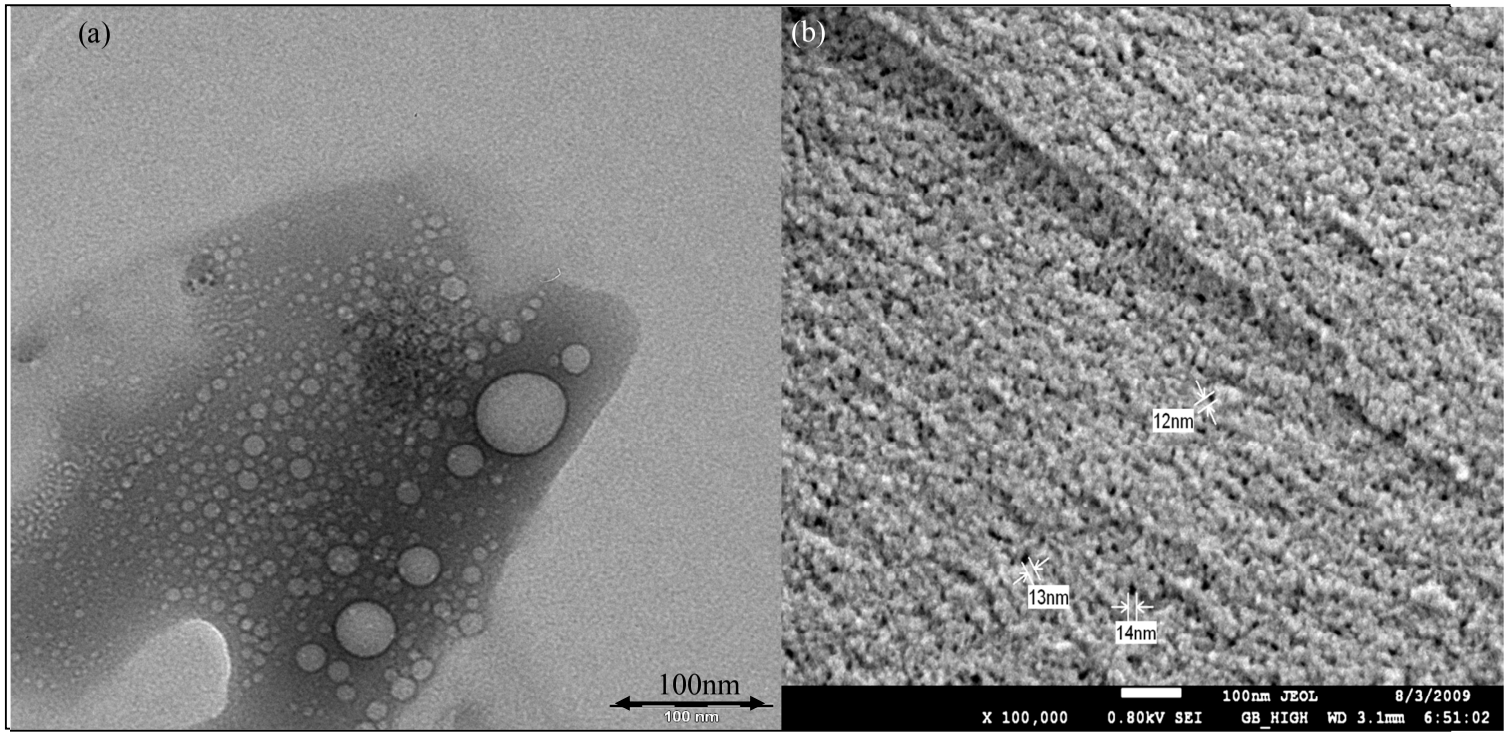

Figure 4.28:
(a) TEM Micrograph and (b) FESEM Micrograph of S1

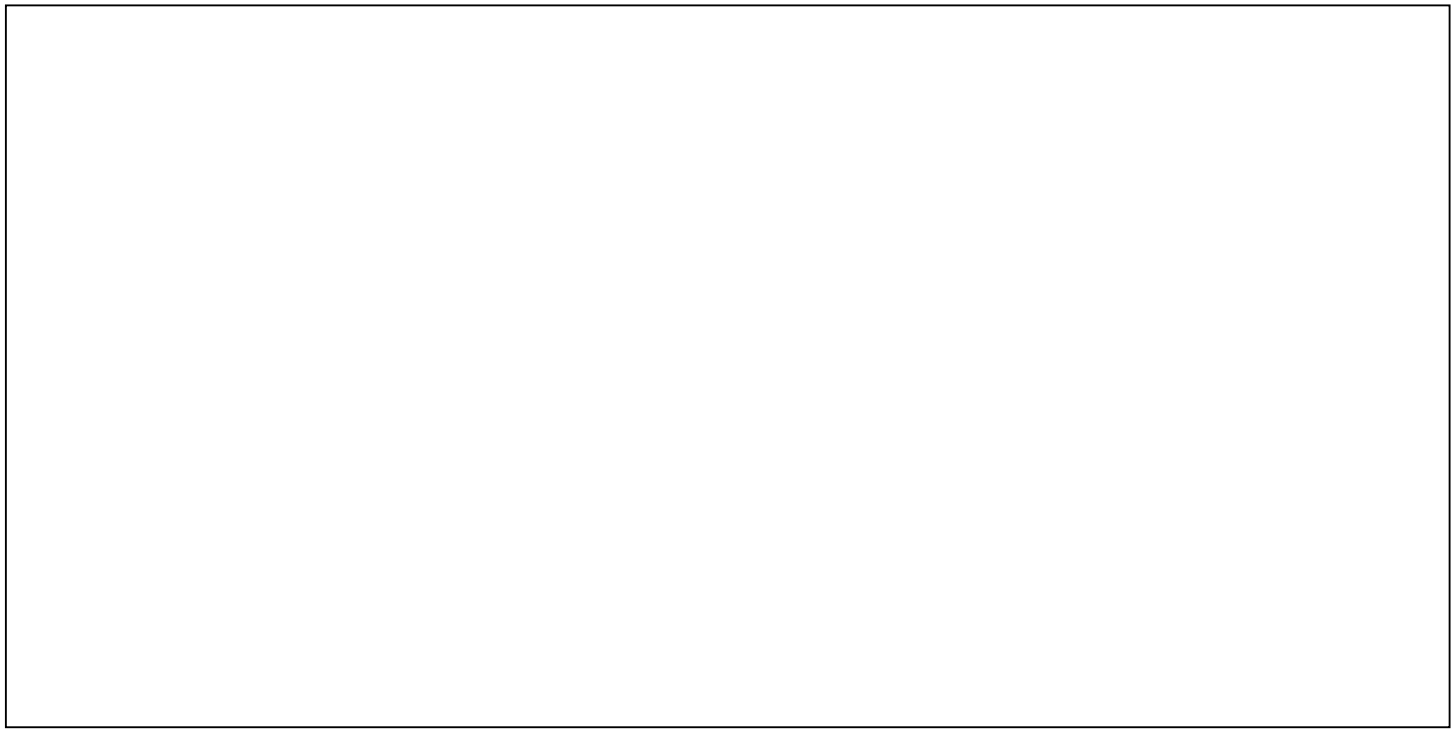

Figure 4.29:
FESEM Micrograph and (b) EDX of S1

4.2.1.4 Morphology and Physical Size

TEM and FESEM analyses were performed, which provide information on the physical and structure of the silica xerogel formed. Silica amorphous phase is a very electro-sensitive material. The image may alter or disappear in some areas after a few seconds of exposure to the beam. Hence, it is particularly difficult to capture good TEM and FESEM images.

The TEM micrograph in Fig. 4.28(a) shows the structure of the silica xerogel matrix, which reveals that the matrix is in gel form with many pores. The average pore size of the gel was measured from around 100 pores and was estimated to be within 14.2 nm size range, as shown in Fig. 4.30.

The FESEM micrographs in Figs. 4.28(b) and 4.29(a) exhibit the surface morphologies for sample S1. The gel is in a network texture with pores and the average physical pore size is approximately 15 nm. From Fig. 4.29(b), EDX analysis reveals a major presence of Si and O. This further confirms the presence of only Si and O in the silica xerogel and that no other impurities and surfactants remain in the sample. The carbon peak is mainly due to the contamination of the sample during FESEM sample preparation.

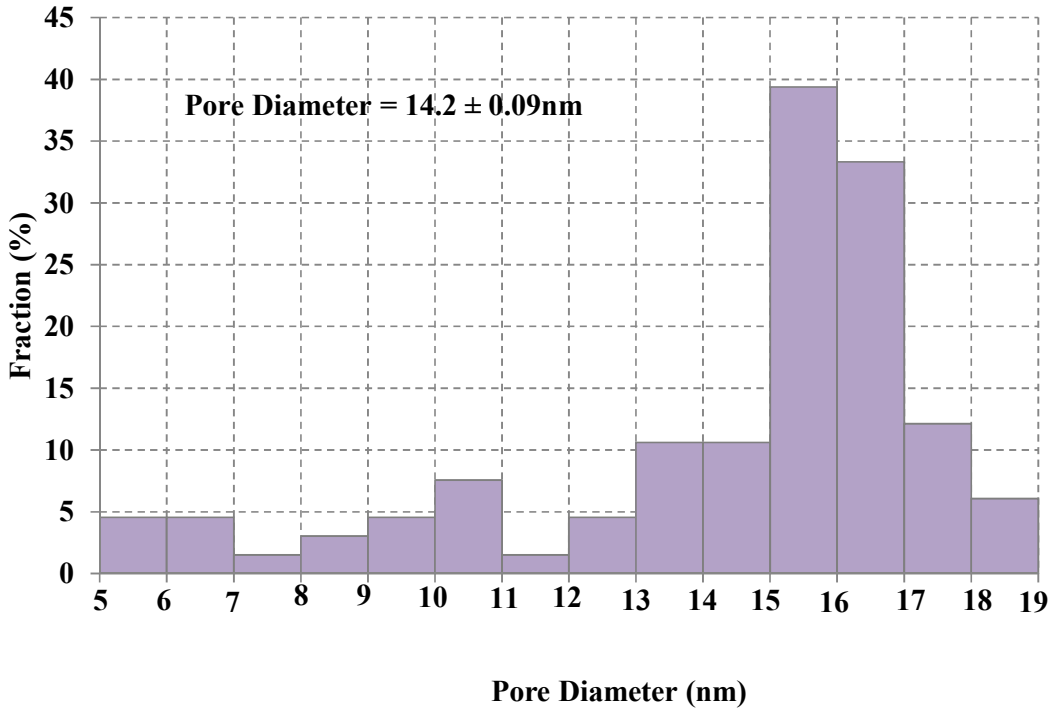

Figure 4.30:
Pore Size Distribution Histogram of S1

4.2.1.5 Magnetization Analysis

Fig. 4.31 shows a typical hysteresis curve for sample S1 at room temperature. The maximum magnetization for sample S1 at 10 kOe (M_{s10kOe}) is 0.05 emu/g, which is very low compared with the maghemite nanoparticles. Hence, silica gel is treated as a non-magnetic matrix in this study.

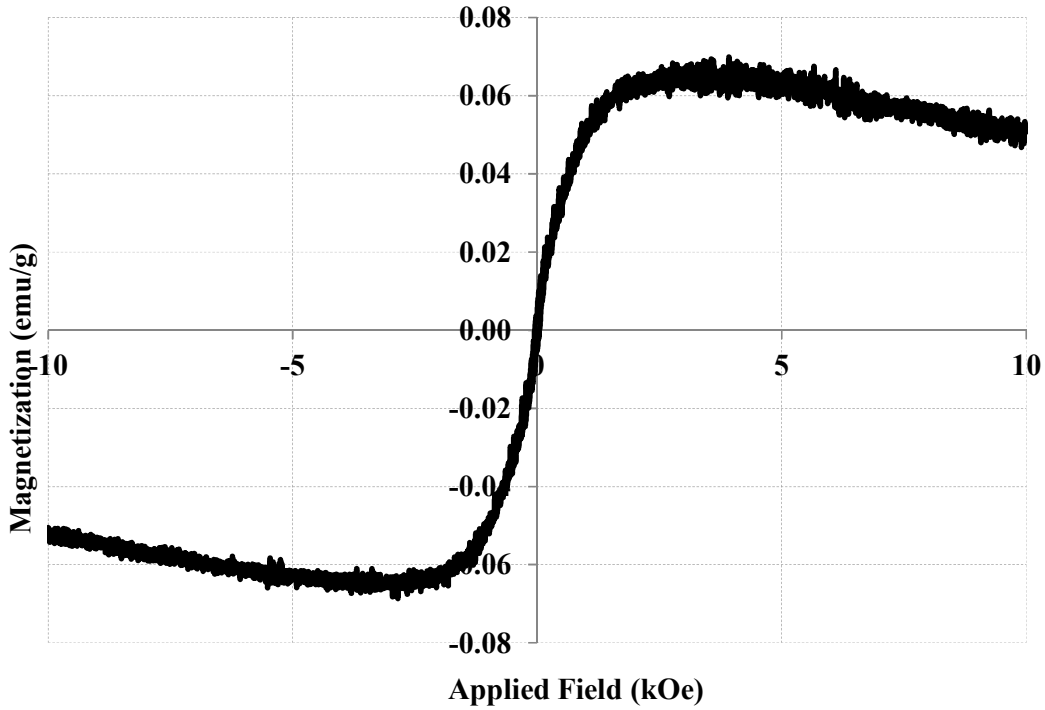

Figure 4.31:
Magnetization Curve of S1

4.2.2 Formation of Maghemite-Silica Xerogel Nanocomposites

Five samples were prepared in this study by sol-gel method. The steps for the formation of maghemite-silica xerogel nanocomposites are described in Section 3.1.1.2. The compositions of the samples are shown below:

Table 4.13:
Composition of Samples

Sample	Maghemite Nanoparticles (g)	TEOS (g)	H_2O (g)	TPA(g)	Fe_2O_3/SiO_2
MN010	0.10	2.5	1.5	3.5	0.14
MN025	0.25	2.5	1.5	3.5	0.35
MN050	0.50	2.5	1.5	3.5	0.70
MN100	1.00	2.5	1.5	3.5	1.39
MN150	1.50	2.5	1.5	3.5	2.08

4.2.2.1 Thermal Properties

Fig. 4.32 shows the TGA curves of the samples. The MN samples and silica gel matrix (S1) exhibit similar behaviour. A minor weight loss is observed at around 100^{o}C, which is mainly due to the evaporation and dehydration process and a major weight loss is observed at around 250^{o}C. The second weight loss is due to the dehydration and evaporation of sol-gel solvent and water trapped within the silica xerogel network and pores.

A total weight loss of about 26-48% is observed upon heating over the range from room temperature to 700^{o}C, as shown in Table 4.14. No obvious trend is observed for the samples' weight loss.

Table 4.14:
Percentage Weight Loss of Samples

Sample	Weight loss (%)
S1	26.05
M10	18.78
MN010	26.47
MN025	31.92
MN050	48.77
MN100	40.13
MN150	29.24

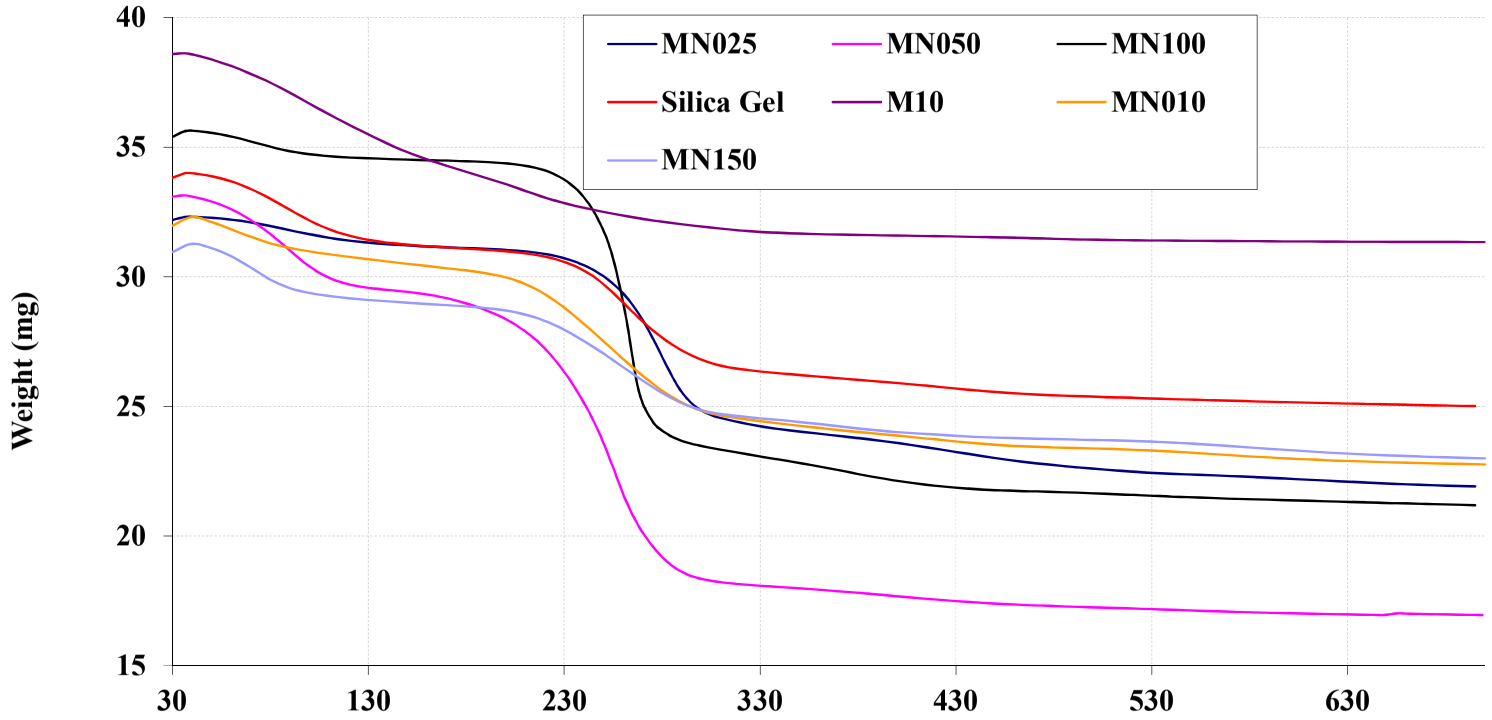

Figure 4.32:
TGA Curves for Samples

4.2.2.2 Phase and Crystal Structure

Figures 4.33 and 4.34 show the XRD diffraction patterns for the as-prepared nanocomposites. The XRD diffraction patterns for samples MN025, MN050, MN100 and MN150 clearly show the reflection corresponding to maghemite nanoparticles and a visible broad diffraction shoulder is observed at 2θ from 20 ^{o} to 35 ^{o}, which are characteristics of the amorphous phase of the silica gel. In addition, the patterns exhibit the presence of only maghemite and SiO_2 amorphous phase, which indicates that there are no chemical reactions between the silica xerogel and maghemite nanoparticles to form other compounds. In fact, for sample MN010, the extra peaks observed are contributed by the silica crystalline phase and not the amorphous gel phase. This indicates that some of the amorphous phase already transformed to crystalline phase. Therefore, further investigations were not carried out for this sample.

From the patterns, the corresponding peaks observed are located at around 2θ = 30 ^{o}, 35 ^{o}, 43 ^{o}, 57 ^{o} and 63 ^{o}. These peaks match well with the ICDD PDF Card Number 39-1346, which proves that no phase transformation occurs during the encapsulation process. Additionally, the broadening of the (311), (511) and (440) reflections increase in the order of MN150, MN100, MN050 and MN025. The observed trend suggests a possible decrease in crystallite size when the concentration of maghemite nanoparticles is decreased or in other words, with decreasing weight ratio of Fe_2O_3/SiO_2. The broadening and low intensities of the peaks indicate that the crystallite sizes of the samples are within the nanometre scale for all samples. The average crystallite sizes of the samples were calculated from the major peaks using Equation 4.1 and the details are shown in Table 4.15 and Fig. 4.35.

The calculated crystallite sizes are 2.57 nm, 4.58 nm, 5.14 nm and 6.82 nm for samples MN025, MN050, MN100 and MN150 respectively. Comparison of the average crystallite size between samples M10 and MN shows that the encapsulated maghemite nanoparticles have a smaller average crystallite size, except for sample MN150.

Sample MN150 shows a larger crystallite size compared with sample M10, which may be due to the limitation imposed by the amount of maghemite nanoparticles dispersed in the xerogel matrix. When the limit is exceeded, the nanoparticles are unable to disperse well in the matrix, which leads to agglomeration and aggregation. The pores are insufficient to cope with the amount of maghemite nanoparticles added. This may be also due to the gelation time, which is inadequate to disperse the maghemite nanoparticles sufficiently into the matrix.

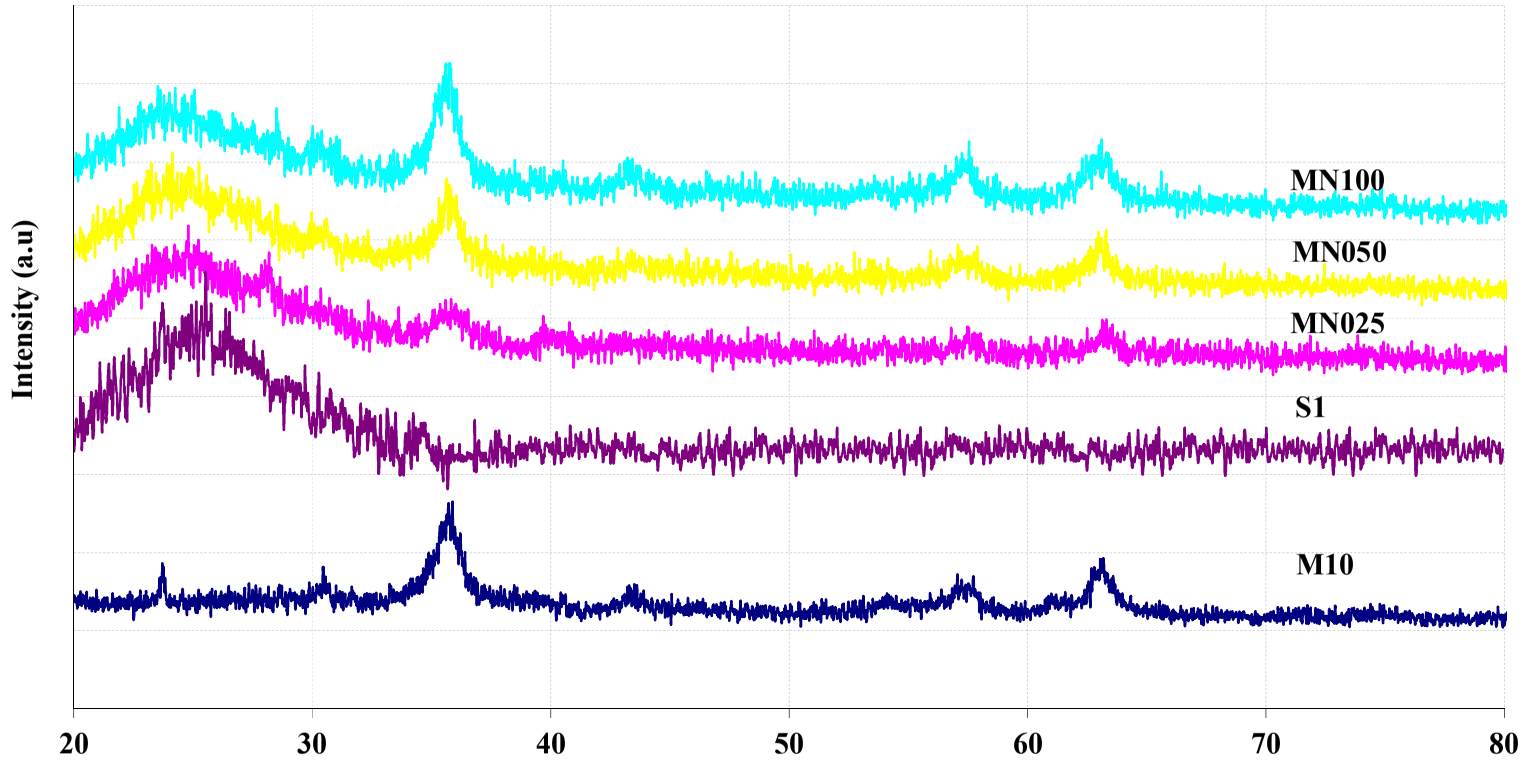

Figure 4.33:
XRD Curves for M10, S1, MN025, MN050 and MN100

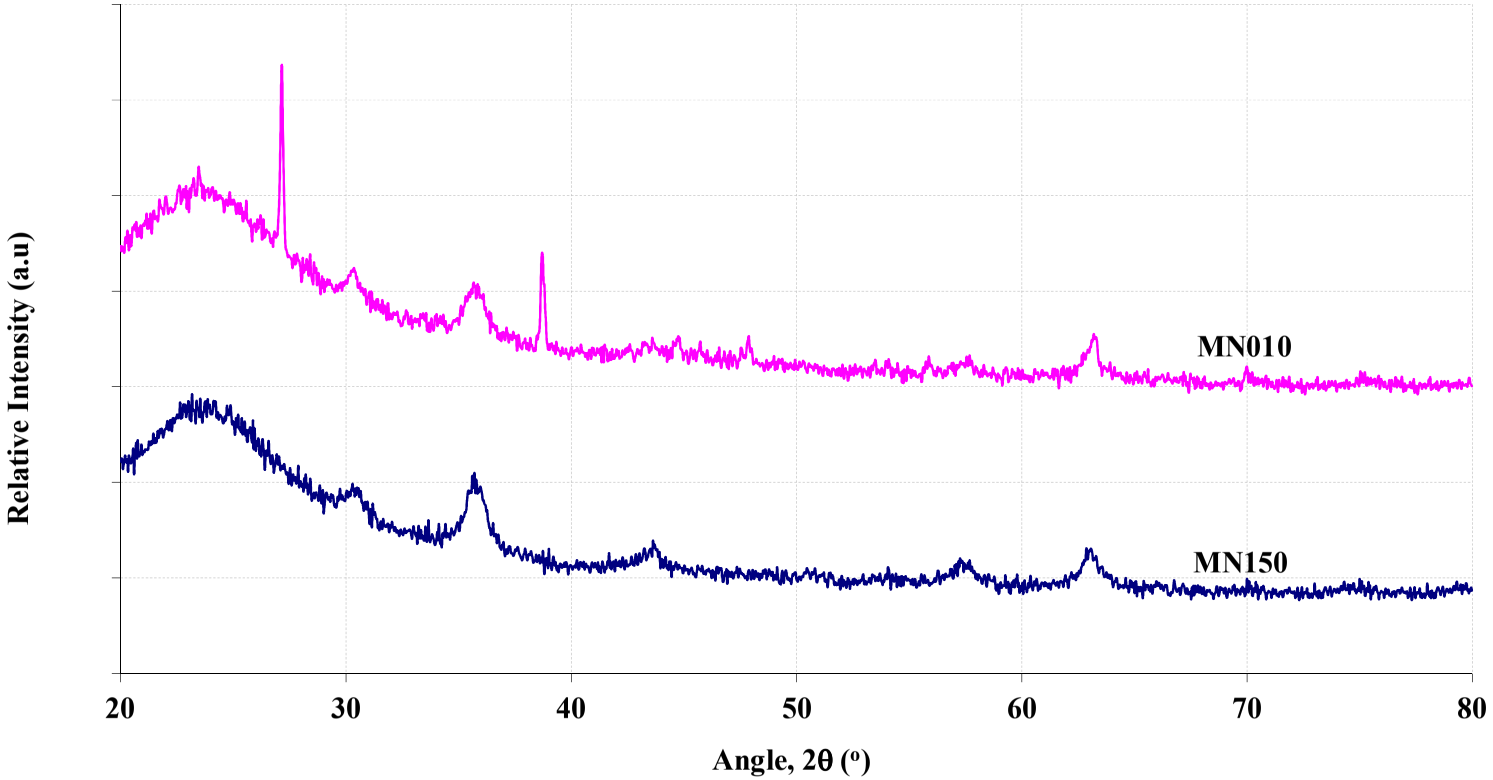

Figure 4.34:
XRD Curves for MN100 and MN150

Table 4.15:
Crystallite Size for Samples

Sample	2θ (^{o})	θ (rad)	cos θ	$W_{b(sample)}$	$W_{s(standard)}$	Crystallite Size (nm)
M10	35.5792	0.31053	0.95217	1.245	0.0531	6.09
	62.8507	0.54855	0.85328	1.1066	0.1618	6.20
					Average	**6.14**
MN025	35.6966	0.31155	0.95186	2.2884	0.0531	3.31
	63.456	0.55383	0.85052	3.6808	0.1618	1.84
					Average	**2.57**
MN050	35.6917	0.31151	0.95187	1.4802	0.0531	5.12
	63.0062	0.54990	0.85257	1.6876	0.1618	4.04
					Average	**4.58**
MN100	35.601	0.31072	0.95211	1.184	0.0531	6.40
	62.9003	0.54898	0.85306	1.753	0.1618	3.89
					Average	**5.14**
MN150	35.7492	0.31201	0.95172	1.0008	0.0531	7.57
	63.0095	0.54993	0.85256	1.1292	0.1618	6.07
					Average	**6.82**

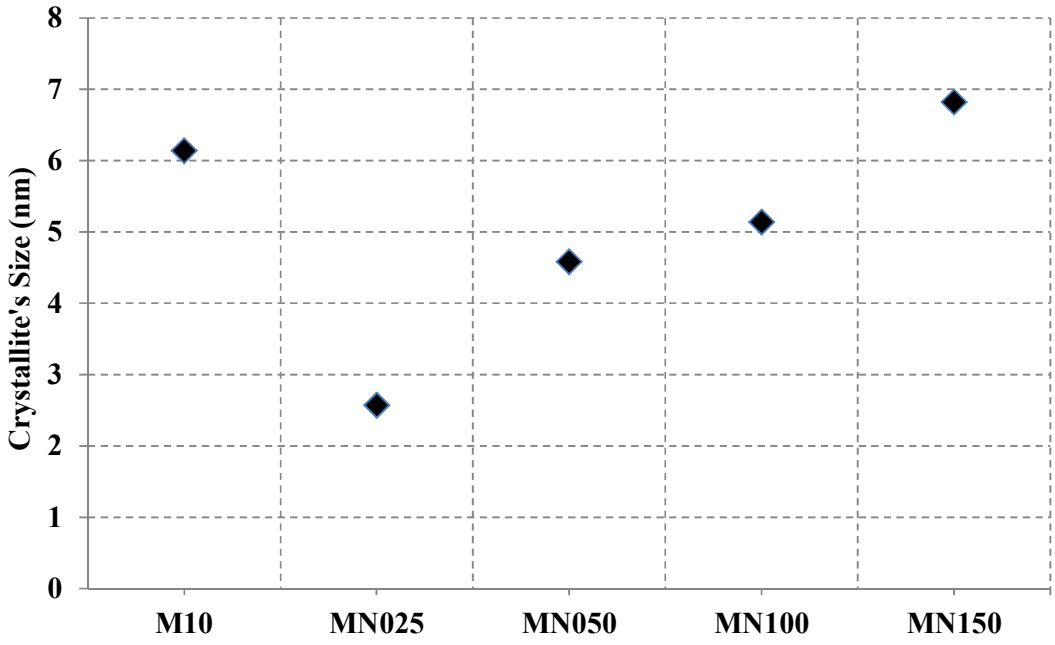

Figure 4.35:
Crystallite Size Comparison for Samples

4.2.2.3 Morphology and Physical Size

Figs. 4.36(a) – 4.39(a) show the TEM micrographs of samples, which reveal a very homogeneous dispersion of isolated maghemite nanoparticles over silica xerogel matrix in samples MN025, MN050 and MN100. The TEM observation in dark field mode (Fig. 4.40(a)) also reveals that the nanoparticles are distributed randomly within the silica matrix, without massive aggregation. ESI analysis is carried out, which proves that the Fe particles are well distributed and surrounded by Si compound (Fig. 4.41). However, some large and irregular aggregations of nanoparticles within the silica matrix are observed in MN150, which are not present in other samples. The aggregation of particles is caused by the gelation process during SiO_2 formation. The time for the maghemite nanoparticles to disperse completely into the pores of the network form of

silica matrix is insufficient before the system turns into gel. The high maghemite content may give rise to large nanoparticles, which prevents a homogeneous and well dispersed distribution in the host silica xerogel matrix.

The TEM physical size distribution histograms are shown in Figs. 4.36 (b) – 4.39 (b). The calculated TEM physical mean diameters decrease constantly from sample MN150 to MN025 (Fig. 4.41), confirming that the peak broadening observed in the XRD spectra is due to the reduction in maghemite nanoparticle size. The calculated average diameters are 4.40 nm, 4.61 nm, 5.23 nm and 7.25 nm for samples MN025, MN050, MN100 and MN150, respectively. The standard deviations for the samples are 1.30, 1.68, 1.72 and 2.84 for samples MN025, MN050, MN100 and MN150, respectively. The low standard deviation indicates that the data points tend to be very close to the mean. This indicates that MN025 has a narrower size distribution and a smaller average diameter compared with other samples. The standard deviation exhibits an increasing trend with increasing Fe_2O_3/SiO_2 ratio. These results indicate that increasing the ratio of Fe_2O_3/SiO_2, leads to an increased particle size and a wider size distribution. These results agree well with the other results obtained.

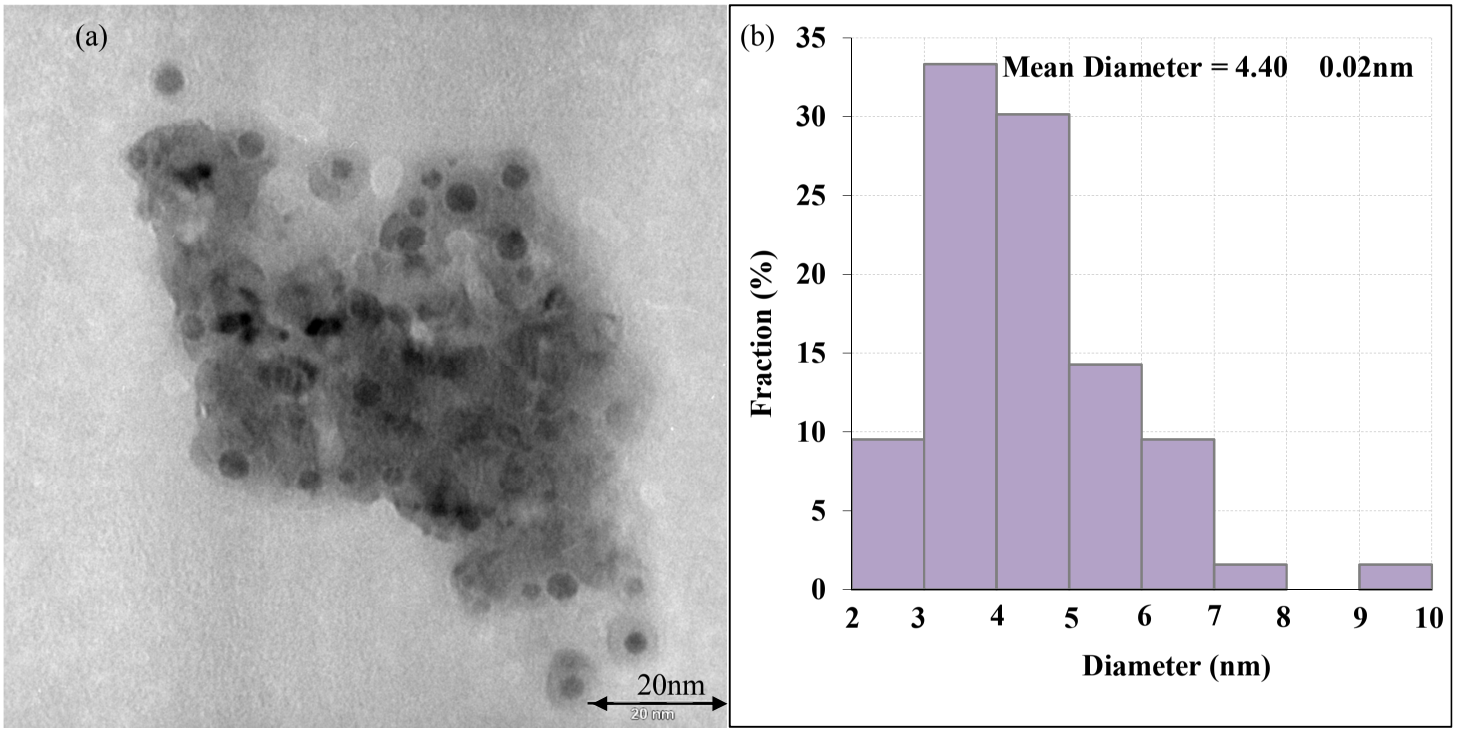

Figure 4.36:
(a) TEM Micrograph and (b) Size Distribution Histogram of MN025

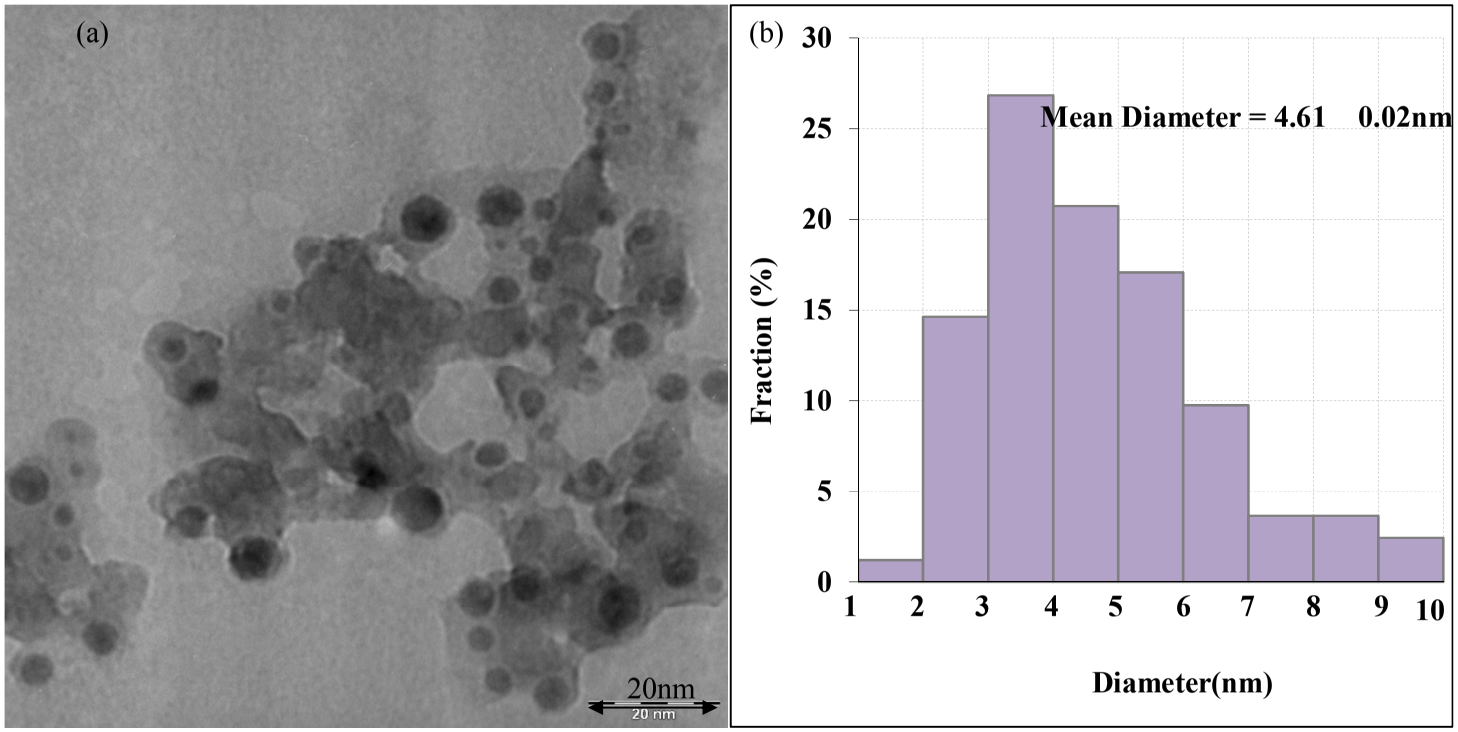

Figure 4.37:
(a) TEM Micrograph and (b) Size Distribution Histogram of MN050

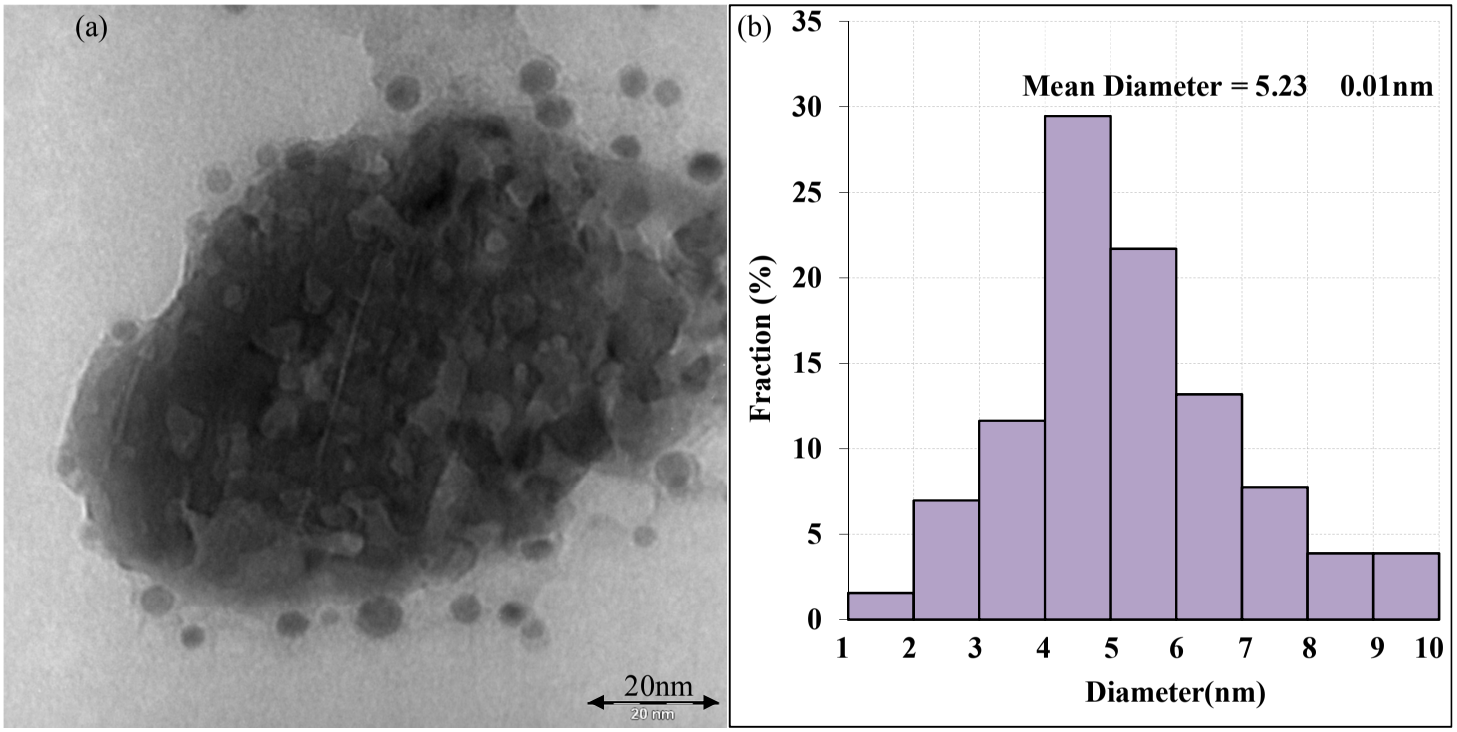

Figure 4.38:
(a) TEM Micrograph and (b) Size Distribution Histogram of MN100

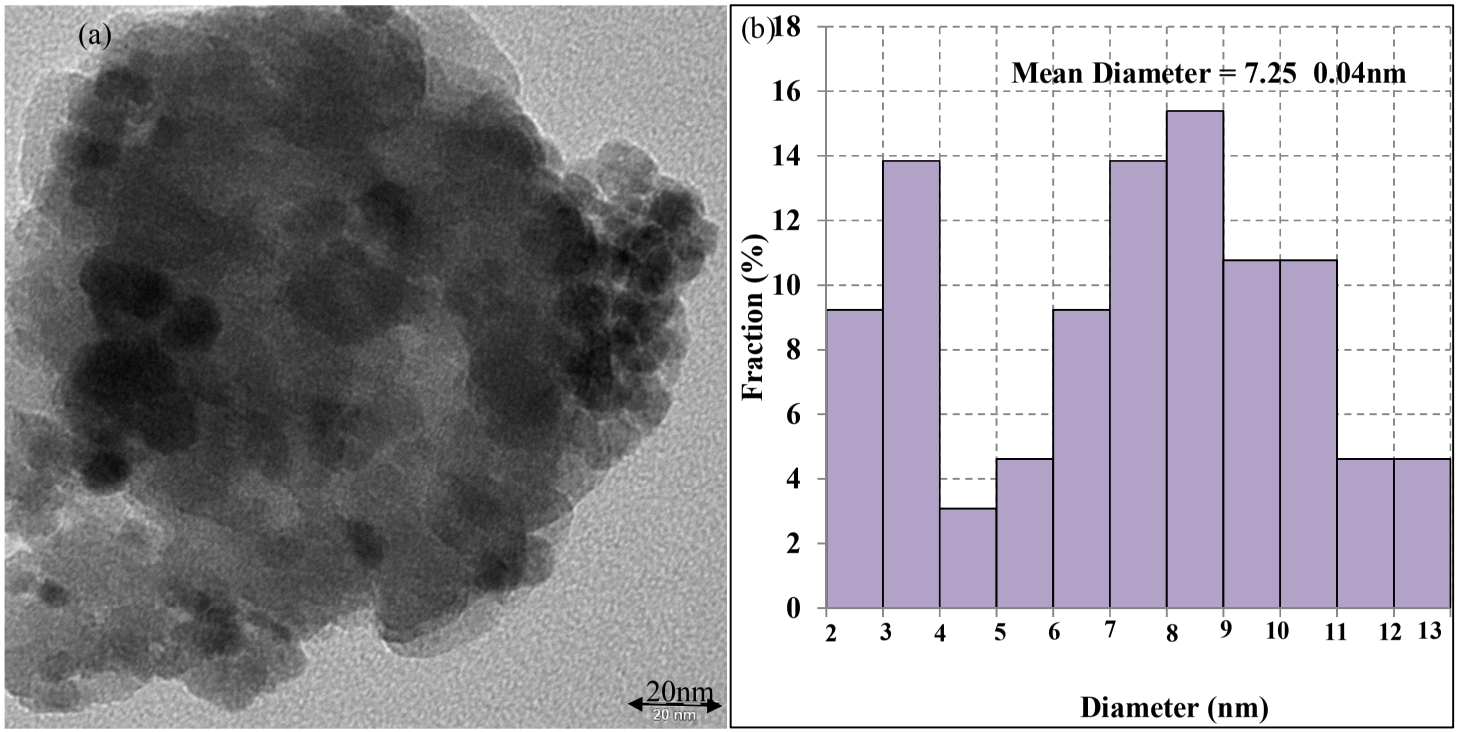

Figure 4.39:
(a) TEM Micrograph and (b) Size Distribution Histogram of MN150

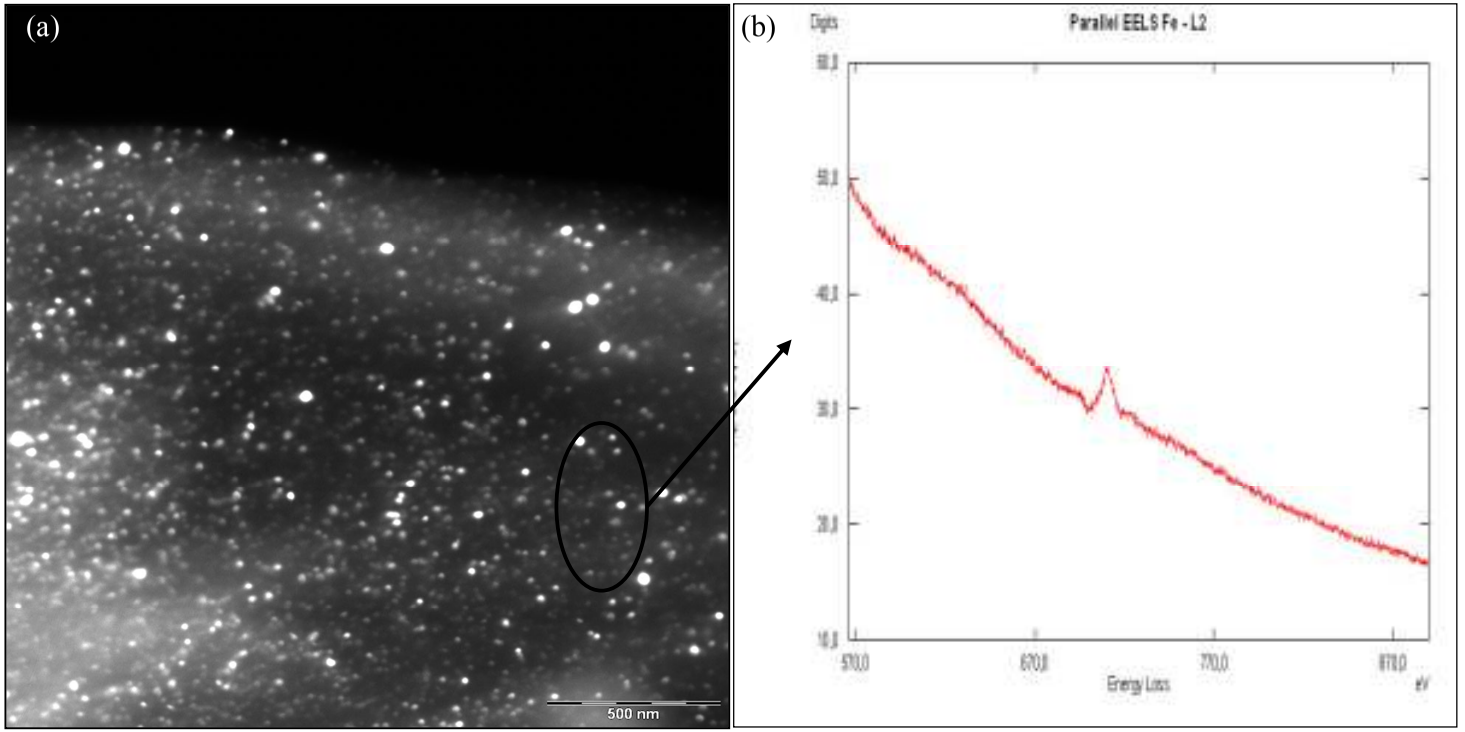

Figure 4.40:
(a) TEM Micrograph in Dark Field Mode and (b) EELS of MN025

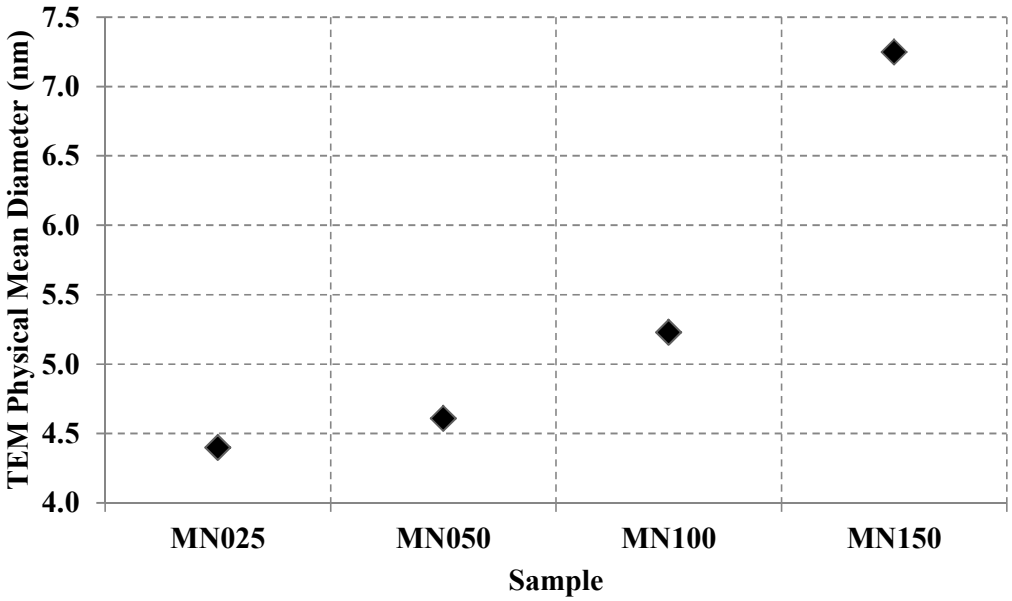

Figure 4.41:
TEM Physical Mean Size for Samples

EELS analysis was carried out for sample MN025 (Fig. 4.40), which shows the presence of Fe-L_2 signals and indicates that the particles observed in micrographs are iron based compounds.

The micrographs of samples M10 (Fig. 4.7) and MN025 (Fig. 4.36(a) in bright field and Fig. 4.40(a) in dark field) are compared. The particles in sample M10 are in spherical shape and form agglomerates, whereby the particles in sample MN025 show a very homogeneous dispersion of isolated nanoparticles. This means that the agglomeration problem is minimized when maghemite nanoparticles are encapsulated in silica xerogel matrix. Silica matrix works as a physical barrier to block the long-range magnetic dipole-dipole interactions between the particles and prevents the agglomeration problem caused by the drying process during TEM sample preparation. The measured average diameters for samples M10, MN025 and MN050 are 4.98 nm,

nanoparticles. This is further proven by the EDX result in Fig. 4.44, which shows that only Si, O and Fe are present. The intensity of the Fe signal is lower, which is attributed to the fact that most of the maghemite nanoparticles are embedded within the silica gel and not on the surface. The measured average physical pore size diameter is about 15 nm, whereas the average physical size of maghemite nanoparticles is about 4.98 nm. The size of the pores is nearly three times bigger than the size of the as-synthesized maghemite nanoparticles. This enables the nanoparticles to fill the pores easily. Moreover, the additional 3 hours of stirring is sufficient to form the silica network surrounding the nanoparticles, which hinders further agglomeration caused by magnetic dipole-dipole interaction between the nanoparticles. However, there could be other factors which contribute to the change in surface morphology structure such as the formation of a different phase of silica. From the FESEM micrographs, it can also be observed that some of the maghemite nanoparticles form agglomerates on the surface such as in samples MN100 and MN150.

EDX analysis was carried out to study the elemental composition of the samples. The percentage of each element from estimation and observation is listed in Table 4.16. The result shows the prepared nanocomposites have similar elemental percentage as the estimation values.

The result of EDS analysis is shown in Fig. 4.45 and it can be seen that the encapsulated maghemite nanoparticles are well distributed within the silica xerogel matrix.

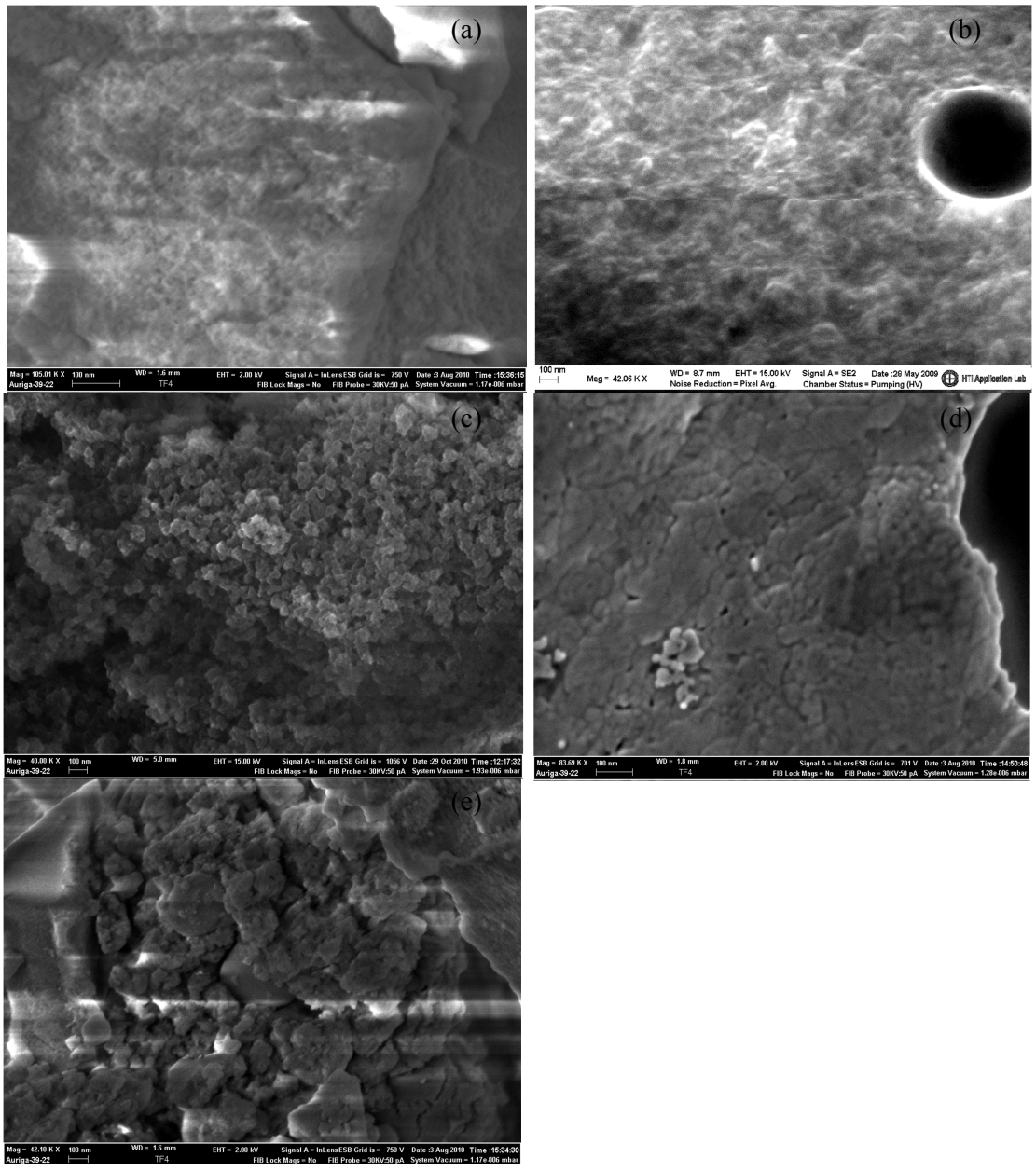

Figure 4.43:
FESEM Micrographs for (a) MN010, (b) MN025, (c) MN050, (d) MN100 and (e) MN150

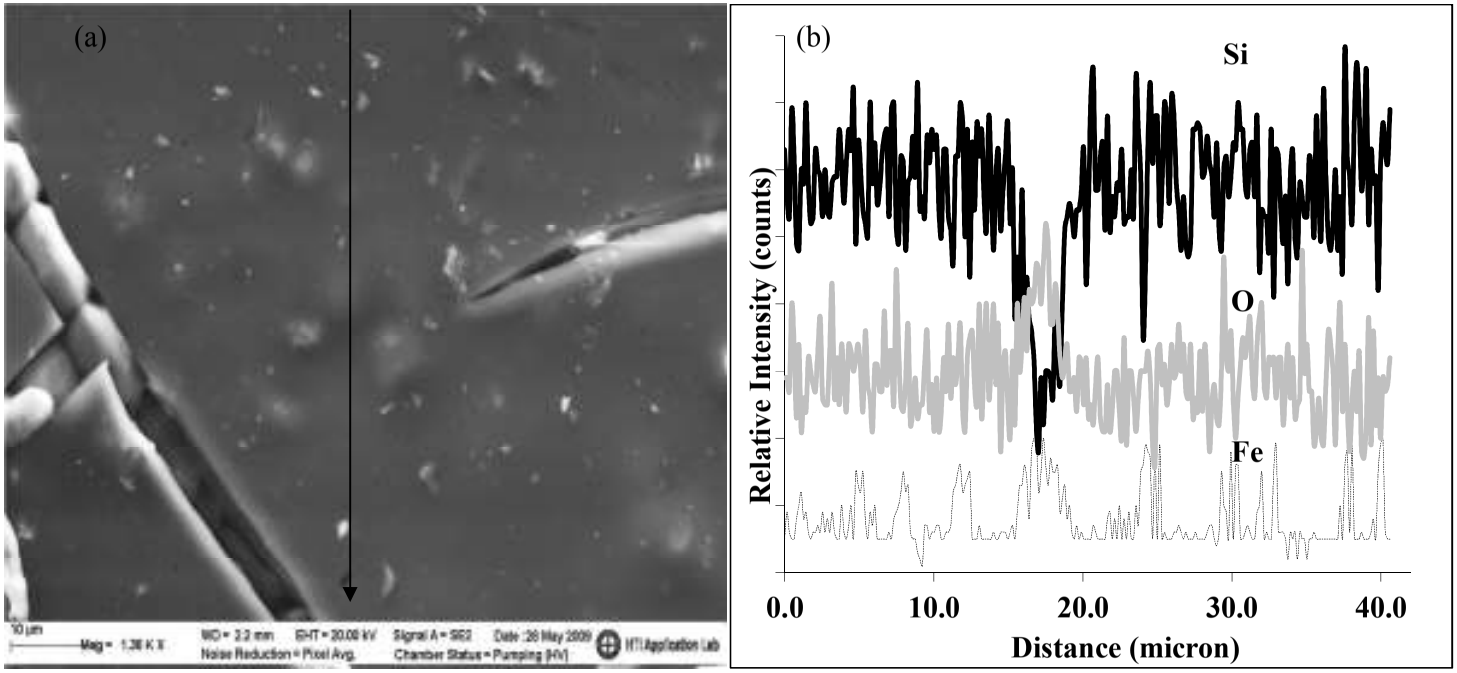

Figure 4.45:
FESEM Micrograph and (b) EDS Line Analysis of MN025

4.2.2.4 Surface Area Analysis

The surface areas for the MN samples were studied by the N_2-gas absorption desorption method. Figs. 4.46 – 4.49 show the typical mesoporous graphs for samples MN025, MN050, MN100 and MN150. The samples exhibit similar N_2-gas adsorption desorption isotherms, and the primary difference is the size of the hysteresis loop. The unique features are (i) no adsorption at $P/P_o \rightarrow 0$, which indicates the absence of micropores for all samples; (ii) a relatively moderate increase in the adsorbed amount of N_2 within the P/P_o range of 0-0.9; (iii) a sharp increase in adsorbed N_2 within the P/P_o range of 0.9-1.0; (iv) the hysteresis loop is rather big and horizontally oriented; (v) the isotherms do not exhibit plateau at $P/P_o \rightarrow 1.0$, but they asymptotically approach the *y*-axis. These features correspond relatively well to Type IV isotherm.

Referring to Table 4.17, the surface areas obtained for nanocomposite samples (MN) are much lower compared to silica (S1) and maghemite nanoparticles (M1). Table 4.17 also shows that increasing the content of maghemite nanoparticles leads to reduced surface area for the nanocomposite systems (Fig. 4.50). This suggests that the pores of the silica matrix are almost fully filled. This is further proven by looking at the values of the specific pore volume listed in Table 4.17 and the hysteresis loop obtained from experiment. When more maghemite nanoparticles are added, smaller hysteresis loops are obtained. This indicates that the existing pores of the silica gel are filled with maghemite nanoparticles. The opening of the hysteresis loop for MN025 and MN050 are compared to sample MN100, which indicates that the distribution of the mesopores for MN025 and MN050 are shifted to a lower pore diameter, d_p. This shows that most of the micropores in the silica xerogel are filled when the amount of maghemite nanoparticles reaches a certain value. This is illustrated by the typical pore size

distribution calculated by the How/Kar method, as shown in Table 4.17 (Gulkova et al., 2004).

The TEM micrograph in Fig. 4.36 clearly shows that the embedded maghemite nanoparticles are isolated by the pores within the silica xerogel matrix. The calculated crystallite and physical sizes from XRD and TEM prove that the sizes of embedded nanoparticles are smaller than the original maghemite nanoparticles, as reported by Ang and Yaacob (Ang and Yaacob, 2010).

Table 4.17:
Specific Surface Area (BET) and Pore Specific Volume of Samples

Sample	Specific Surface Area (m^2/g)	Pore Specific Volume (cm^3/g)
MN025	38.25	0.0729
MN050	20.93	0.0470
MN100	17.18	0.0617
MN150	15.8	0.0286

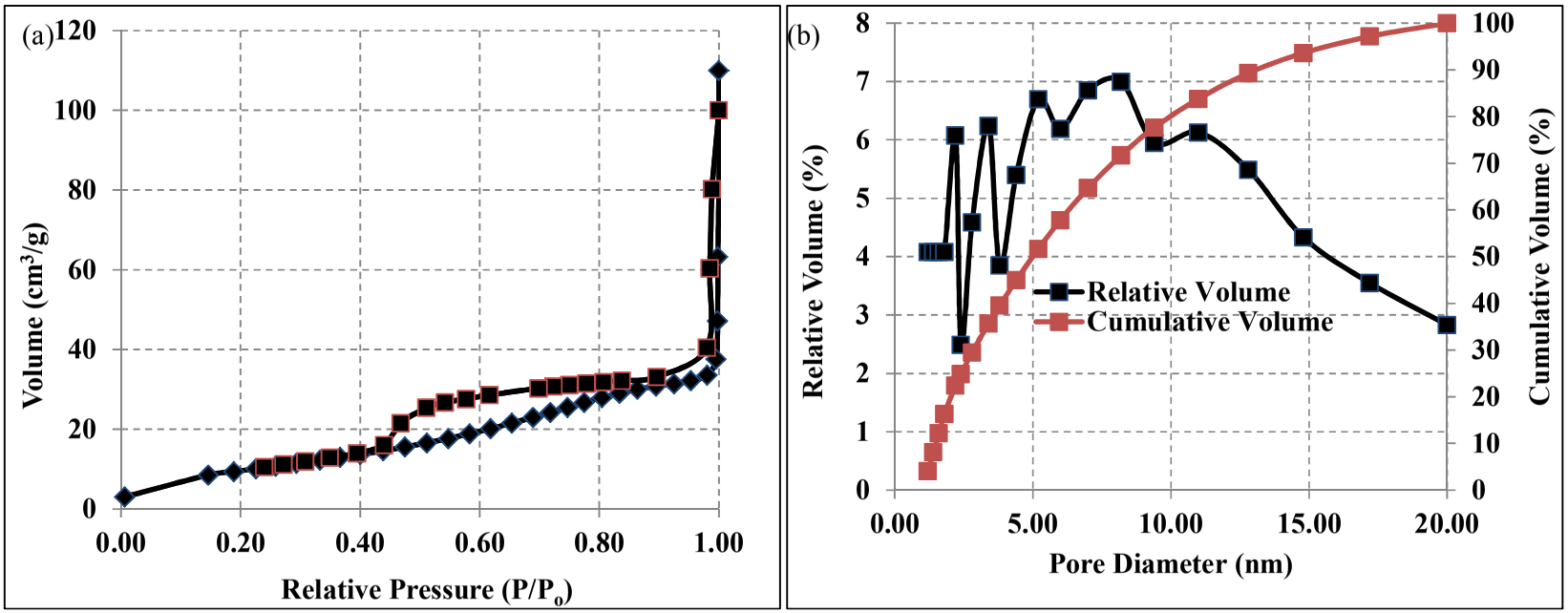

Figure 4.46:
(a) N_2-gas Adsorption Desorption Isotherm and (b) Pore Size Distribution of MN025

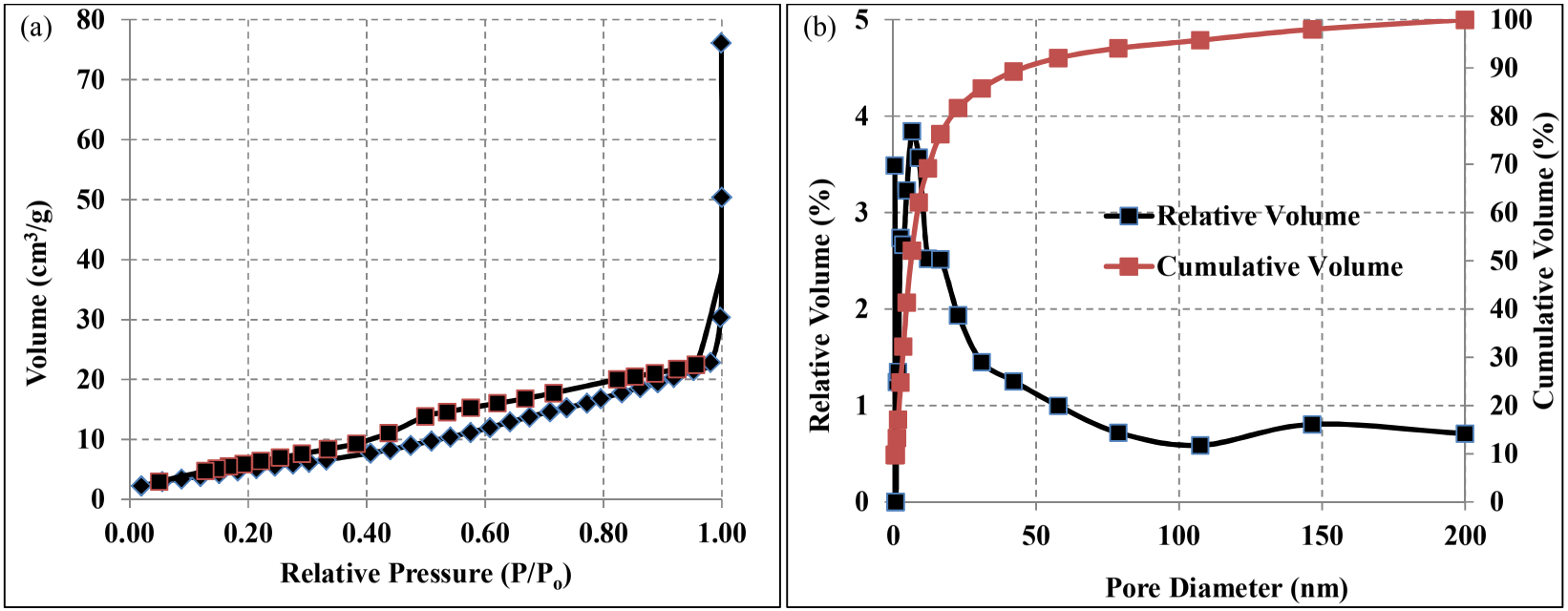

Figure 4.47:
(a) N_2-gas Adsorption Desorption Isotherm and (b) Pore Size Distribution of MN050

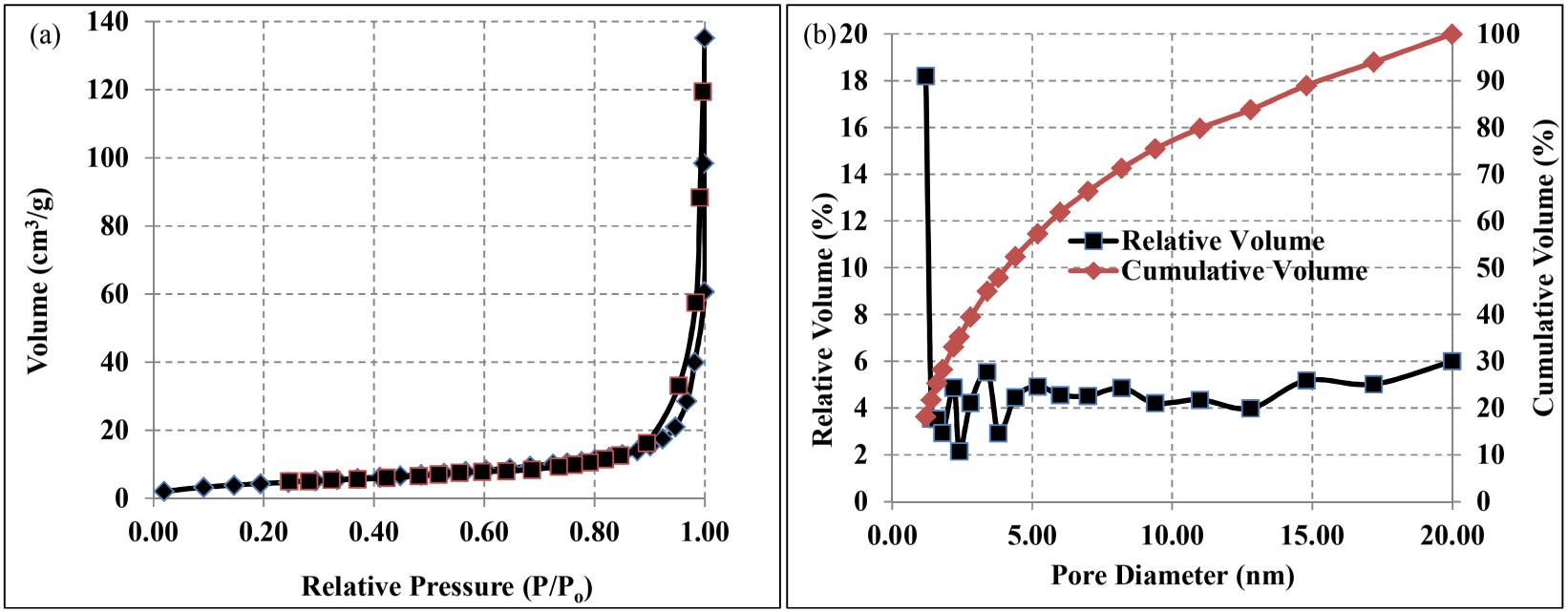

Figure 4.48:
(a) N_2-gas Adsorption Desorption Isotherm and (b) Pore Size Distribution of MN100

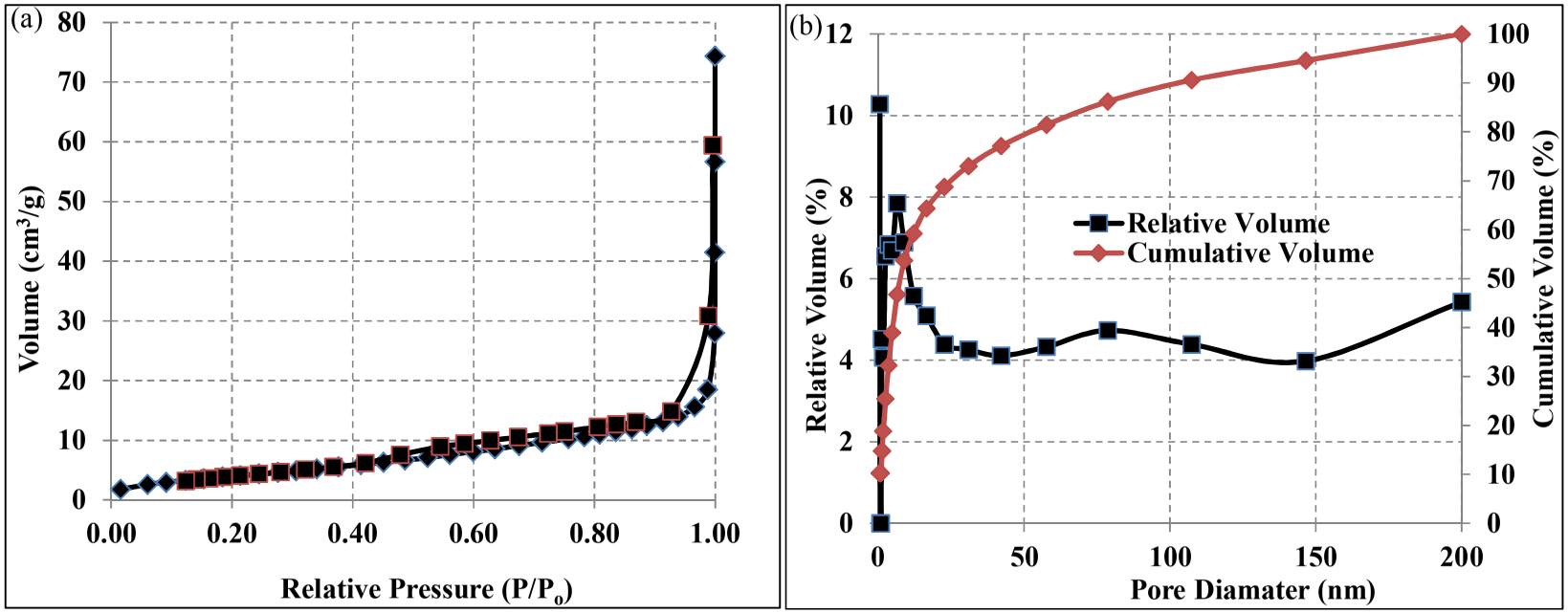

Figure 5.49:
(a) N_2-gas Adsorption Desorption Isotherm and (b) Pore Size Distribution of MN140

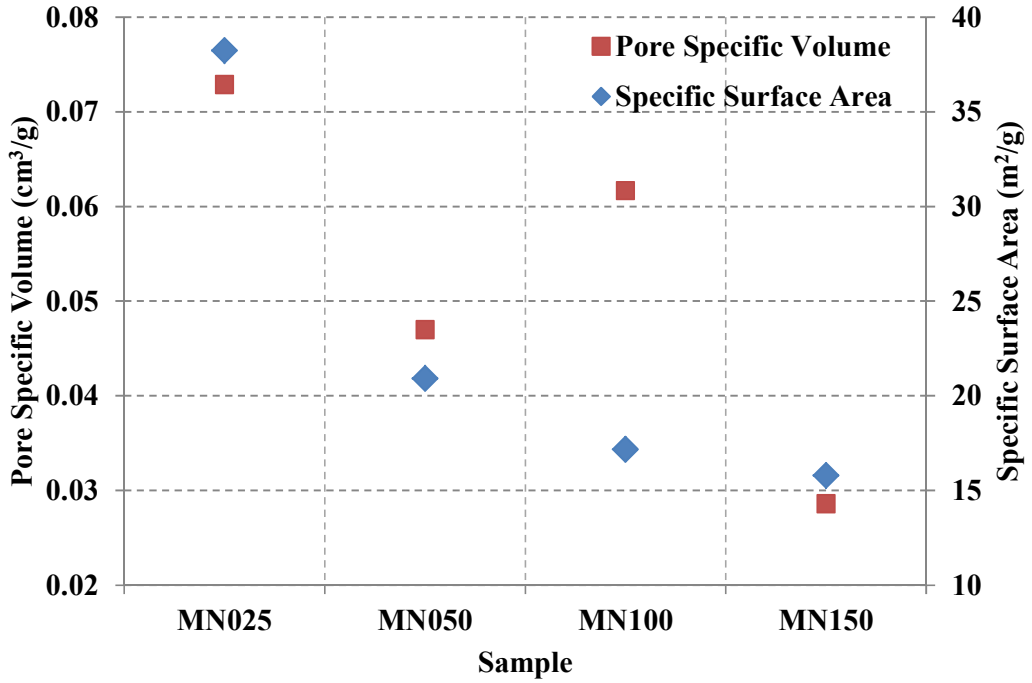

Figure 4.50:
Specific Surface Area (BET) and Pore Specific Volume of Samples

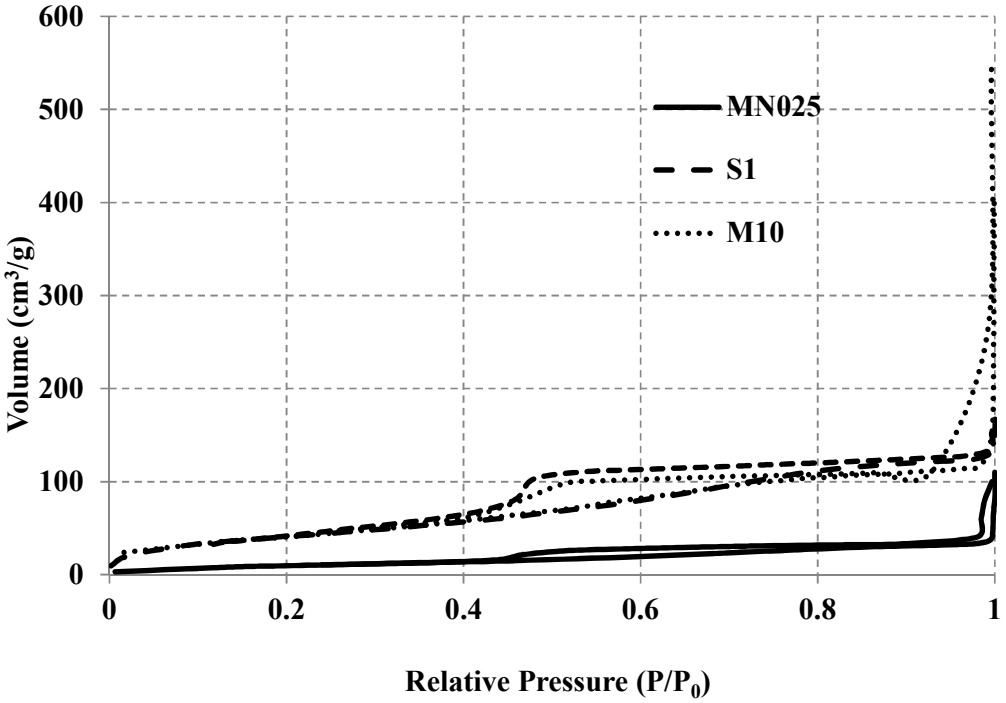

Figure 4.51:
N_2-gas Adsorption Desorption Isotherms for Samples M10, S1 and MN025

Comparisons are made for samples S1, M10 and MN025. The features of the isotherms change when maghemite nanoparticles are added. Among these samples, only the silica gel shows microporous behaviour as the adsorption at $P/P_o \rightarrow 0$ is moderately high, which indicates a small amount of micropores. A larger hysteresis loop is also observed for sample S1, which contains a higher number of pores. Hysteresis loop occurs due to condensation and evaporation processes in the pores which do not necessarily take place as exact reversals of each other. A larger hysteresis loop indicates a higher number of pores (Greg and Sing, 1982b). Samples S1 and M10 exhibit bigger hyteresis loops compared with the MN samples (Fig. 4.51).

4.2.2.5 Magnetization Analysis

Fig. 4.52 shows the magnetization curves for MN samples. The shapes of the magnetization curves for nanocomposites are very similar to the original sample. Superparamagnetic behaviour is observed for all samples, indicating that the size of maghemite nanoparticles is always within the nanometre range. The increase in iron content gives rise to a small particle growth.

The decrease in magnetization values relative to sample M10 also reflects the standard practice of normalizing the magnetization by sample mass. For nanocomposites, there is less magnetic material per gram of sample, and the magnetization readings are divided by the substantial mass of silica. As a result, both the saturation and remanent magnetization values decrease upon the encapsulation process. Attempts to quantify the percentage of magnetic material in order to normalize by mass of magnetic material have been unsuccessful, as methods to dissolve the silica

matrix also destroy or alter the maghemite nanoparticles (Vestal and Zhang, 2003). The value of M_r/M_s does not change significantly for the as-synthesized maghemite nanoparticles and maghemite nanocomposites. The consistency in shape of the hysteresis curves further confirms that the decrease in magnetization is primarily due to a lower amount of magnetic material per mass and a slight dissolution of maghemite nanoparticles.

The magnetization values at an applied field of 10 kOe (Ms_{10kOe}) and the least upper bound of the 'magnetic' size for all samples are listed in Table 4.18, and are shown in Figs. 4.53 and 4.54. The results indicate that when the ratio of Fe_2O_3/SiO_2 increases, the magnetic size increases. The results obtained from AGM correlate well with those from TEM and XRD measurements.

Table 4.18:
Magnetic Size for Samples

Sample	Magnetization Saturation (emu/g)	dM/dH	Magnetic Size (nm)
M10	9.53	0.02205	5.92
MN025	1.79	0.00285	3.01
MN050	3.12	0.00480	3.59
MN100	5.94	0.00965	4.45
MN150	6.80	0.01120	4.76

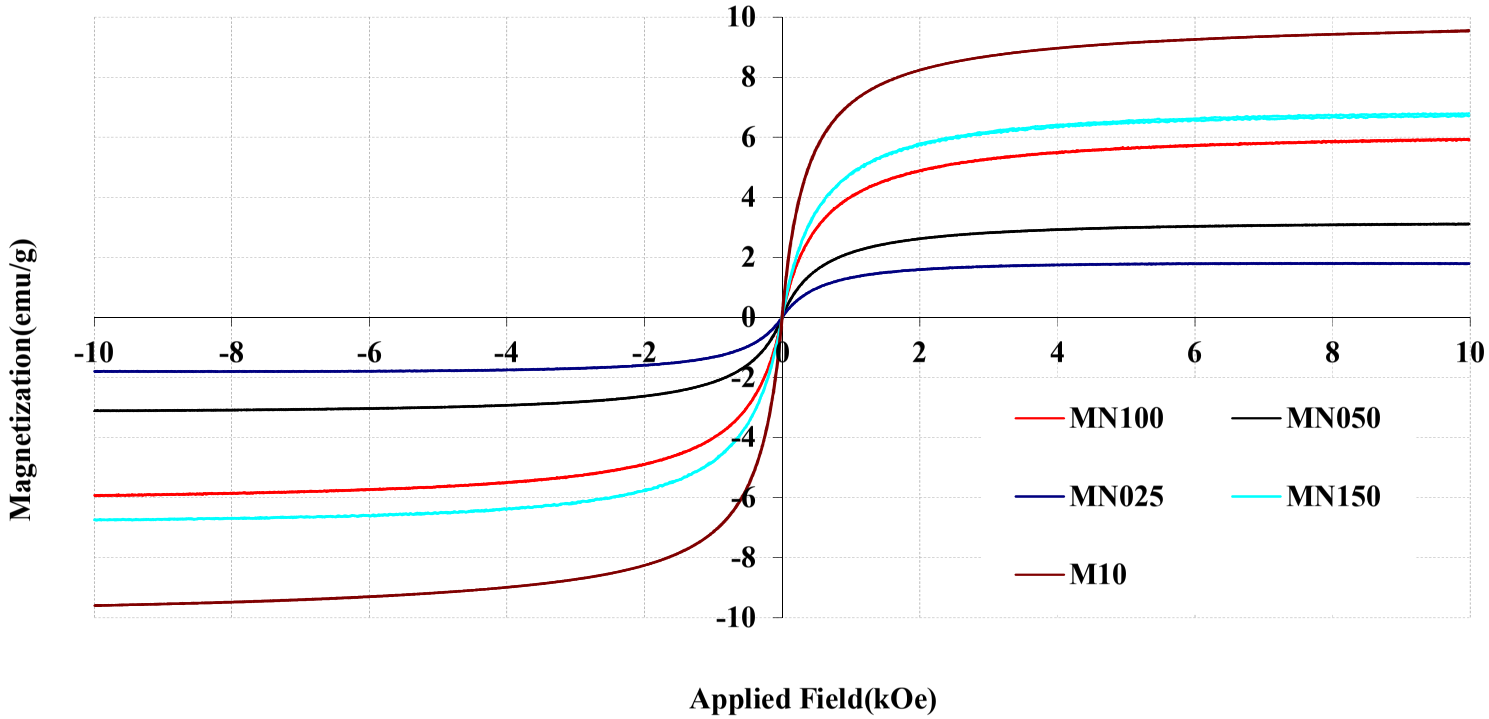

Figure 4.52:
AGM Curves for Samples

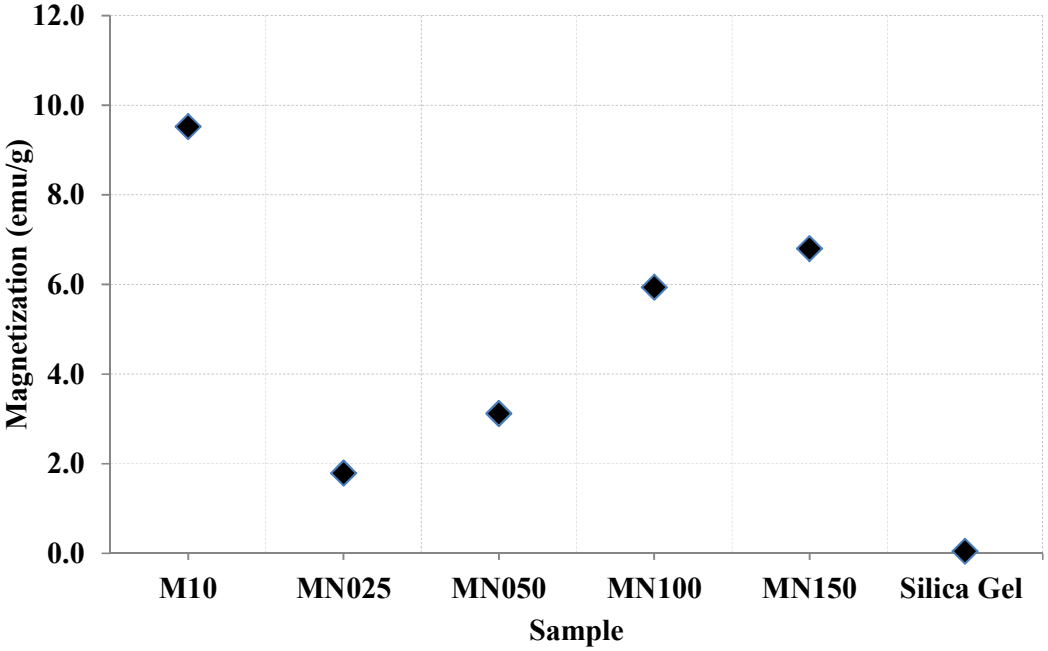

Figure 4.53:
Magnetization at 10kOe Applied Field (M_{s10kOe}) for Samples

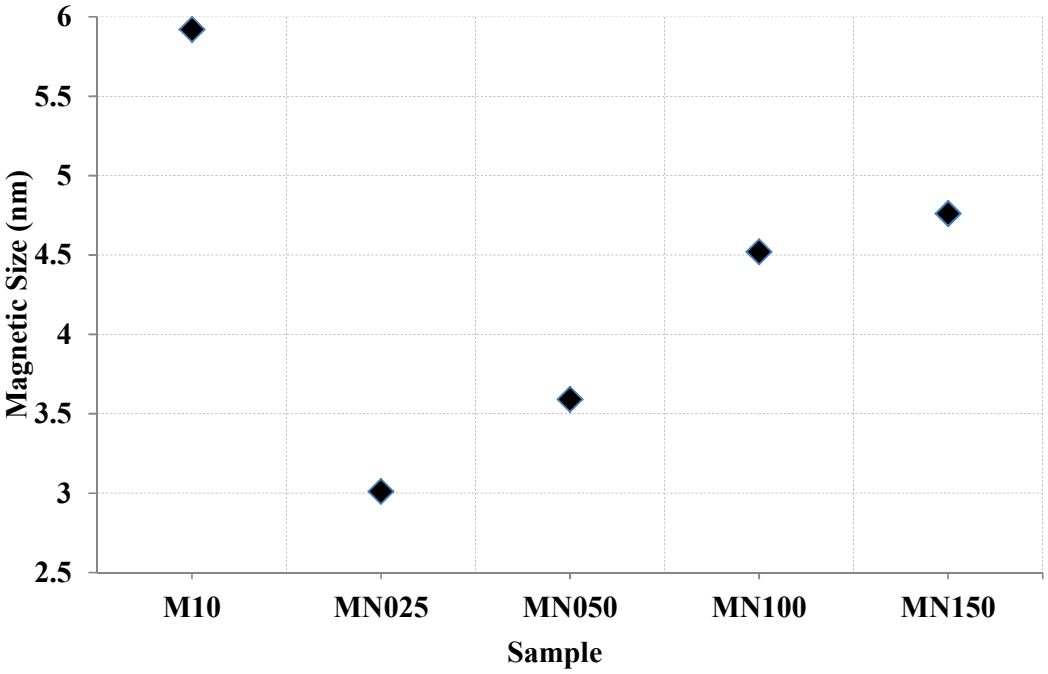

Figure 4.54:
Magnetic Size for Samples

4.2.3 Summary for Stage II

Table 4.19:
Details for Samples

Sample	XRD Crystallite Size (nm)	TEM Physical Size (nm)	AGM Magnetic Size (nm)	BET Surface Area (m^2/g)
M10	6.14	4.98	5.92	154.37
MN025	2.57	4.40	3.01	38.25
MN050	4.58	4.61	3.59	20.94
MN100	5.14	5.23	4.45	17.18
MN150	6.82	7.25	4.76	15.80

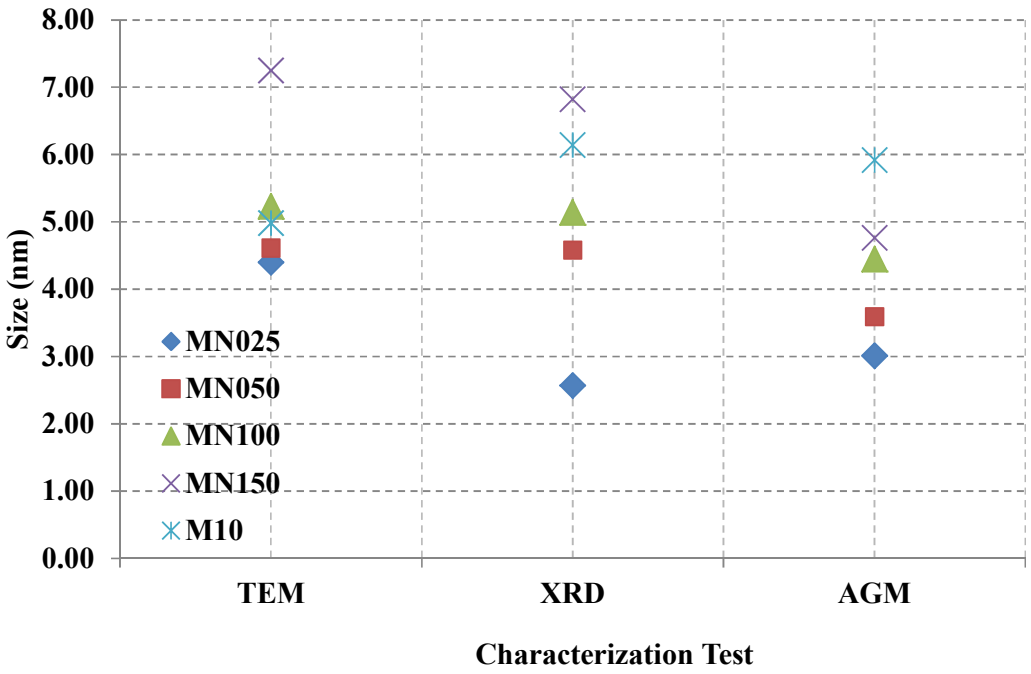

Figure 4.55:
Size Comparison Graphs for Samples

Fig. 4.55 and Table 4.19 show the results for stage II. A few conclusions can be made for this stage. Firstly, increasing the ratio of Fe_2O_3/SiO_2, increases the size of the encapsulated maghemite nanoparticles. The result also show that when the ratio is below 2.08 (samples MN025, MN050 and MN100), the calculated sizes are smaller than the as-synthesized maghemite nanoparticles (M10). This may be a result of slight dissolution of maghemite nanoparticles in the silica xerogel matrix. Furthermore, the pore structure of silica keeps the particles isolated and hinders their coalescence and growth. The pore structure of the matrix and the interactions between the magnetic clusters and the host can be employed to control the stability of the nanoparticles.

However when the ratio of Fe_2O_3/SiO_2 goes beyond 2.08, the calculated size is bigger than M10. This may be due to the limitation imposed by the amount of maghemite nanoparticles which are dispersed in the xerogel matrix or the inadequate gelation time required for all nanoparticles to disperse well in the silica xerogel matrix. This is proven by TEM micrographs which show the agglomeration of the maghemite nanoparticles.

High surface area is crucial for nanoparticles especially during application. This stage shows that a very low surface area is obtained from all MN samples compared with M10 and pure silica xerogel (S1). For this reason, modifications are carried out in stage III to increase the surface areas of the nanocomposites and retain their properties simultaneously. Based on the results in stage II, only three samples are produced in stage III, having a Fe_2O_3/SiO_2 ratio value of 0.35, 0.70 and 1.39.

4.3 PREPARATION OF MAGHEMITE-SILICA PARTICULATE FORM NANOCOMPOSITES

The preparation process for silica xerogel matrix was modified to form silica particulate matrix. The purpose of changing the matrix from xerogel to particulate form was to increase the surface area and retain its properties. The first step involves modifying the pH and preparation conditions, which facilitates transforming the silica xerogel into silica particulate. Following this, nanocomposites were fabricated by embedding the as-synthesized maghemite nanoparticles into silica particulate matrix. This process is a promising alternative technique for fabricating nanocomposites because it is simple, manufacturable, inexpensive and fast. In addition, this process can be carried out at room temperature and the composition, crystalline distribution and properties of maghemite nanoparticles and maghemite nanocomposites can be controlled. Moreover, no surfactants or other unnecessary precursors are involved. The silica particulate matrix was prepared using only TEOS, ethanol and H_2O. The pH level was maintained at pH 10 after investigations. In this analysis, ammonium solution was used to control the pH level. The whole process was run in ultrasonic bath.

4.3.1 Formation of Pure Silica Particulate Phase Matrix

A control sample of pure silica particulate matrix was produced and labelled as P1. The pure silica particulate phase matrix was formed easily without a change in pH and additional ethanol. The silica particulate phase was formed when a premix solution of TEOS and H_2O was placed inside the ultrasonic bath.

However, a change in silica phase was observed when as-synthesized maghemite nanoparticles were added. The silica phase transformed from particulate to a network gel phase after the addition of maghemite nanoparticles (labelled as F1). Modifications were required only during the preparation of nanocomposites and not on the pure silica particulate phase matrix. Therefore, the following investigations were mostly focused on the nanocomposites rather than the pure silica particulate phase matrix. Fig. 4.56 shows a comparison between the physical appearance of the pure silica particulate phase, the gel phase after the addition of maghemite nanoparticles and the maghemite-silica particulate nanocomposite (MNP) after modifications.

Figure 4.56:
Images of (a) P1, (b) F1 and (c) MNP Nanocomposite.

Most of the characterization tests carried out for sample P1 reveal similar results to those for silica xerogel (S1) in terms of the thermal properties, phase and crystal structure and magnetization analysis. Therefore, the results mentioned above will not be discussed in this section.

4.3.1.1 Morphology and Physical Size Analysis

TEM and FESEM analyses were performed, which provide information on the physical and structural nature of the silica particulate matrix formed.

TEM micrograph in Fig. 4.57(a) shows that the silica particulates are spherical in shape. The particle sizes are distributed over a wide range. The average particle size was calculated from around 100 particles and was found to be 78 nm (Fig. 4.58).

FESEM micrograph in Fig. 4.57(b) shows the surface morphology of sample P1. It is clearly seen that the matrix formed is in spherical particulate form. The average physical particle size is approximately 63 nm. In comparison with sample S1 (Fig. 4.28), a network with pores is absent in sample P1. This proves the success of the phase transformation from gel to spherical particulate form.

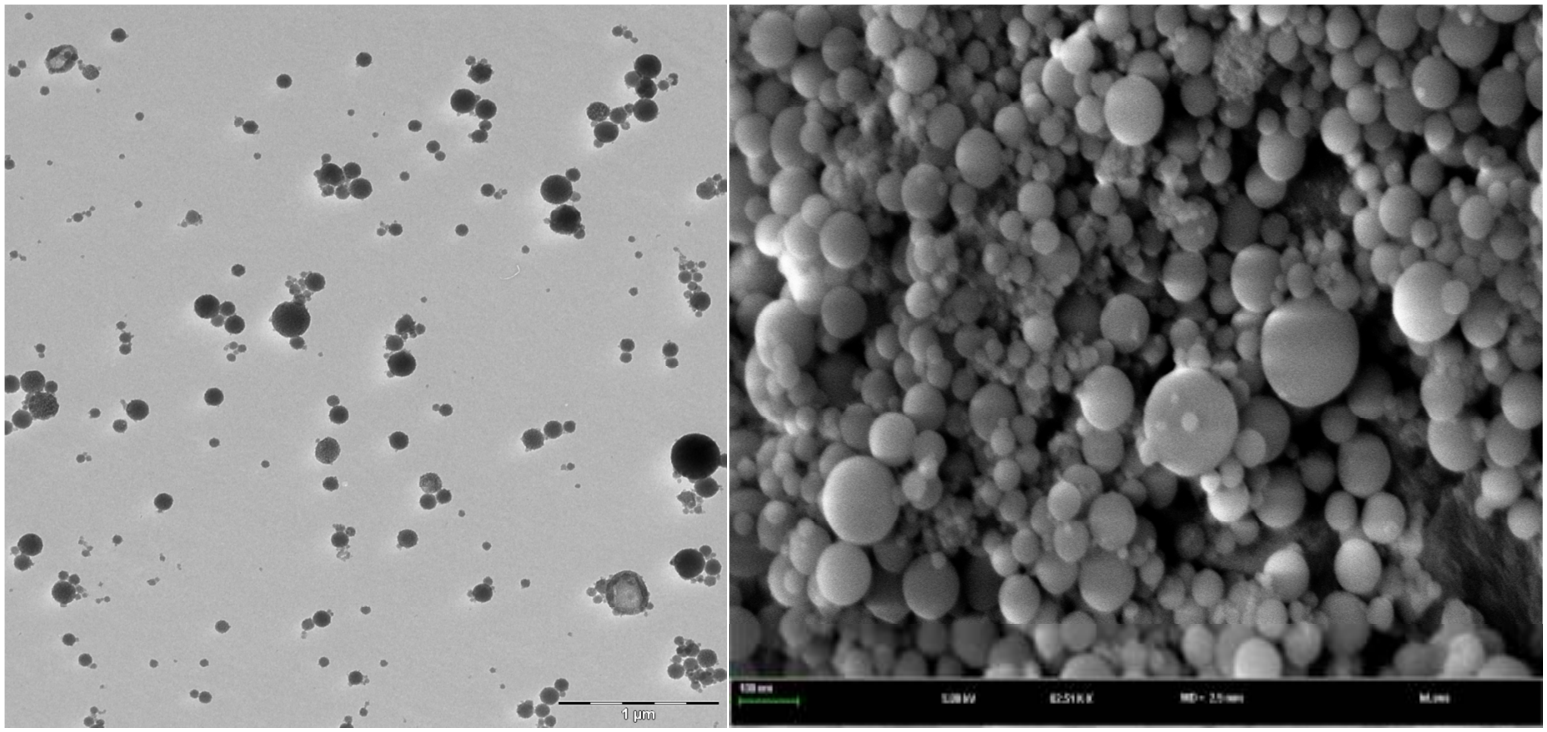

Figure 4.57:
(a) TEM micrograph and (b) FESEM Micrograph of P1

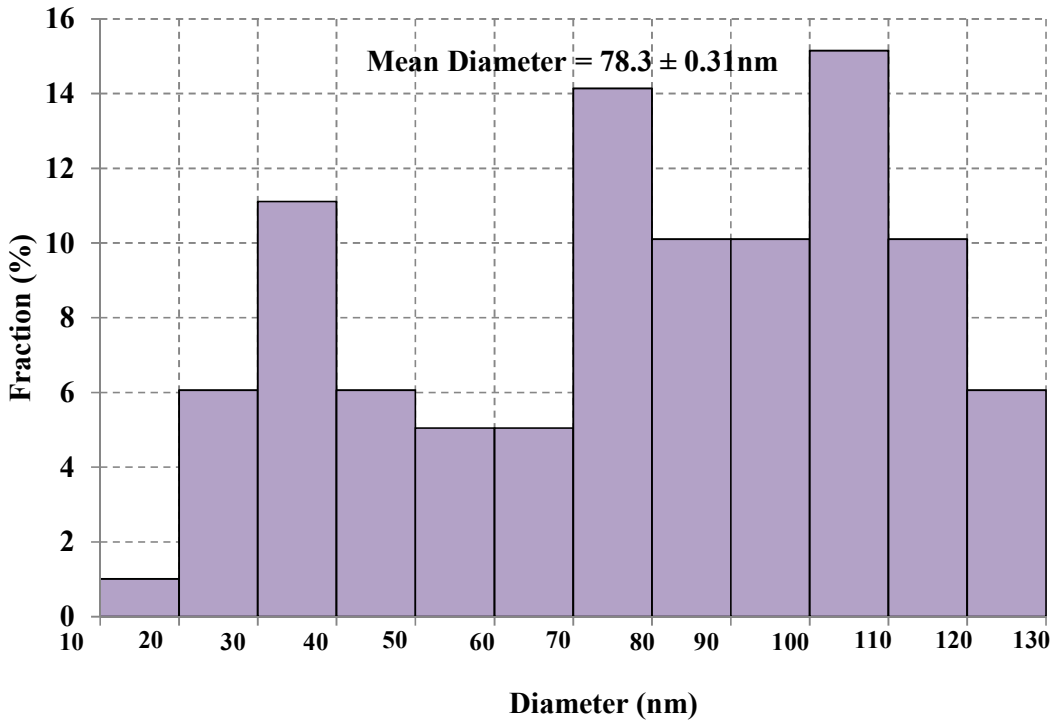

Figure 4.58:
TEM Size Distribution Histogram of P1

4.3.1.2 Surface Area Analysis

The surface area of P1 was studied by the N_2 adsorption desorption method. Fig. 4.59(a) shows a typical combination of microporous and mesoporous graph for sample P1. The unique features are (i) a slight increase in adsorption at $P/P_o \rightarrow 0$, which indicates a small amount of micropores; (ii) a relatively moderate increase in the adsorbed amount of N_2 within the P/P_o range of 0.1-0.8; (iii) a sharp increase in adsorbed N_2 within the P/P_o range of 0.8-1.0; (iv) the hysteresis loop is rather small and horizontally oriented; (v) the isotherms do not exhibit plateau at $P/P_o \rightarrow 1.0$ but they asymptotically approach the *y*-axis. These features correspond relatively well to Type IVB isotherm.

The specific surface area calculated by the BET method is 608.85 m^2/g, which is relatively high compared with sample S1 (155.09 m^2/g). The pore size distribution (Fig. 4.59(b)) shows that P1 has a wide range of pore size distribution.

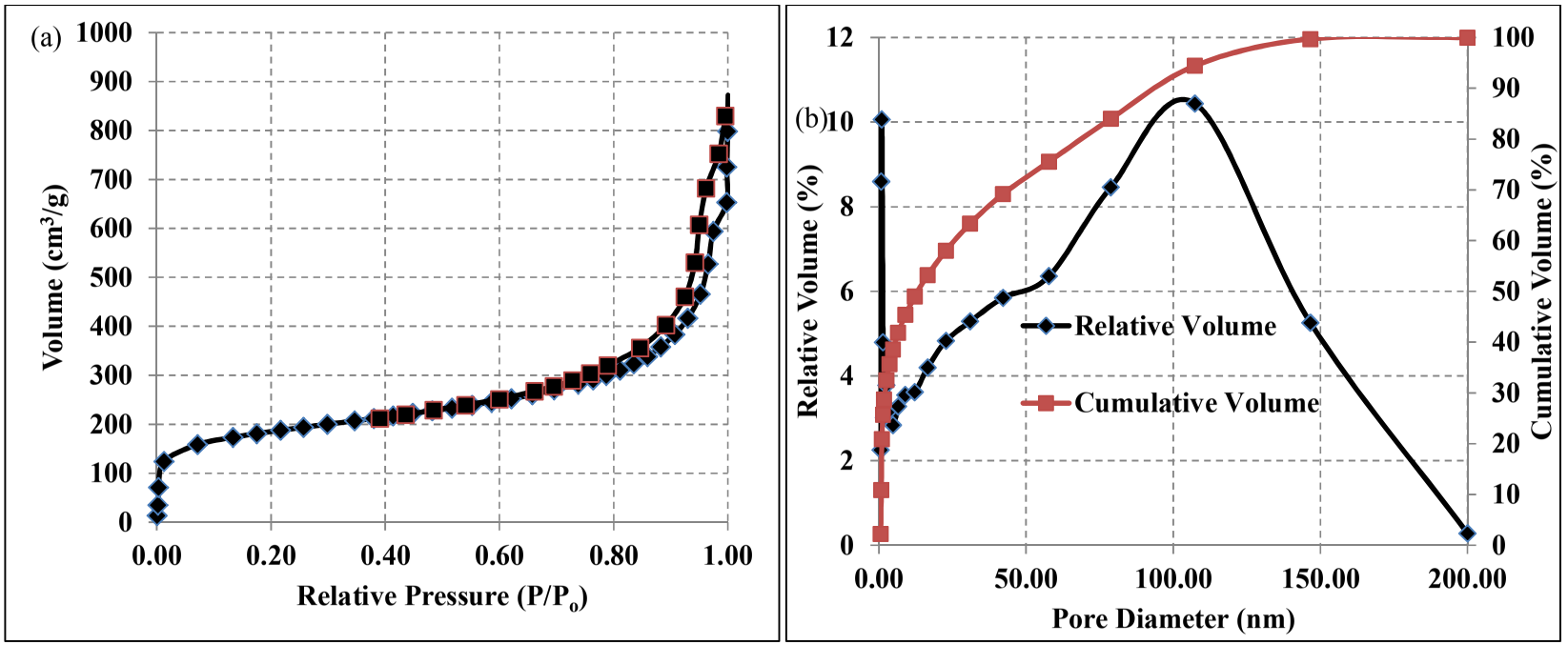

Figure 4.59:
(a) N_2-gas Adsorption Desorption Isotherm and (b) Pore Size Distribution of P1

4.3.2 Formation of Maghemite-Silica Particulate Nanocomposites

To form maghemite-silica particulate nanocomposites, modifications need to be made to achieve this purpose. Firstly, the whole process should be run in ultrasonic bath. Ultrasonic bath is used to increase the hydrolysis and condensation rates of the sol-gel process. Hydrolysis and condensation rates directly influence the final particle size (Wang et al., 2010). Monodisperse particles can be obtained as long as the hydrolyzed monomers react much more quickly than they are produced.

Secondly, the pH level needs to be controlled to ensure the formation of silica particulate matrix. Following this, ethanol was used instead of TPA to form this matrix in order to increase the surface area of the produced nanocomposites.

Four primary samples were prepared by varying the pH level of the solution during the addition of maghemite nanoparticles. This was to ensure that the matrix formed is in silica particulate form. The Fe_2O_3/SiO_2 ratio used was the same as in sample MNP025. The compositions and pH values of the samples are listed in Table 4.20. The results were analyzed and the final pH level was determined before proceeding to the following step.

Table 4.20:
Composition of Samples

Sample	pH Level	Maghemite Nanoparticles (g)	TEOS (g)	H_2O (g)	Fe_2O_3/SiO_2
P2.5	2.5	0.25	2.5	1.5	0.35
P5.0	5.0	0.25	2.5	1.5	0.35
P7.0	7.0	0.25	2.5	1.5	0.35
P10.0	10.0	0.25	2.5	1.5	0.35

4.3.2.1 Effect of pH Variation

NH_4OH solution was used to control the pH level for this stage. The addition of NH_4OH not only accelerates the hydrolysis and condensation of TEOS, but supplies the OH^- adhering on the particle, which can stabilize the suspension by static repulsion against Van der Waals attractive force (Wang et al., 2010). Thus, coagulation may be formed if the concentration of NH_4OH is too high, and the reaction requires a long time or silica particles cannot be obtained if the concentration of NH_4OH is too low. An appropriate NH_4OH concentration should be chosen in order to solve this problem.

4.3.2.1.1 Thermal Properties

Figure 4.60 shows the TGA curves of samples labelled "P". The curves exhibit similar behaviour. A weight loss of around 19 % is observed upon heating over the range of room temperature to 1000 ^oC, as shown in Table 4.21. Only one weight loss is observed at around 150 ^oC, which is mainly due to the removal of solvent and dehydration process.

Table 4.21:
Percentage Weight Loss of Samples

Sample	Weight loss (%)
P2.5	18.83
P5.0	19.48
P7.0	19.77
P10.0	18.44

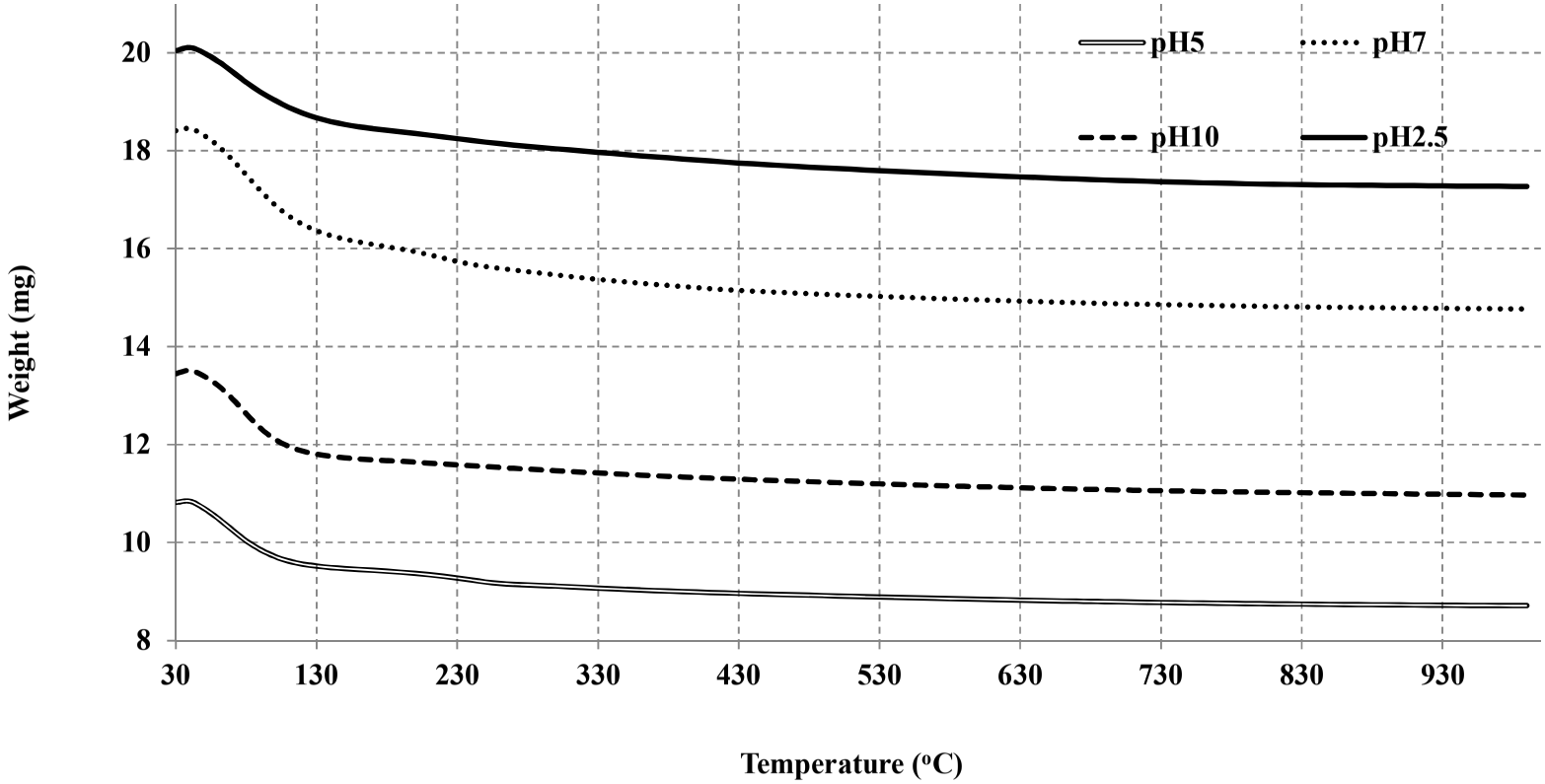

Figure 4.60:
TGA Curves for Samples

4.3.2.1.2 Phase and Crystal Structure Analysis

The XRD patterns of the as-prepared maghemite-silica particulate nanocomposites are shown in Fig. 4.61 (please refer to Appendix 2-5 for the individual graph). For sample P2.5, no maghemite nanoparticle peaks can be observed. This may be due to the limit of the dissolution of maghemite nanoparticles or the phase transformation of nanoparticle under the low pH value. Maghemite is quite soluble in low pH and even more difficult to detect by XRD. For samples P5 and P7, an extra peak is observed at 28 ^{o}, which corresponds to the silica crystallite phase. Additionally, the maghemite peaks are sharp, indicating that the size is larger than 10 nm. For sample P10, the pattern is similar to the maghemite-silica xerogel nanocomposite discussed in Section 4.2. The XRD diffraction patterns clearly show the reflection corresponding to maghemite nanoparticles and a visible wide band at 2θ from 20 ^{o} to 35 ^{o}, which are characteristics of the amorphous phase of the silica gel. Additionally, the patterns exhibit the presence of only maghemite and SiO_2 amorphous phase, which indicates that there are no chemical reactions between the silica particulate matrix and maghemite nanoparticles to form other compounds.

From the patterns, the corresponding peaks observed are located at about 2θ = 30 ^{o}, 35 ^{o}, 43 ^{o}, 57 ^{o} and 63 ^{o}. These peaks match well with the ICDD PDF Card Number 39-1346. This proves that no phase transformation occurs during the encapsulation process. The broadening of the peak for sample P 10 also reflects that the sample's particle size is within the nanometre size range.

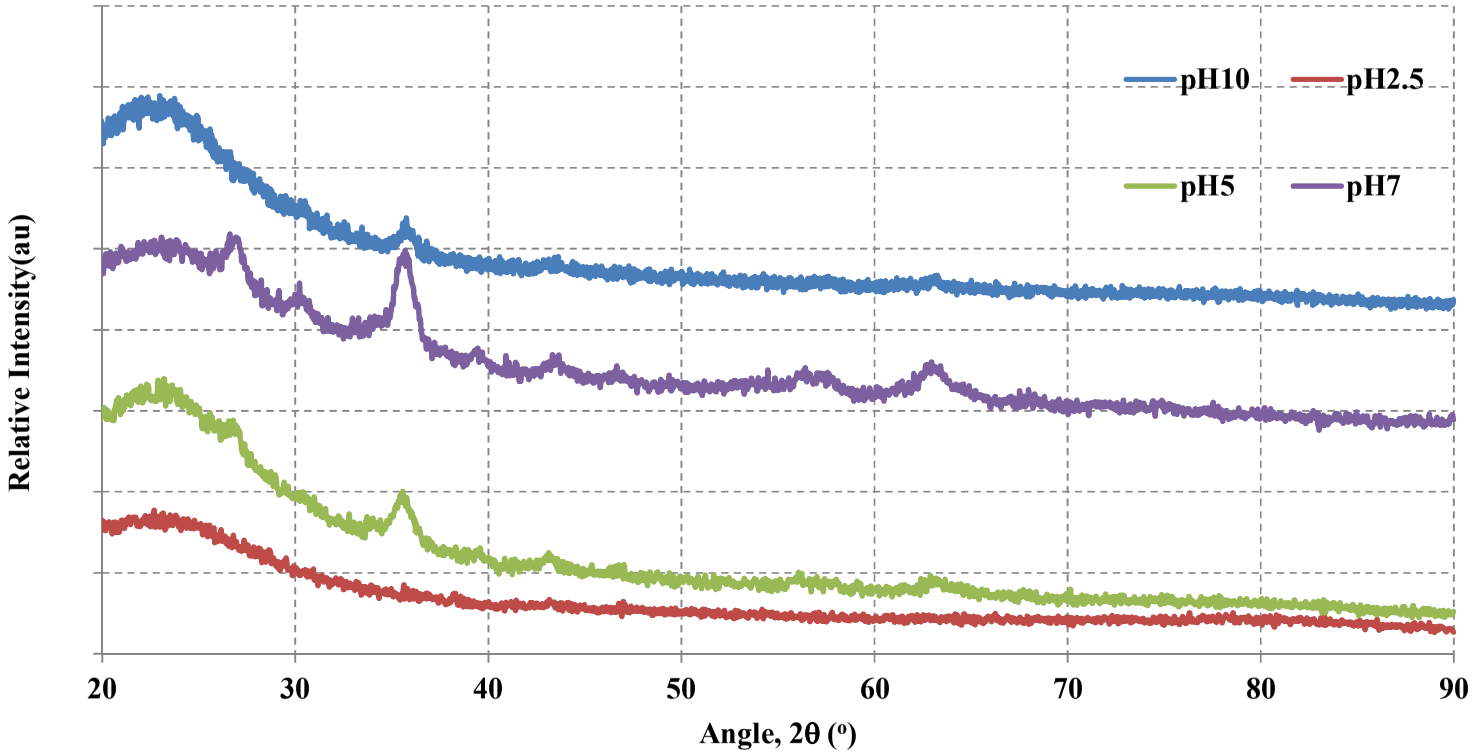

Figure 4.61:
XRD Curves for Samples

4.3.2.1.3 Morphology and Physical Size Analysis

In this study, only 3-dimensional FESEM was performed and are shown in Figs. 4.62 – 4.65. For sample P2.5, the surface morphology observed is a network of solid material with pores, which is the same as sample S1. Phase transformation is observed when the pH value changes to 5, which seems to be a coagulation of very small particles. Less coagulated particles are observed with an increase in NH_4OH, as shown in sample P7 (Fig. 4.64). Sample P7 shows an irregular surface morphology, in which two types of particles are observed. The first type is composed of botryoidally aggregates of spherical particles, whereas the second type has a continuous gel appearance, which is a gel network with pores. This surface morphology is known as a bi-modal final particle size distribution. Finally, monodisperse spherical particles are achieved for the sample having a pH value of 10. This phenomenon has never been reported in the preparation of maghemite-silica nanocomposites in the past.

This shows that the addition of different amounts of NH_4OH directly influences the final particle size and size distribution. Monodisperse particles can be obtained as long as the hydrolyzed monomers react much more quickly than they are produced. Otherwise, particles with a bi-modal distribution and polydispersity will be achieved.

From the XRD, TEM and FESEM results, maghemite-silica particulate nanocomposites can only be produced if the pH level is adjusted to 10. This condition is used for the following samples produced from this stage.

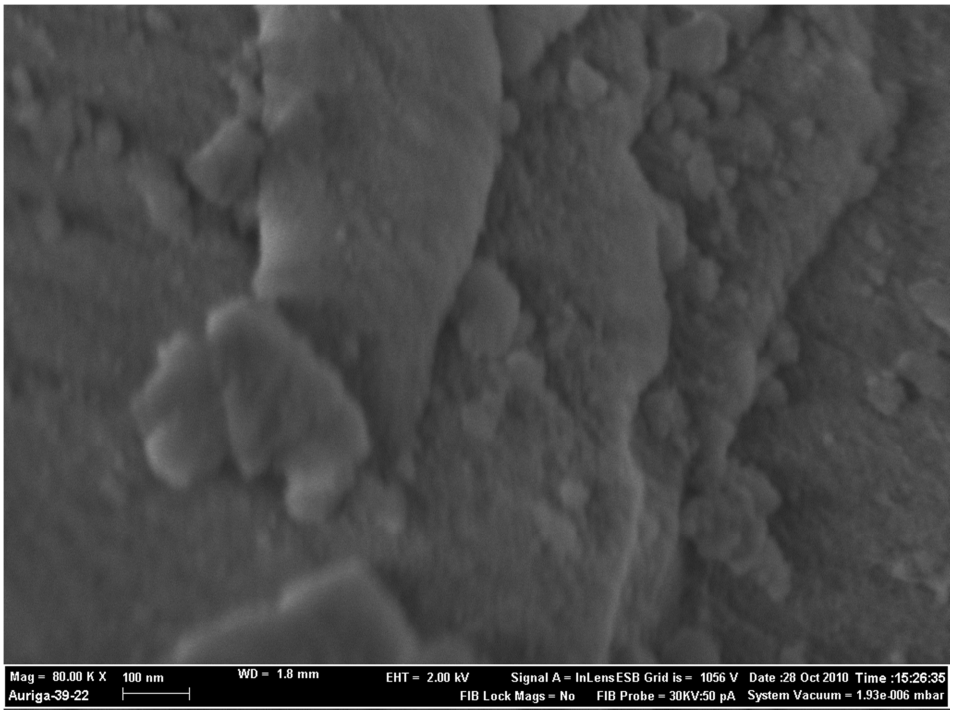

Figure 4.62:
FESEM Micrograph of Sample P2.5

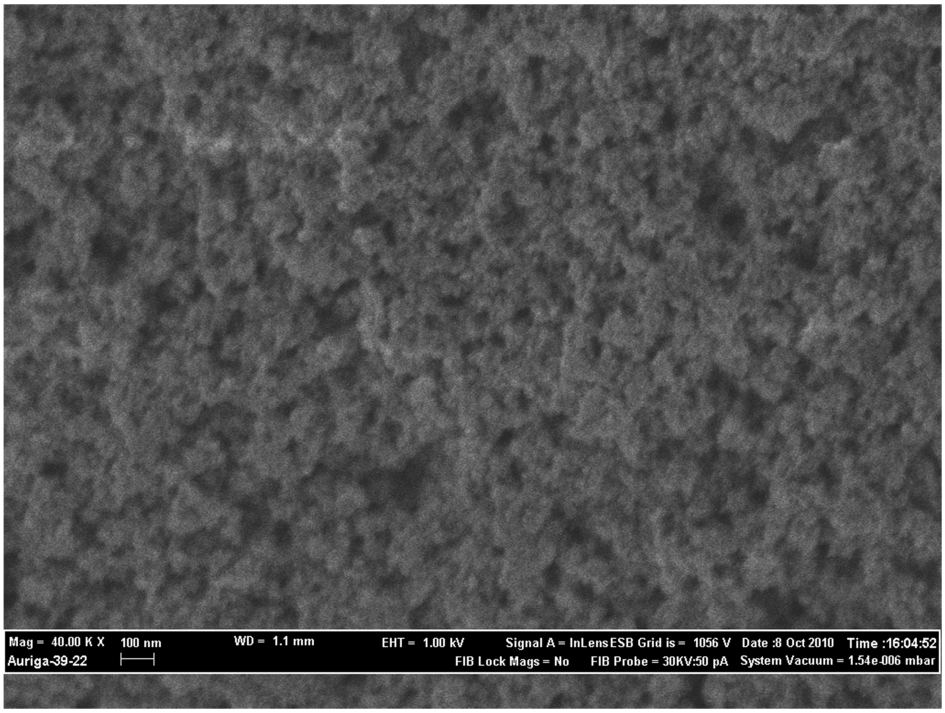

Figure 4.63:
FESEM Micrograph of Sample P 5

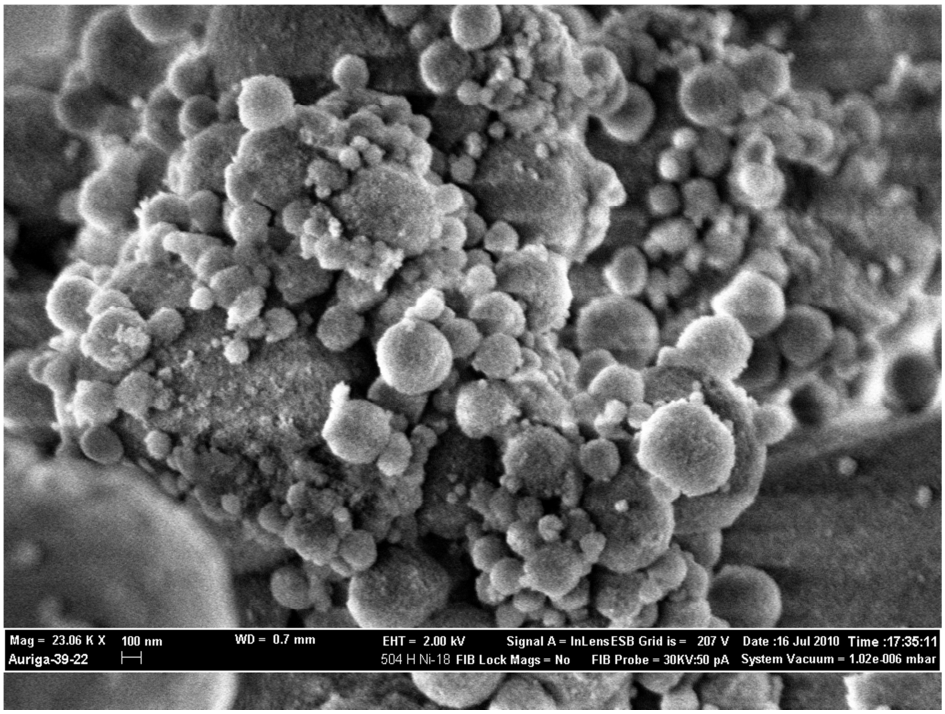

Figure 4.64:
FESEM Micrograph of Sample P7

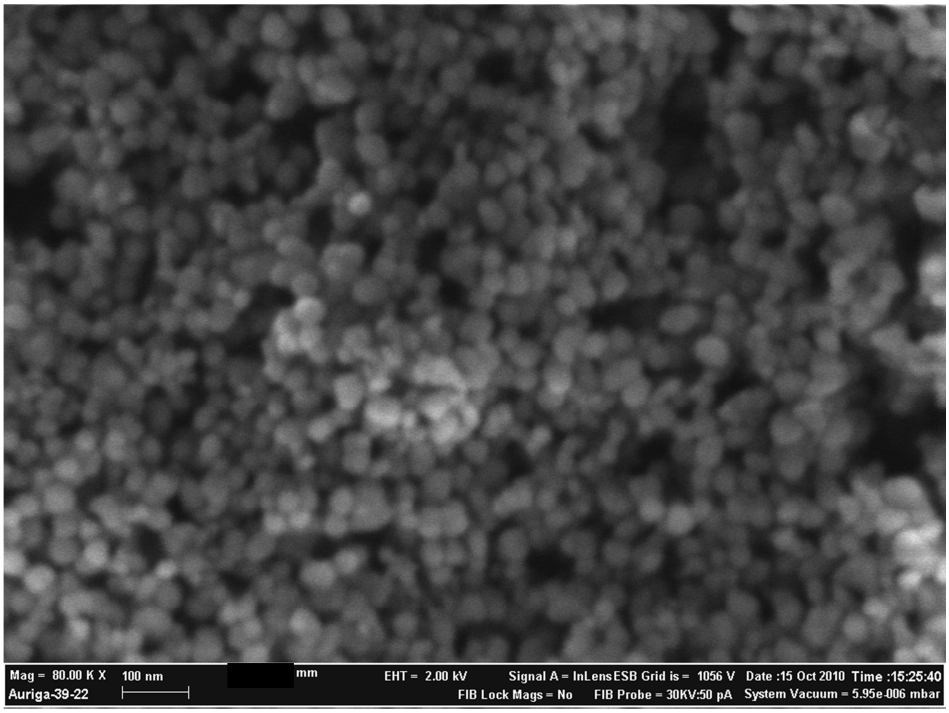

Figure 4.65:
FESEM Micrograph of Sample P10

4.3.2.2 Effect of the Amount of Maghemite Nanoparticles in Nanocomposite

Following the determination of pH level for formation of particulate SiO_2, three samples with different Fe_2O_3/SiO_2 ratios were prepared from the modified new sol-gel method. The steps for the formation of maghemite-silica particulate nanocomposites have been described in Section 3.1.1.3. The compositions of the samples are listed below:

Table 4.22:
Composition of Samples

Sample	Maghemite Nanoparticles (g)	TEOS (g)	H_2O (g)	Fe_2O_3/SiO_2
MNP025	0.25	2.5	1.5	0.35
MNP050	0.50	2.5	1.5	0.70
MNP100	1.00	2.5	1.5	1.39

4.3.2.2.1 Phase and Crystal Structure Analysis

Figure 4.66 shows the XRD diffraction patterns for as-prepared nanocomposites. The XRD diffraction patterns for samples MNP025, MNP050 and MNP100 clearly show the reflection corresponding to maghemite nanoparticles and a visible broad peak at 2θ from 20 ^{o} to 35 ^{o} which are characteristics of the amorphous phase of the silica gel. The patterns also exhibit the presence of only maghemite and SiO_2 amorphous phase, which indicates that there are no chemical reactions between the silica particulate gel and maghemite nanoparticles to form other compounds. These results are the same as those observed for sample MN in Section 4.2.

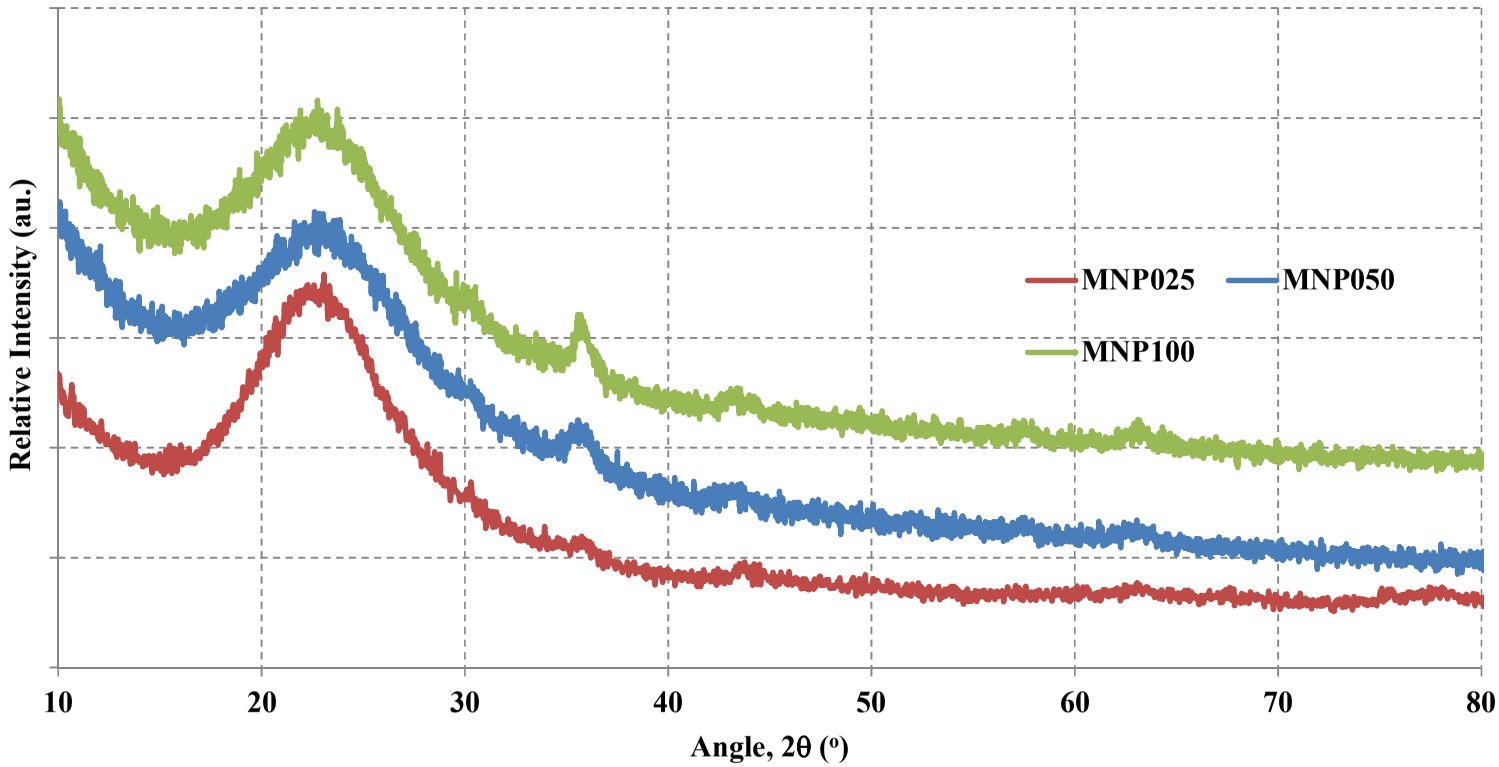

Figure 4.66:
XRD Curves for Samples

The broadening of the (311), (511) and (440) reflections increase in the order of MNP100, MNP050 and MNP025. The observed trend suggests a possible decrease in crystallite size when the concentration of maghemite nanoparticles is decreased or in other words, with decreasing weight ratio of Fe_2O_3/SiO_2. The broadening and low intensities of the peaks indicate that the crystallite sizes of the samples are within the nanometre scale for all samples. The average crystallite size and lattice parameter of the samples were calculated from the major peaks using Equation 4.1 and the details are shown in Tables 4.23 and 4.24.

Table 4.23:
Lattice Parameter for Samples

Sample	2θ (°)	d-spacing (Å)	Miller Indices (hkl)	Lattice Constant (Å)
MNP025	35.6662	2.514	311	8.34
	62.9862	1.4738	440	8.34
			Average	**8.34**
MNP050	35.7675	2.5071	311	8.32
	63.5105	1.4629	440	8.28
			Average	**8.30**
MNP100	35.7382	2.5091	311	8.32
	63.0456	1.4726	440	8.33
			Average	**8.33**

The calculated crystallite sizes are 4.07 nm, 4.82 nm and 5.45 nm for samples MNP025, MNP050 and MNP100, respectively. Comparison of the average crystallite size between samples M10 and MNP shows that the encapsulated maghemite nanoparticles have a smaller average crystallite size. This could be due to a slight dissolution of maghemite nanoparticles in the silica particulate matrix. These results agree well with the broadening trend observed previously. The crystallite sizes are nearly the same when compared with sample MN.

Table 4.24:
Crystallite Size for Samples

Sample	2θ (°)	θ (rad)	cos θ	$W_{b(sample)}$	$W_{s(standard)}$	Crystallite Size (nm)
MNP025	35.6662	0.31129	0.95194	1.4983	0.0531	5.06
	62.9862	0.54973	0.85267	2.1975	0.1618	3.09
					Average	**4.07**
MNP050	35.7675	0.31217	0.95167	1.0261	0.0531	7.39
	63.5105	0.55431	0.85027	2.9999	0.1618	2.26
					Average	**4.82**
MNP100	35.7382	0.31192	0.95175	1.1379	0.0531	6.66
	63.0456	0.55025	0.85239	1.6042	0.1618	4.25
					Average	**5.45**

4.3.2.2.2 Morphology and Physical Size Analysis

Figs. 4.67 (a) – 4.69 (a) show the TEM micrographs for the samples and Fig. 4.70 shows the FESEM micrographs. Capturing nice images is particularly difficult using FESEM and TEM as the silica particulate nanocomposites are very sensitive to the electron beams, which transforms to gel in a few seconds. Only coagulation of gel can be observed after a few seconds. However, several images were taken to show the distribution of maghemite nanoparticles in silica particulate matrix. The TEM micrographs reveal a homogeneous dispersion of isolated maghemite nanoparticles over the silica particulate matrix in all samples. The FESEM micrographs further confirm that the matrix is still in silica particulate form.

The physical size distribution histograms for TEM are shown in Figs. 4.67(b) – 4.69(b). The calculated physical mean diameter decreases constantly from sample MNP100 to MNP025, confirming that the peak broadening observed in the XRD spectra is due to the reduction in maghemite nanoparticle size. The measured physical

mean diameters are 4.48 nm, 4.77 nm and 5.22 nm for samples MNP025, MNP050 and MNP100, respectively. In addition, the distribution histogram for sample MNP025 is more skewed toward lower size compared to sample MNP050 and MNP100.

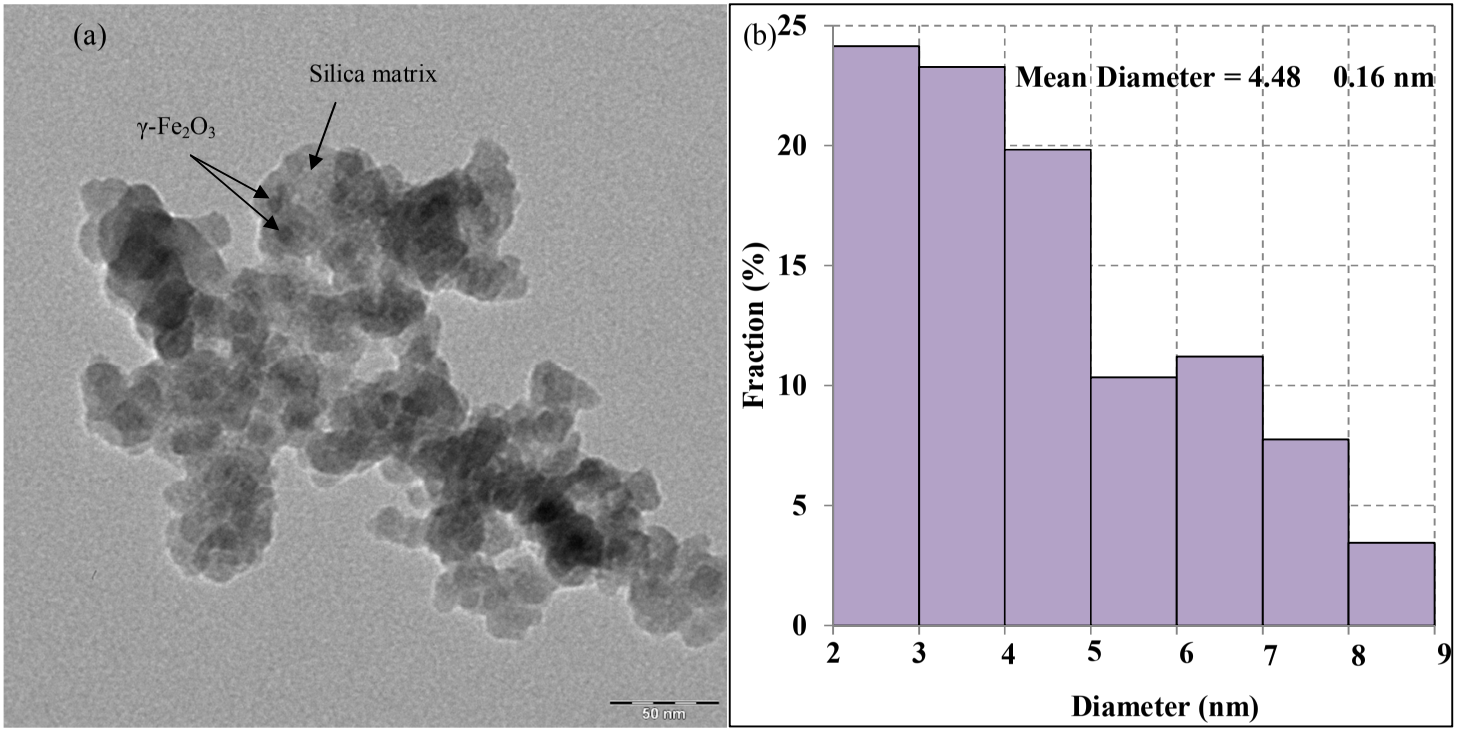

Figure 4.67:
(a) TEM Micrograph and (b) Size Distribution Histogram of MNP025

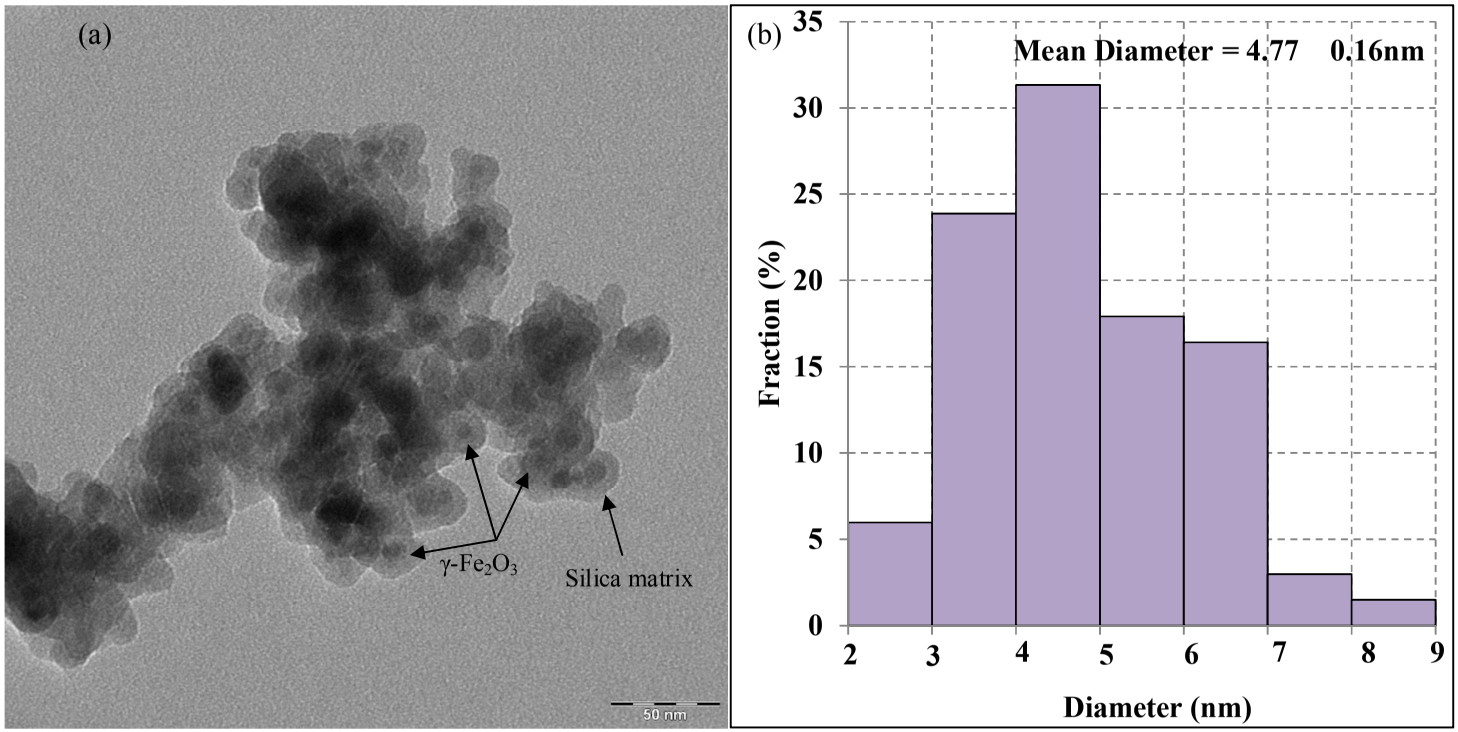

Figure 4.68:
(a) TEM Micrograph and (b) Size Distribution Histogram of MNP050

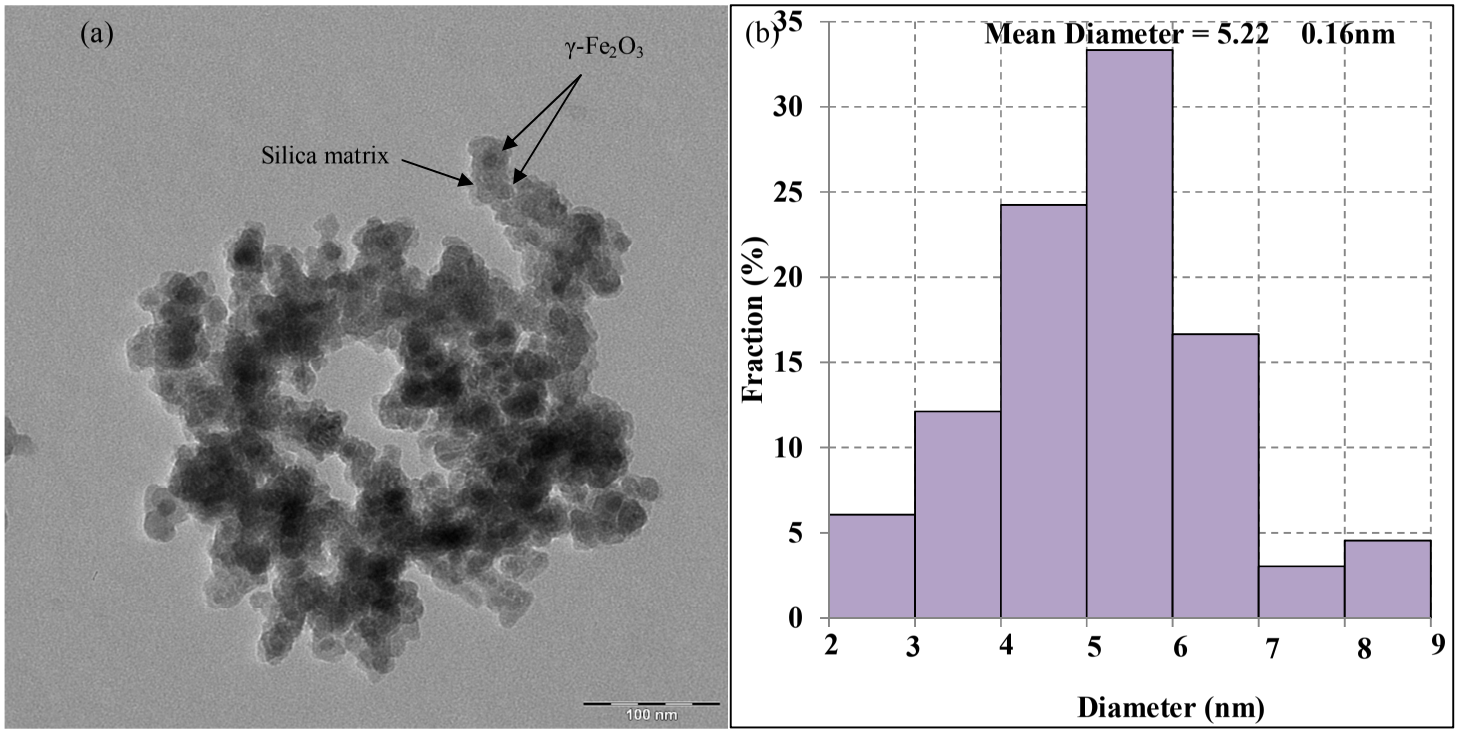

Figure 4.69:
(a) TEM Micrograph and (b) Size Distribution Histogram of MNP100

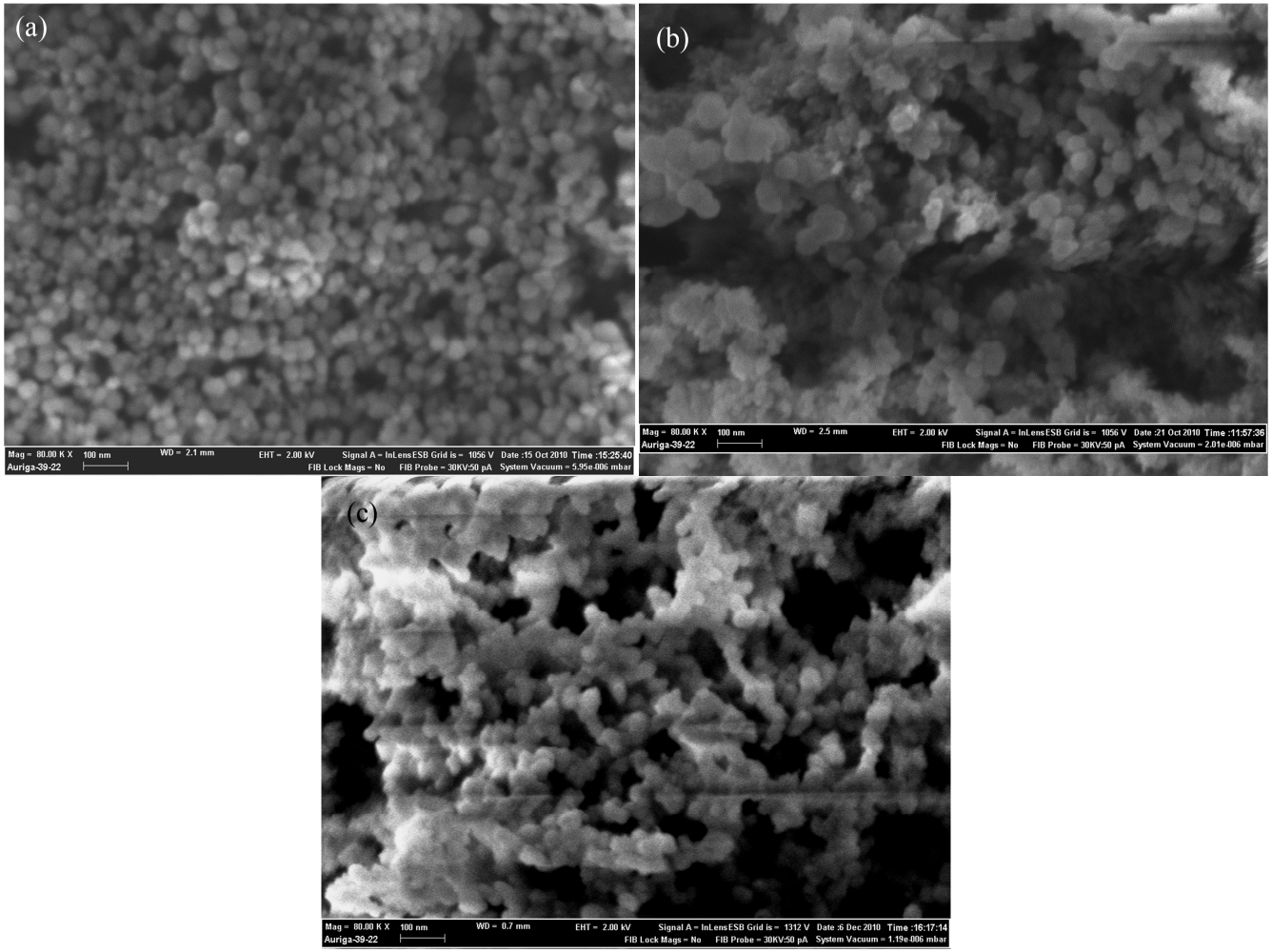

Figure 4.70:
FESEM Micrographs for (a) MNP025, (b) MNP050 and (c) MNP100

HRTEM and EELS were carried out for sample MNP025, as shown in Fig. 4.71. From the HRTEM micrograph, it is clearly seen that the embedded particle (core) is with the presence of atomic interspaces, which indicates that it is in the crystalline form. The matrix observed is a non-crystalline material because no lattice is present from the observation. The EELS result obtained from the cores clearly shows the presence of Fe-L_3 signals at around 720 eV, which proves that the embedded particles are iron-based compounds.

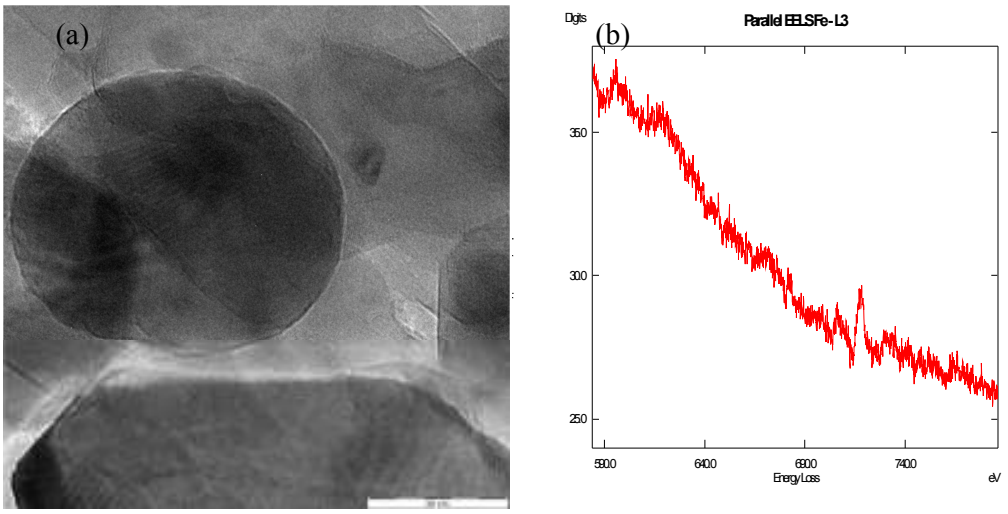

Figure 4.71:
(a) HRTEM Micrograph and (b) EELS of MNP025

4.3.2.2.3 Surface Area Analysis

The surface areas of the MNP samples were studied by the N_2-gas adsorption desorption method. The samples exhibit very similar isotherms. The unique features are (i) very high adsorption at $P/P_o \rightarrow 0$, which indicates that a high volume of micropores is present for all samples; (ii) a relatively moderate increase in the adsorbed amount of N_2 within the P/P_o range of 0-0.95; (iii) a sharp increase in adsorbed N_2

within the P/P_o range of 0.95-1.0; (iv) the hysteresis loop is rather small and horizontally oriented; (v) the isotherms do not exhibit plateau at $P/P_o \rightarrow 1.0$ but they asymptotically approach the *y*-axis. These features correspond relatively well to the Type IV isotherm. The specific surface area is calculated from the BET method and is shown in Table 4.25.

Table 4.25:
Specific Surface Area (BET), Pore Specific Volume of Samples

Sample	Specific Surface Area (m^2/g)	Pore Specific Volume (cm^3/g)
MNP025	369.91	0.2205
MNP050	370.97	0.2164
MNP100	382.90	0.2244

The result shows that increasing the amount of maghemite nanoparticles leads to a larger surface area for the nanocomposites. However, the difference is not significant. This shows that the particles do not fill the pores between the silica spherical particles. Rather, the maghemite particles are embedded within the silica particles. The results show good agreement with TEM observations.

Referring to Table 4.17, the surface area obtained for maghemite-silica xerogel nanocomposites (MNs) are much lower compared to MNPs, whereby the specific surface areas are only within the range of 15 - 39 m^2/g. Once the silica matrix changes to silica particulate form, the surface area increases tremendously.

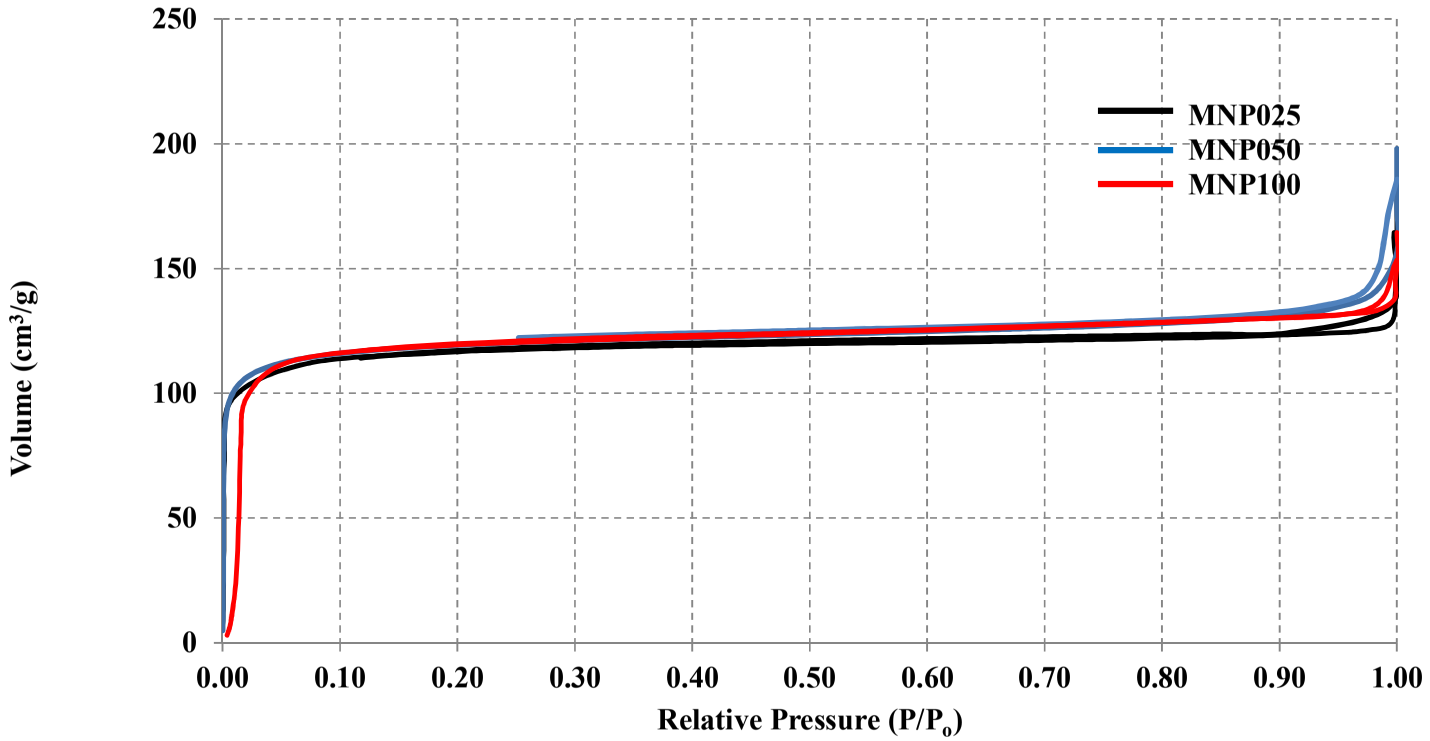

Figure 4.72:
N_2-gas Adsorption Desorption Isotherm for Samples

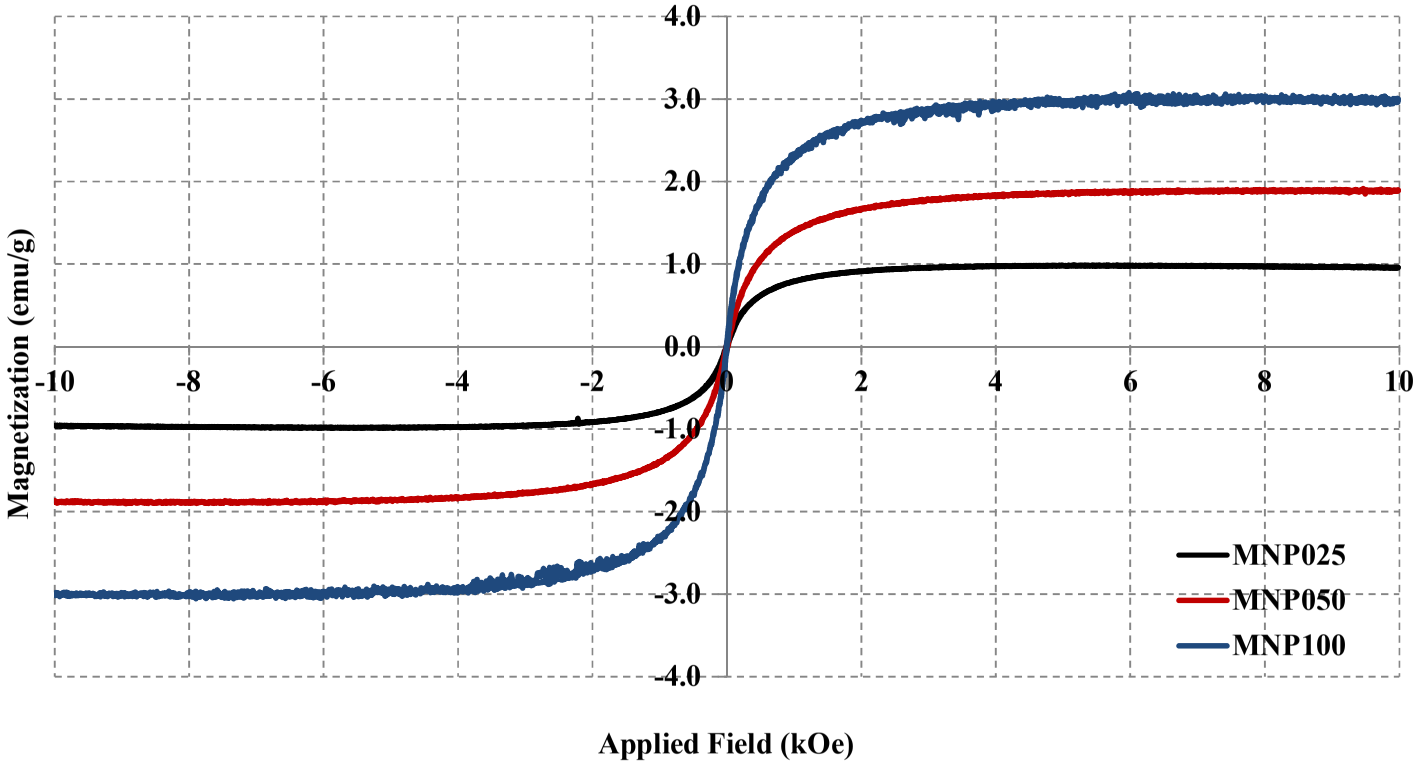

Figure 4.73:
Magnetization Curves for Samples

4.3.2.2.4 Magnetization Analysis

Fig. 4.73 shows the magnetization curves for all MNP samples. The shapes of the magnetization curves for nanocomposites are very similar to the initial sample. Superparamagnetic behaviour is exhibited by all samples, indicating that the size of the maghemite nanoparticles is always within the nanometre range. The increase in iron content gives rise to a small particle growth.

The observed decrease in magnetization values compared with sample M10 also reflects the standard practice of normalizing the magnetization by sample mass. For nanocomposites, there is less magnetic material per unit weight, and the magnetization readings are divided by the substantial mass of silica. As a result, both the saturation and remanent magnetization values decrease upon the embedment process. Attempts to quantify the percentage of magnetic material in order to normalize by mass of magnetic material have been unsuccessful, as methods to dissolve the silica matrix also destroy or alter the maghemite nanoparticles (Vestal and Zhang, 2003). The value of M_r/M_s does not change significantly from the as-synthesized maghemite nanoparticles and maghemite nanocomposites. The consistency in the shape of the hysteresis curves further confirms that the decrease in magnetization is primarily due to a lower amount of magnetic material per mass and a slight dissolution of maghemite nanoparticles.

Comparison of sample MN (Table 4.18) and sample MNP (Table 4.26) shows that the magnetization at 10 kOe applied field (M_{10kOe}) and the magnetic size for sample MNP are slightly lower. This may be due to the possibility that most maghemite nanoparticles are embedded within the silica particulate matrix and not on the surface or the pores of the matrix.

Table 4.26:
Magnetic Size for Samples

Sample	Magnetization Saturation (emu/g)	dM/dH	Magnetic Size (nm)
M10	9.53	0.02205	5.92
MNP025	0.96	0.00214	2.74
MNP050	1.90	0.00343	3.21
MNP100	3.00	0.00668	4.00

4.3.3 Summary for Stage III

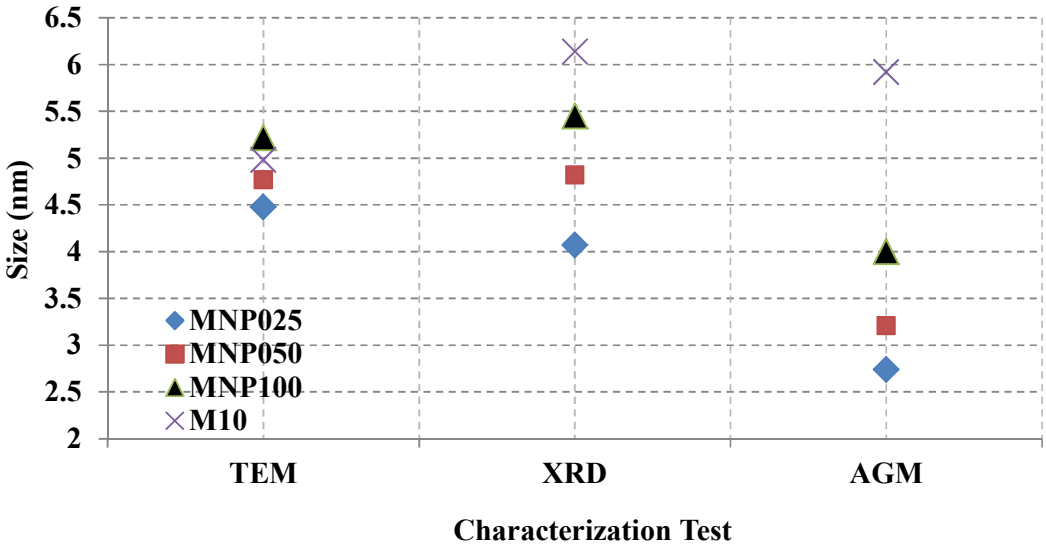

Figure 4.74:
Size Comparison Graphs for Samples

Table 4.27:
Measured Crystallite, Physical, Magnetic Size, Lattice Constant and Surface Area of Samples

Sample	XRD Crystallite Size (nm)	TEM Physical Size (nm)	Lattice Constant (nm)	AGM Magnetic Size (nm)	BET Surface Area (m^2/g)
MNP025	4.07	4.48	8.34	2.74	369.91
MNP050	4.82	4.77	8.30	3.21	370.97
MNP100	5.45	5.22	8.33	4.00	382.90

Fig. 4.74 and Table 4.27 show the summarized results for stage III. A few conclusions can be made for this stage. Firstly, the size of the embedded maghemite nanoparticles increases with increasing Fe_2O_3/SiO_2 ratios. The results also show that the calculated sizes are smaller than the as-synthesized maghemite nanoparticles (M10). This may be due to a slight dissolution of maghemite nanoparticles in silica particulate form matrix. The particulate form of matrix keeps the particles isolated and hinders their coalescence and growth, which stabilizes the as-synthesized maghemite nanoparticles.

High surface area is crucial for nanoparticles especially for applications due to the increase of the sensitivity. In stage III, a very high surface area is attained for the produced nanocomposites, compared with those of stage II. This enhances the sensitivity and the reactivity of the nanocomposites. The modified sol-gel process gives the following advantages: 1) nanocomposites with high surface areas, 2) good control of maghemite nanoparticles, 3) no surfactants are required and 4) monodispersed nanoparticles are achieved and therefore, the aggregation and agglomeration problem is solved. These nanocomposites would be very useful for bio-applications such as MRI contract agent.

CHAPTER 5: CONCLUSIONS

Maghemite nanoparticles were produced successfully using Massart's procedure. This matched the first objective of my study. In this research, the effects of varying the $FeCl_2$ concentration on the physical properties and magnetic size were studied. The XRD patterns of the samples showed peak broadening effect, which indicates that the crystallite sizes of the particle were in the nanometre size range. The calculated crystallite sizes were 6.79nm, 6.56nm, 6.14nm, 6.72nm and 7.24nm for $FeCl_2$ concentrations of 0.1M (M01), 0.8M (M08), 1.0M (M10), 1.2M (M12) and 1.5M (M15), respectively. The magnetization curves which showed no hysteresis, indicates that the particles were superparamagnetic. The least upper bound of the 'magnetic' sizes calculated were 7.53nm, 6.29nm, 5.92nm, 6.41nm and 8.04nm while the physical sizes measured from TEM micrographs were 5.97nm, 6.02nm, 4.98nm, 5.98nm and 5.35nm for samples M01, M08, M10, M12 and M15, respectively. The TEM micrographs showed that the maghemite nanoparticles were roughly spherical in shape. All the samples showed lower saturation magnetization values at 10kOe applied field compared to bulk. From the results, it can be concluded that the product obtained through Massart's procedure was highly dependent on the concentration of the precursor and decreasing the concentration of iron salt does not necessarily reduce the size of maghemite nanoparticles.

Maghemite-silica xerogel nanocomposites were produced successfully using sol-gel technique, which is in line to the second objective of this study. By encapsulating maghemite nanoparticles within the silica xerogel matrix, the crystallite sizes of the encapsulated maghemite nanoparticles were finer, indicating that a slight dissolution of particles occurred during the encapsulation process. The sizes of the maghemite nanoparticles within the silica matrix increased with increasing weight ratio of

Fe_2O_3/SiO_2. The nanocomposites showed superparamagnetic behaviour with values of magnetization at ±10kOe applied field within the range of 1.79emu/g to 9.53emu/g, depending on the Fe_2O_3/ SiO_2 ratio. The magnetization values at 10kOe applied magnetic field increased with increasing amount of maghemite in the nanocomposites. The N_2-gas adsorption-desorption hysteresis loops of maghemite-silica xerogel nanocomposites became smaller with increasing maghemite nanoparticles within silica xerogel matrix. This indicates that the amount of pores was reduced. This claim was further proven by observing the average pore width. The hysteresis loops showed that mini and micro pores of SiO_2 were filled. The FESEM micrographs clearly showed that most of the maghemite nanoparticles were embedded into the pores of the silica matrix. The EDS and TEM results revealed that the maghemite nanoparticles were distributed evenly within the matrix. This indicates that the silica matrix functions as a physical barrier to prevent the agglomeration and aggregation of maghemite nanoparticles.

In stage III, a very high surface area was attained for the produced nanocomposites, compared with those of stage II. This enhances the sensitivity and reactivity of the nanocomposites. This unique property matched the third objective very well. The modified sol-gel process offers the following advantages: 1) nanocomposites with high surface areas, 2) good control of maghemite nanoparticles, 3) no surfactants are required, and 4) monodisperse nanoparticles are achieved and therefore, the aggregation and agglomeration problem is solved. These nanocomposites can be applied into the bio-applications.

CHAPTER 6: PROBLEMS FACED

Some considerations can be suggested to further investigate these unique maghemite nanoparticles and their composites:

1. In this study, Massart's procedure was used to synthesize maghemite nanoparticles. More investigations can be carried out such as thermal conductivity and zeta potential to study on the stability of the as-synthesized maghemite nanoparticles.
2. More details studies on the magnetic properties need to be carried out based on the preparation conditions of Massart's procedure.
3. Studies are required to determine the effects of gelation time, surface/volume on silica matrix and the nanocomposites produced.
4. Further work should be focused on the use of the synthesized maghemite nanoparticles and nanocomposites in actual bio-applications such as MRI contract agent.

REFERENCES

Ang B.C., & Yaacob I.I. (2006). Synthesis and characterization of iron oxides nanoparticles. *Key Engineering Materials, 306-308,* 1115-1120.

Ang B.C., & Yaacob I.I. (2007). Synthesis and characterization of magnetic iron oxide nanoparticles via w/o microemulsion and Massart's procedure. *Journal of Materials Processing Technology, 191 (1-3)*, 235.

Ang B. C., & Yaacob I.I. (2010). Preparation of maghemite-silica nanocomposite using sol-gel technique. *Advanced Materials Research 97-101*, 2140-2143.

Allwood D.A., Xiong G, Cooke M.D., Faulkner C.C., Atkinson D., & Vernier N. (2002). Submicrometer ferromagnetic NOT gate and shift register. *Science, 296,* 2003-2006.

Aslam M., Fu L., Li S., & Vinayak P. Dravid (2005). Silica encapsulation and magnetic properties of FePt nanoparticles. *Journal of Colloid and Interface Science, 290***,** 444-449.

Asti G., Solzi M., & Gerber R. (1994). *Applied Magnetism*. The Nertherlands: Kluwer Academic Publishers, pp. 370.

Ayyub P., Multani M., Barma M., Polkar V. R., & Vijayaraghavan R. (1988). Size-induced structural phase transitions and hyperfine properties of microcrystalline Fe_2O_3. *J. Phys. C: Solid State Phys., 21*, 2229-2245.

Barrado E., Rodriguez J.A., Prieto F., & Medina J. (2005). Characterization of iron oxides embedded in silica gel obtained by two different methods. *J. of Non Crys Solids, 351*, 906-914.

Bate, G. (1999). Magnetic recording materials since 1975. *J. Magn. Magn. Mater., 100*, 413-424.

Bee A., Massart R., & Neveu S. (1995). Synthesis of very fine maghemite particles. *Journal of Magn. Material, 149***,** 6-9.

Bhatnagar S.P., & Rosensweig R.E. (1995). Introduction to the magnetic fluids bibliography. *J. Magn. Magn. Mater., 149*, 198.

Binh V.T., Purcell S.T., Semet V., & Feschet F. (1998). Nanotips and nanomagnetism. *Applied Surface Science 130-132*, 803-814.

Borelli, N.F., Morse, D.L., & Schreurs J.W.H. (1983) Magnetic properties of iron oxide photolytically produced from $Fe(CO)_5$ impregnated porous glass. *J. Appl. Phys., 54*, 3344 .

Boudeulle M., Batis-Landoulsi H., Leclercq Ch., & Vergnon P. (1983). Structure of γ-Fe_2O_3 microcrystals: Vacancy distribution and superstructure. *Journal of Solid State Chemistry, 48(1),* 21-32.

Braun H. and Gallagher K.J. (1972). β- Fe_2O_3: a new structural form of iron (III) oxide. *Nature Physical Science, 240,* 13-14.

Brinker C.J. & Scherer G.W. (1990). *Sol-Gel Science: The Physical and Chemistry of Sol-Gel Processing.* United Kingdom: Academic Press Limited.

Bruce M.M. (1991). *Hitchhiker's Guide to Magnetism.* Environmental Magnetism Workshop, Institute for Rock Magnetism.

Brunauer S, Emmett P. H. & Teller E. (1938). Adsorption of gases in multimolecular layers. *Journal of the American Chemical Society, 60,* 309-19.

Cannas C., Casu M., Musinu A., & Piccaluga G. (2005). Si CPMAS NMR and near-IR study of sol-gel microporous silica with tunable surface area. *Journal of Non-crystalline solids, 351,* 3476-3482.

Cannas C., Concas G., Falqui A., Musinu A., Spano G. and Piccaluga G. (2001). Investigation of the precursor of gamma Fe_2O_3 in Fe_2O_3/ SiO_2 nanocomposites obtained through sol-gel. *Journal of Non-Crystalline Solids, 286,* 64-73.

Cannas C., Concas G., Gatteschi D., Falqui A., Musinu A., Piccaluga G., Sangregorio C., & Spano G. (2001). Superparamagnetic behaviour of γ-Fe2O3 nanoparticles dispersed in a silica matrix. Phys. Chem. Chem. Phys. 3, 832-838.

Cannas C., Gatteschi D., Musinu A., Piccaluga G., & Sangregorio C. (1998). Structural and magnetic properties of Fe_2O_3 nanoparticles dispersed over a silica matrix. *J. Phys. Chem B, 102,* 7721-7726.

Casas L1., Roig A., Rodriguez E., Molins E., Tejada J. and Sort J. (2001). Silica aerogel-iron oxide nanocomposites: structural and magnetic properties. *J. of non-crystalline solids, 285,* 37-43.

Callister W.D. (2003). *Materials Science and Engineering* (6th ed.). United State of America: John Willey and Sons, Inc.

Cauqui M.A., & Rodriguez-Izquierdo J.M. (1992). Application of sol-gel methods to catalys preparation. *J. Non-crys. Solids, 724*, 147-148.

Coey J. (1971). Noncollinear spin arrangement in ultrafine ferromagnetic crystallites. *Physics Review Letter 27*, 1140-1143.

Cornell R.M. and Schwertmann U. (1996). *The Iron Oxides: Structure, Properties, Reactions, Occurrence and Uses* (1st ed.). Weinheim Germany: VCH Verlagsgesellschaft.

Crangle J. (1977). *The Magnetic Properties of Solids*. London: Edward Arnold Ltd., 128-129

Cullity B.D. (1972). Introduction to Magnetic Materials. Massachusetts: Addison-Wesley Publishing.

Daughton J.M. (1992). Magnetoresistive memory technology. *Thin solid Films, 216*, 162-168.

Dinesen A.R., Pedersen C.T., & Bender K. C. (2001). The thermal conversion of lepidocrocite revisited. *Journal of Thermal Analysis and Calorimetry, 64,* 1303-1310.

Elaloui E., Pierre A.C., & Pajonk G.M. (1997). Influence of the sol-gel processing methods on the structure and the porous texture of nondoped alumines. *Journal of Catalysis, 166(2)*, 340-346.

Ennas G., Marongiu G., Musinu A., Falqui A., Ballirano P., & Caminiti R. (1998). Characterization of Nanocrystalline γ–Fe_2O_3 Prepared by Wet Chemical Method. *Mater. Res., 14 (4)*, 1570.

Ennas, G., Musinu, A., Piccaluga, G., Zedda, D., Gatteschi, D., Sangregorio, C., Stanger, J.L., Concas, G, & Spano, G. (1998). Characterization of iron oxide nanoparticles in an Fe_2O_3-SiO_2 composite prepare by a sol-gel method. *Chem. Mater., 10,* 495-502.

Fang J., Kumbhar A., Zhou W. L., & Stokes K.L. (2003). Nanoneedle of maghemite iron oxide prepared from a wet chemical route. *Materials Research Bulletin, 38,* 461-467.

Fang J., Dai J., Kumbhar A., Zhou W.L., Wiemann J.A., & Stokes K.L. (2000). Needle-like maghemite iron oxide in nanometer size prepared from wet chemical processing. *Materials Research Society Symposium Proceedings*, *Materials Research Society 614*, F8.2.1.

Fang, J., Wang, J., Ng S.C., Gan, L.M., Quek, C.H. and Chew, C.H. (1998). Synthesis of lead zirconate powders via a polyanilline-mediated microemulsion processing route, *Materials Letters 36*, 179-185.

Fan R., Chen X.H. Gui Z. Liu L., & Chen Z.Y. (2001). A new simple hydrothermal preparation of nanocrystalline magnetite Fe_3O_4. *Materials Research Bulletin, 36,* 497-502.

Fatemi D. J., Harris V.G., Chen M.X., Malik S.K., Yelon W.B., Long G.J., & Mohan A. (1999). X-ray absorption, neotron diffraction, and Mossbauer effect studies of MnZn-ferrite processed through high energy ball milling. *J. Appl. Phys., 85 (8),* 5172-5174.

Feltin N., & Pileni M.P. (1998). New technique to make ferrite nanosized particles. *Journal de Physisique IV, 7*, 609-610.

Fidalgo A., & Ilharco L.M. (2004). Correlation between physical properties and structure of silica xerogels. *Journal of Non-Crystalline Solids* 347, 128-137.

Flinn R. A., & Trojan P.K. (1990). *Engineering Materials and Their Applications* (4^{th} ed.). United State of America: John Wiley and Sons, Inc..

Galina G., Barry J., Clayton K., Vladimir K. (2009). Synthesis of ultrasmall magnetic iron oxide nanoparticles and study of their colloid and surface chemistry. *J. Magn. Magn. Mater. 321 (10)*, 1372-1376.

Gider S., Shi J., Awschalom D.D., Hopkins P.F., Campman K.L., Gossard A.C., Kent A.D., & Von Molniar S. (1996). Imaging and magnetometry of swithching in nanometer-scale iron particles. *Appl Phys Lett., 69*, 3269-3271.

Gilbert I., Milan A., Palacio F., Falqui A., Snoeck E., & Serin V. (2003). Magnetic properties of maghemite nanoparticles in polyvinylpyridine matrix. *Polyhedron 22*, 2457-2461.

Gleiter H. (1989). Nanocrystalline material. *Prog. Mater. Sci. 33*, 223-315.

Gomez-Villacieros R., Hernan L. & Morales J. (1987). Mechanochemical preparation and thermal stability of gamma- Fe_2O_3 derived from gamma FeOOH, Material *Research Bulletin, 22*, pp. 513-520.

Gregg S.J., & Sing K.S.W. (1982a). *Adsorption, Surface Area and Porosity* (2nd ed.). United State: Academic Press Inc, p.42.

Gregg S.J. and Sing K.S.W. (1982b). *Adsorption, Surface Area and Porosity* (2nd ed.). United State: Academic Press Inc,p.126.

Grimm S., Stelzner T., Leuthauber J., Barth S., & Heide K. (1997). Particle size effects on the thermal behavior of maghemite synthesized by flame pyrolysis. *Thermochimica Acta 300* , 141-148.

Gulkova D., Solcova O., & Zdrazil M. (2004). Prepartion of MgO catalytic support in shaped mesoporous high surface area form. *Microporous and Mesoporous Materials 76*, 137-149.

Gunzler, H., & Williams, A. (2001). *Handbook of Analytical Technique* Vol. I, Weinheim: Wiley-VCH.

Guo H.**,** Zhang X.**,** Cui M.H., Sharma R., Yang N.L., & Akins A.D. (2005). Magnetic ordering of ferric oxide within SiO_2-based mesoporous materials. *Materials Research Bulletin 40(10)*,1713-1725.

Gupta A.J., & Gupta M. (2005). Synthesis and surface engineering of iron oxide nanoparticles for biomedical applications. *J. Biomaterials, 26*, 3995-4021.

Hair L.M., Coronado P.R., Reynolds J.G. (2000). Mixed-metal oxide aerogels for oxidation of volatile organic compounds. *J. Non-cryst. Solids 270*, 115-122.

Hannink R.H.J., & Hill A.J. (2006). *Nanostructure Control of Materials*, Cambridge England: Woodhead Publiching Limited.

He, Y., Yang, B., Cheng, G. and Pan, H. (2003). Synthesis of $La_2O_3/BaCO_3$ nanocatalysts and their catalytic performances, *Powder Technology 134*, 52-57.

Held G.A., Grinstein G., Doyle H., Sun S., & Murrat C.B.(2001). Competing interaction in dispersions of superparamagnetic nanoparticles. *Physics Review B 64*, 12408.

Herrero E., Cabanas M.V., Vallet-Regi M., Martinez J.L., & Gonzalez-Calbet J. M. (1997). Influence of Synthesis Conditions on the Gamma Fe_2O_3 Properties. *Solid State Ionics., 101-103,* 213-219.

Hoh J.C., Yaacob I.I., & Teh C.L. (2004). Cobalt Ferrite Magnetic Nanoparticle by Polymer Matrix Template Synthesis for High Magnetic Field Bioseparation. *Key Engineering Materials, 206,* 1201.

Ida, T., Tsuiki, H., & Ueno, A. (1987). Characterization of iron oxide in Fe_2O_3/SiO_2 catalyst. *J. Catal., 10***6**, 428-439.

Iler R.K. (1979). *The Chemistry of Silica*. New York : Wiley.

Janzen C., Knipping J., Rellinghaus B., Roth P. (2003). Formation of silica-embedded iron-oxide nanoparticles in low-pressure flames. *Journal of Nanoparticles Res 5*, 589-596.

Jing Z.H., & Wu S.H. (2004). Synthesis, characterization and magnetic properties of γ-Fe_2O_3 nanoparticles via a non- aqueous medium, *Journal of Solid State Chemistry, 177,* 1213-1218.

Kim, E.J. and Hahn, S.H. (2001). Microstructure and photoactivity of titania nanoparticles prepared in nonionic W/O microemulsion, *Materials Science Engineering A 303*, 24-29.

Kluchova K., Zboril R., Tucek J., Pecova M., Zajoncova L., Safarik I., et al. (2009). Superparamagnetic maghemite nanoparticles from solid-sate synthesis- Their functionalization towards peroral MRI contrast agent and magnetic carrier for trypsin immobilization. *Biomaterials 30*, 2855-2863.

Kodama R.H. (1999). Magnetic nanoparticles. *Journal of Magnetism and Magnetic Materials, 200***,** 359-372.

Kortesuo P., Ahola M., Kangas M., Yli-Urpo A., Kiesvaara J., & Marvola M. (2001). In vitro release of dexmedetomidine from silica xerogel monoliths: effect of sol-gel synthesis parameters. *International Journal of Pharmaceutics 221,* 107–114.

Kroll E., Winnik F.M., & Ziolo R. (1996). In situ preparation of nanocrystalline γ-Fe_2O_3 in iron(II) cross-linked alginate gels**.** *Chem. Mater., 8* , 1594.

Landau, M.V., Tavor, D., Regev, O., Kaliya, M.L. and Herskowitz, M. (1999). Colloidal nanocrystals of zeolite beta stabilized in alumina matrix, *Chemistry of Materials 11(8),* 2030-2037.

Liu T., Guo L., Tao Y., Wang Y.B., & Wang W.D. (1999). Synthesis and interfacial structure of nanoparticles Gamma-Fe_2O_3 coated with surfactant DBS and CTAB. *Nanostructured Materials, 11*, 487-492.

Liu Z.L., Wang H.B., Lu Q.H., Du G.H., Peng L., Du Y.Q., Zhang S.M., & Yao K.L. (2004). Synthesis and characterization of ultrafine well- dispersed magnetic nanoparticles. Journal of Magn. Magn. Mater. 283, 258-262.

Luckarift H.R., Spain J.C., Naik R.R., & Stone M.O. (2004). Enzyme immobilization in a biomimetic silica support. *Nature Biotechnology 22*, 211-213.

Maria F.C., Corrias A., Pashina G. (2001). Iron-oxide-silica aerogel and xerogel nanocomposite materials. *Journal of Non-Cryst Solids 293-295*, 25-31.

Martin J.I., Nogues J., Liu K., Vicent J.I., & Schuller I.K. (2003). Ordered magnetic nanostructures: fabrication and properties. *J. Magn. Magn. Mater*., *256,* 449.

Mcmichael R.D., Shull R.D., Swartzendruber L.J., Bennett L.H. & Watson R.E. (1992). Magnetocaloric effect in superparamagnets. *J. Magn. Magn. Mater., 111(1-2)*, 29-33.

Mollard P., Germi P., & Rousset A. (1977). Surface effects on saturation magnetization of fine spinel ferrite particles. *Physica B+C, 86-88 (3***)**, 1393-1394.

Monte, F.D., Morales, M.P., L**e**vy, D., Fernandez, A., Ocana, M., Roig, A., Molins, E., Ogrady, K. & Serna, C.J. (1997). Formation of γ-Fe_2O_3 isolated nanoparticles in a silica matrix. *Langmuir, 13*, 3627-3634.

Morales, M.P., Pecharroman, C., Gonzalez, T. and Sema, C.J. (1994). Structural characteristics of uniform γ-Fe_2O_3 particles with different axial (length/width) ratios. *J. Solid State Chem., 108*, 158-163.

Mornet S., Grasset E., Portier J and Duguet E. (2002). Maghemite@silica nanoparticles for biological applications. *European Cells and Materials, 3(2)*, 110-113.

Moskowitz B.M. (1991). *Hitchhiker's Guide Magnetism*. Environmental magnetism Workshop, Institute for Rock Magnetism.

Murad E. (1988). The Mossbauer spectrum of "well"-crystallized ferrihydrite. *J. Magn. Magn., 74,* 153-157.

Nalwa H.S. (2002). *Nanostructure Materials and Nanotechnology*, Concise edn. United State of America: Academic Press.

Nguyen, M.T., & Diaz, A.F. (1994). A novel method for the preparation of magnetic nanoparticles in a polypyrrole powder. *Adv. Mater., 6*, 858-860.

Nordquisi K., Pendharkar S., Durlam M., Resnick D., Tehrani S., Mancini D., Zhu T., & Shi J. (1997) Process development of 0.5μm non volatile magnetoresistive random access memory arrays. *Journal Vac. Science Technology B, 15*, 2274-2278.

Okuda Y. and Harada T. (1985). United States Patent No. 4495164.

Panina L.V. (2002). Asymmetrical giant magneto-impedance (AGMI) in amorphous wires. *Journal of Magnetism and Magnetic Material, 249*, 278-87.

Pacheco R.F., Arruebo M., Marquina C., Ibara R., Arbiol J., & Santamaria J. (2006). Highly magnetic silica-coated iron nanoparticles prepared by the arc-discharge method. *Nanotechnology, 17*, 1188-1192.

Pajonk G. M. (2003). Some applications of silica aerogels. *Colloid Polymer Science 281(7)*, 637-651.

Rainho J.P., Rocha J., Carlos L.D., & Almeida R.M. (2001). Si nuclear-magnetic-resonance and vibrational spectroscopy studies of SiO_2-TiO_2 powders prepared by the sol-gel process. *J. Mater. Res., 16*, 2369.

Rath C., Anand S., Das R.P., Sahu K.K., Kulkarni S.D., Date S.K. & Mishra N.C. (2002). Dependence on cation distribution of particle size, lattice parameter, and magnetic properties in nanosize Mn–Zn ferrite. *J. Appl. Phys., 91*, 2211–2215.

Reddy C.V.G., Seela K.K., & Manorama S.V. (2000). Preparation of Gamma Fe_2O_3 by the Hydrazine Method: Application as an Alcohol Sensor. *International Journal of Inorganic Materials, 2,* 301-307.

Sartoratto P.P.C., Caiado K.L., Pedroza R.C., Silva S.W., & Morais P.C. (2007). The thermal stability of maghemite-silica nanocomposites: An investigation using X-ray diffraction and Raman spectroscopy. *Journal of Alloys and Compounds, 434-435*, 650-654.

Santra S., Tapec R., Theodoropoulou N., Dobson J., Hebard A., & Tan W.H. (2001). Synthesis and characterization of silica-coated iron oxide nanoparticles in microemulsion: the effect of non-ionic surfactants. *Langmuir, 17*, 2900-2906.

Satterfield, C.N. (1991). *Heterogeneous Catalyst in Industrial Practice* (2^{nd} ed.). Singapore: McGraw Hill, Inc..

Schimanke G., & Martin M. (2000). In situ XRD study of the phase transition of nanocrystalline maghemite (γ-Fe_2O_3) to hematite (α-Fe_2O_3). *Solid State Ionics 136-137*, 1235-1240.

Shao, D.D., Xia A., Hu J.H., Wang C.C., & Yu W.M. (2008). Monodispersed magnetite/silica composite microspheres: preparation and application for plasmid DNA purification. *Colloids and Surfaces A*: Physiochem. and Eng. Aspects.

Solinas S., Piccaluga G., Morales M.P., & Serena C.J. (2001). Sol-Gel Formation of Gamma Fe_2O_3 in Fe_2O_3/SiO_2 Nanocomposites. *Acta Materialia, 49*, 2805-2811.

Sugimoto, M. (1999). The past, present and future of ferrites. *J. Am. Cream. Soc.. 82*, 269-280.

Sun S. (2006). Recent advances in chemical synthesis, self-assembly, and applications of FePt nanoparticles. *Adv. Mater. 18*, 393-403.

Tao K., Dou H., & Sun K. (2008). Interfacial coprecipitation to prepare magnetite nanoparticles: concentration and temperature dependence. *Colloids Surf. A: Physicochem. Eng. Aspects 320*, 115–122.

Tillotson T.M., & Reynolds J.G. (2003). Structure and characterization of sol–gel and aerogel materials and oxidation products from the reaction of $(CH_3O)_4Si$ and $C_{16}H_{33}Si(OCH_3)_3$. *Journal of Non-crystalline Solids 331 (1-3)*, 168-176.

Tronc E., Chaneac C. & Jolivet J.P. (1998). Structural and magnetic characterization of ε- Fe_2O_3. *J. Solid State Chem., 139(1),* 93-104.

Varanda L.C., Jafelicci J. P., O'Grady K., Gonzalez-Carreno T., Morales M.P., Munoz T., & Serna C.J. (2002). Structural and magnetic transformation of monodispersed iron oxide particles in a reducing atmosphese. *Journal of Applied Physics 92 (4),* 2079.

Vekas L., Doina Bica & Oana Marinica (2006). Magnetic nanofluids stabilized with various chain length surfactants. *Romanian Reports in Physics, 58(3)*, 257-267.

Venkataraman A., Hiremath V.A., Date S.K., & Kulkarni S.D. (2001). A new combustion route to γ-Fe_2O_3synthesis. *Bull. Mater. Sci., 24*, 617-621.

Vestal C.R., & Zhang Z.J. (2003). Synthesis and magnetic characterization of Mn and Co spinel ferrite-silica nanoparticles with tunable magnetic core. *Nanoletters, 3(12),* 1739-1743.

Vollath D., Szabo D.V., Taylor R.D., Willis J.O. and Sickafus K.E. (1995). Synthesis and properties of nanocrytalline superparamagnetic γ-Fe_2O_3. *Nanostruct. Mater., 6*, 941- 944.

Wang X.D., Shen Z.X., Sang T., Cheng X.B., Li M.F., Chen L.Y., & Wang Z.S. (2010). Preparation of spherical silica particles by Stober process with high concentration of tetra-ethyl-orthosilicate. *Journal of Colloid and Interface Science* 341, 23-29.

Wang Q., Yang H., Shi J., & Zou G. (2001). One step synthesis of the nanometer particles of gamma Fe2O3 by wire electrical explosion method. *Materials Research Bulletin, 36*, 503-508.

Yaacob I.I., Nunes A.C., Bose A., & Shah D.O. (1994). Synthesis and characterization of magnetic nanoparticles in spontaneously generated vesicles. *Journal of Colloid and Interface Science, 168,* 289-301.

Yang H.H., Zhang S.Q., Chen X.L., Zhuang Z.X., Xu J.G., & Wang X.R. (2004). Magnetite-containing spherical silica nanoparticles for biocatalysis and bioseparation. *Anal Chem, 76,* 1316-1321.

Yee M. (2003). *Synthesis and Characterization of Nanostructured Iron Oxide in Zeolite Matrices*. Master of Technology (Material Science) Thesis, Institute of Postgraduate Studied and Research, University of Malaya.

Ye X., Lin D., Jiao Z., & Zhang L. (1998). The thermal stability of nanocrytalline maghemite Fe_2O_3. *Journal of Physics D: Applied Physic 31*, 2739-2744.

Yoldas B.E., Annen M.J., & Bostaph J. (2000). Chemical engineering of aerogel morphology formed under nonsupercritical conditions for thermal insulation. *Chemistry of Materials 12(8)*, 2475-2484.

Zhang L., Georgia C., Papaefthymiou Ziolo R.F., Ying J.Y. (1997). Novel γ-Fe_2O_3/SiO_2 magnetic nanocomposites via sol-gel matrix mediated synthesis. *Nanostr Mat 9*, 185-188.

Ziolo, R.F., Giannelis, E.P., Weintein, B.A., Ohoro, M.P., Ganguly, B.N., Mehrotra, V., Russell, M.W., & Huffman, D.R. (1992). Matrix-mediated synthesis of nanocrystalline γ-Fe_2O_3: a new optically transparent magnetic material. *Science, 257,* 219-222.

Internet References

Internet Reference , 29/9/2010(a)

http://en.wikipedia.org/wiki/Sol-gel

Internet Reference, 13/5/11 (a)

http://www.ndt-ed.org/EducationResources/CommunityCollege/MagParticle/Physics/MagneticMatls.htm

Internet Reference, 13/5/11 (b)

http://en.wikipedia.org/wiki/Ferrimagnetism

Internet Reference, 16/5/11 (a)

http://en.wikipedia.org/wiki/Paramagnetism

Appendix 1: XRD Curve for Sample P2.5

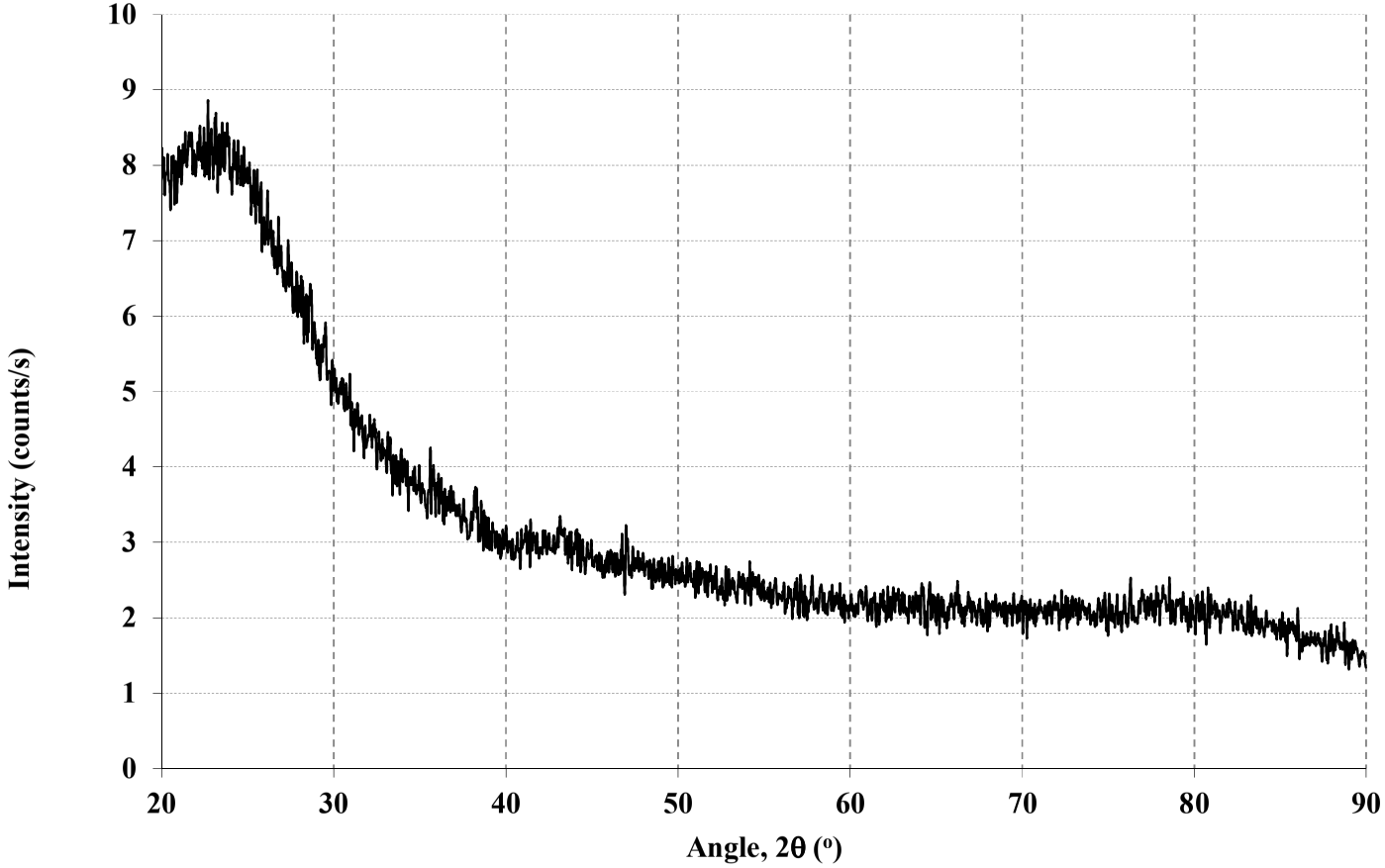

Appendix 2: XRD Curve for sample P5

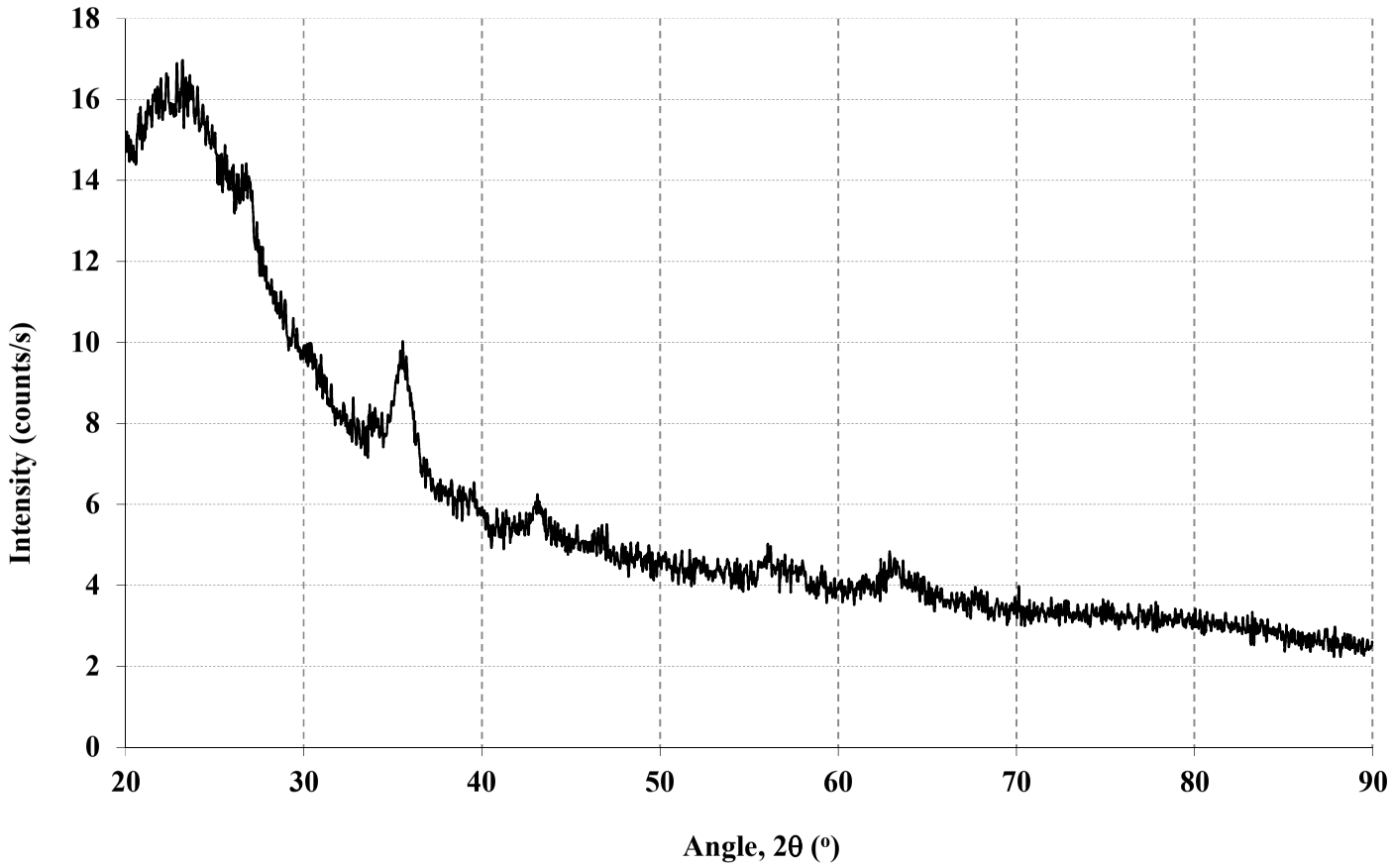

Appendix 3: XRD Curve for sample P7

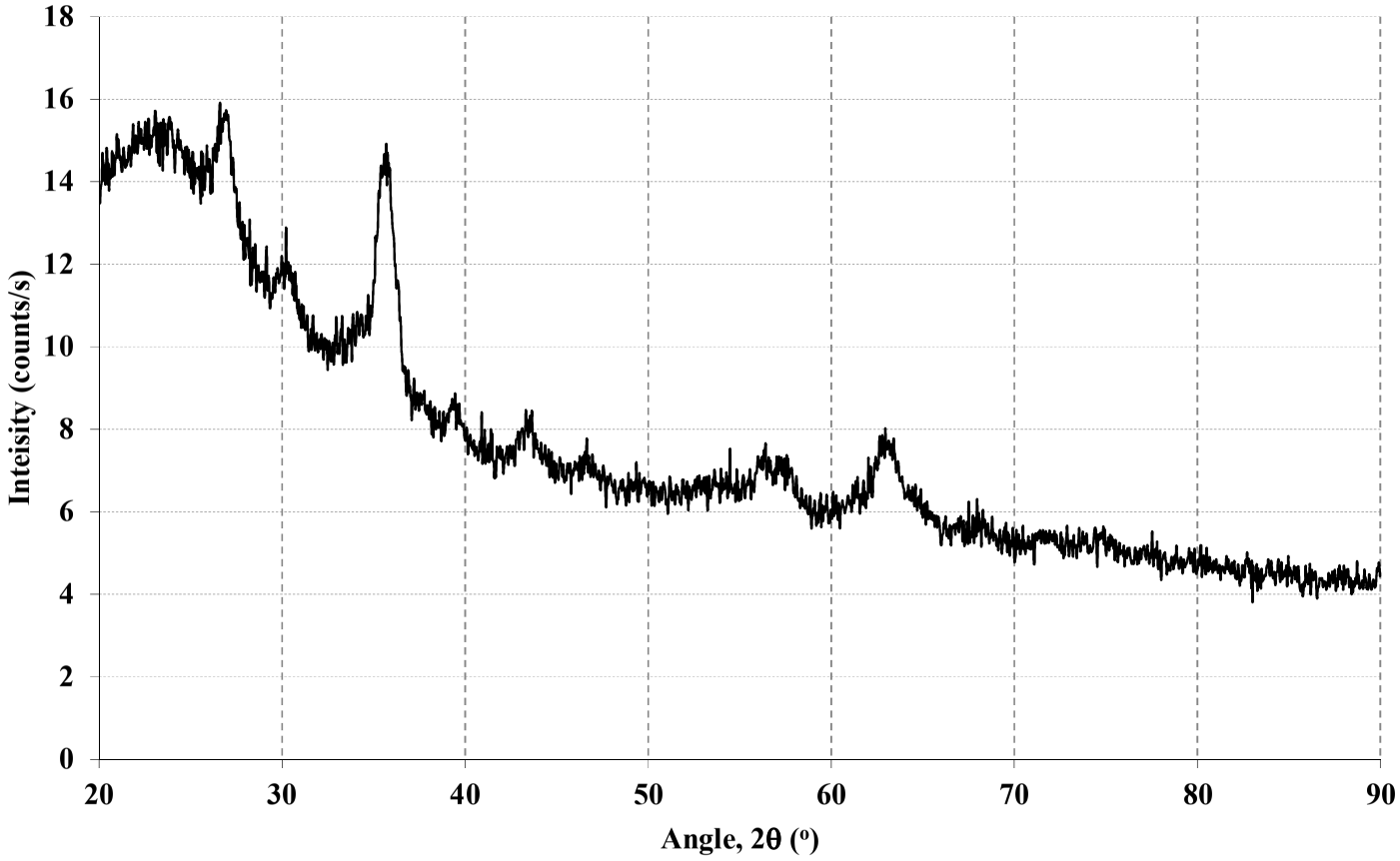

Appendix 4: XRD Curve for sample P10

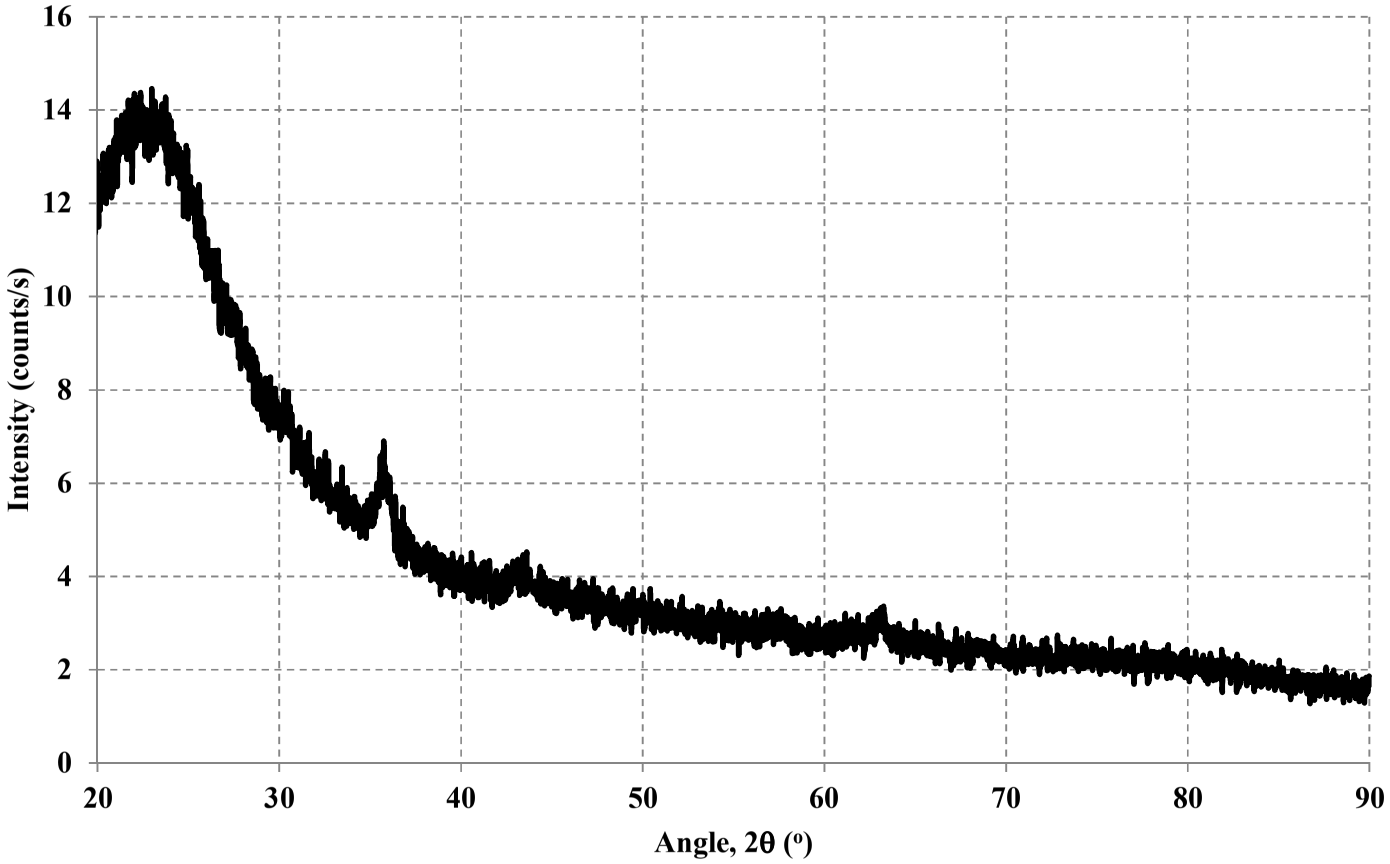

PUBLICATION LIST

1. Ang B.C., & Yaacob I. I. (2004), Preparations of magnetic nanoparticles by water in oil microemulsions. *Proceedings National Conference on Engineering and Technology*, 358-392.
2. Ang B.C., & Yaacob I. I. (2005). Synthesis and characterization of iron oxides nanoparticles. Proceedings the 6th International Conference on Fracture and Strength of Solids, Paper 209.
3. Ang B.C., & Yaacob I. I. (2005). Iron oxides nanoparticles prepared by water in oil microemulsion, Proceedings of the International Conference on Recent Advances in Mechanical & Materials Engineering, Paper 278.
4. Ang B.C., & Yaacob I.I. (2006). Synthesis and characterization of iron oxides nanoparticles. *Key Engineering Materials, 306-308,* 1115-1120.
5. Ang B.C., & Yaacob I.I. (2007). Synthesis and characterization of magnetic iron oxide nanoparticles via w/o microemulsion and Massart's procedure. *Journal of Materials Processing Technology, 191 (1-3)*, 235.
6. Ang B.C., & Yaacob I.I. (2008). Synthesis of magnetic nanoparticles by Massart's procedure. The effect of $FeCl_2$ concentration on the properties of magnetic nanoparticles, *Book of abstract of the International Conference on Functional Materials and Devices,* p.A189.
7. Ang B.C., & Yaacob I.I. (2009). Preparation of maghemite-silica nanocomposite using sol-gel technique. Proceeding of International Conference on Manufacturing Science and Engineering.
8. Ang B. C., & Yaacob I.I. (2010). Preparation of maghemite-silica nanocomposite using sol-gel technique. *Advanced Materials Research 97-101*, 2140-2143.

9. Yaacob I.I. & Ang B. C. (2010). Magnetic Nanoparticles in Water In Oil Microemulsion: Effect of Microemulsion Concentration. Book of VDM Verlag Dr. Muller.